Doctoral Thesis

On the model reduction for chemical and physical kinetics

Author(s):
Kooshkbaghi, Mahdi

ETH Library

DISS. ETH NO. 22898

On the model reduction for chemical and physical kinetics

A thesis submitted to attain the degree of

DOCTOR OF SCIENCES of ETH ZURICH

(Dr. sc. ETH Zurich)

presented by

Mahdi Kooshkbaghi

MSc in Mechanical Engineering,
Amirkabir University of Technology
(Tehran Polytechnic)

born on 25.01.1986
citizen of Iran

accepted on the recommendation of

Prof. Dr. Konstantinos Boulouchos, examiner
Dr. Christos E. Frouzakis, co-examiner
Prof. Dr. Ilya V. Karlin, co-examiner
Prof. Dr. Ioannis G. Kevrekidis, co-examiner

2015

Abstract

The need to design of efficient combustion systems with minimal emissions
of pollutants has led to the development of large detailed reaction mech-
anisms for combustion involving hundreds of chemical species reacting in
a complex network of thousands of elementary reactions. Incorporating
such a detailed reaction mechanism into multidimensional simulations is
practically impossible. Different methodologies have been proposed for the
reduction of detailed mechanisms. In the present work, model reduction
approaches based on timescale separation and thermodynamic analysis are
revisited, introduced, validated and used.

First, an algorithm based on the Relaxation Redistribution Method
(RRM) is revisited and modified for constructing the Slow Invariant Mani-
fold (SIM) of a chosen dimension to cover a large fraction of the admissible
composition space that includes the equilibrium and initial states. The
manifold boundaries are determined with the help of the Rate Controlled
Constrained Equilibrium method, which also provides the initial guess for
the SIM. The latter is iteratively refined until convergence and the con-
verged manifold is tabulated. The global realization of the RRM algorithm
is applied to hydrogen-air mixtures.

Second, Spectral Quasi-Equilibrium Manifold (SQEM), which is based
on the entropy maximization under constraints built by the slowest eigen-
vectors at equilibrium, is proposed to construct the slow manifold for com-

bustion mechanisms including the homogeneous mixtures of hydrogen/air, syngas/air and methane/air, in the adiabatic constant pressure reactor.

Third, a new approach based on the relative contribution of each elementary reaction to the total entropy production is proposed for eliminating species from detailed reaction mechanisms in order to generate skeletal schemes. The approach is applied on n-heptane/air detailed mechanism to construct two skeletal schemes for different threshold values. The accuracy of the skeletal mechanisms is evaluated in spatially homogeneous systems with respect to the ignition delay time, a single-zone engine model, and the speed and structure of spatially-varying premixed laminar flames for a wide range of thermodynamic conditions.

Fourth, the dynamics of n-heptane/air mixtures in perfectly-stirred-reactors (PSR) is investigated systematically using bifurcation and stability analysis and time integration. The significantly reduced size of the skeletal mechanism for n-heptane/air mixtures found in this thesis, enables the extension of the bifurcation analysis to multiple parameters. In addition to residence time, the effect of equivalence ratio, volumetric heat loss and the simultaneous variation of residence time and inlet temperature on the reactor state are investigated. Computational Singular Perturbation (CSP) and entropy production analysis were used to probe the complex kinetics at interesting points of the bifurcation diagrams.

The model reduction approaches can also be applied on fine-grained multiscale systems, arising in physical kinetic problems. In this thesis the systematic non-perturbative analytical approach is presented for the construction of the diffusion manifold from the one-dimensional Boltzmann equation.

Zusammenfassung

Die Forderung nach effizienten Verbrennungssystemen mit minimalen Emissionen hat zur Erstellung von detaillierten Reaktionsmechanismen mit hunderten von chemischen Stoffen zusammen mit tausenden elementarer Reaktionen geführt. Allerdings ist der Einbau von solch komplexen Mechanismen in multidimensionale Simulationen praktisch unmöglich. Daher wurden in der Vergangenheit verschiedene Methoden vorgestellt um die Reaktionsmechanismen zu reduzieren. In dieser Arbeit wird werden Methoden zur Reduktion von Mechanismen basierend auf der Separierung der Zeitskalen und einer thermodynamischen Analyse überdacht, eingeführt, validiert und verwendet.

Als erstes wurde ein Algorithmus basierend auf der "Relaxation Redistribution Method" (RRM) überdacht und modifiziert mit dem Ziel einen "Slow Invariant Manifold" (SIM) für eine gewünschte Dimension zu konstruieren, der ein breites Spektrum des erlaubten Mischungsraumes inklusive des Gleichgewichts und des Anfangszustands beinhaltet. Die Randbedingungen des "Manifolds" werden mit der "Rate Controlled Constrained Equilibrium" Methode bestimmt, die auch ein geschätztes Anfangsfeld für die SIM bereitstellt. Die letztere wird iterativ verfeinert bis die Resultate konvergieren. Anschliessend wir der "Manifold" tabuliert. Der modifizierte RRM Algorithmus wird in der Arbeit für Wasserstoff-Luft Mischungen verwendet.

Zweitens: Zur Erzeugung des "slow manifolds" für die Verbrennungsm-

echanismen von Wasserstoff/Luft, Syngas/Luft und Methan/Luft Gemischen im adiabaten Gleichdruckreaktor wird die "Spectral Quasi-Equilibrium Manifold" (SQEM) Methode vorgeschlagen, welche auf der Maximierung der Entropie unter Einschränkungen des langsamsten Eigenvektors bei Gleichgewichtbasiert.

Drittens: Ein neuer Ansatz zur Eliminierung von Spezies aus detaillierten Reaktionsmechanismen zur Erzeugung skelettaler Schemen, basierend auf dem relativen Beitrag jeder elementaren Reaktion zur gesamten Entropieproduktion, wird vorgeschlagen. Dieser wird angewandt auf detaillierte n-Heptan/Luft-Mechanismen zur Erzeugung zweier skelettaler Mechanismen für unterschiedliche Schwellwerte. Die Genauigkeit der Skelett-Mechanismen wird erstens in einem räumlich homogenen System hinsichtlich des Zündverzuges, zweitens in einem ein-Zonen Motormodell und drittens über die Geschwindigkeit und Struktur von vorgemischten Flammen validiert.

Viertens: Die Dynamik von n-Heptan/Luft Gemischen in "perfectly stirred reactors" (PSR) wird mit Hilfe von Bifurkation, Stabilitätsanalyse und zeitlicher Integration systematisch untersucht. Die gefundene drastische Reduktion der Anzahl sekelletaler Mechanismen für n-Heptan/Luft Gemische ermöglicht die Ausweitung der Bifurkation auf mehrere Parameter. Zusätzlich zur Verweildauer wurden der Einfluss des Äquivalenzverhältnises, der volumetrischen Wärmeverluste sowie die simultane Variation von Verweildauer und Einlasstemperatur auf den Reaktorzustand untersucht. Die "Computational Singular Perturbation" (CSP) Methode und Analyse der Entropieerzeugung wurden verwendet um komplexe kinetische Vorgänge an Punkten von Interesse im Bifurkations-Diagramm zu untersuchen.

Die Ansätze zur Modellreduzierung können auch auf hochauflösende Multiskalen-Systeme angewandt werden, die bei physikalisch-kinetischen Problemen auftreten. In dieser Arbeit wird ein systematischer Ansatz zur nicht-perturbativen, analytischen Erzeugung vom "diffusion manifold" auf Basis der eindimensionalen Boltzmann-Gleichung vorgestellt.

Acknowledgments

I wish to thank all the people in the Aerothermochemistry and Combustion Systems Laboratory (LAV) and in particular the head of the LAV, Professor Konstantinos Boulouchos for the chance he gave me to work in such a pleasant environment. I greatly appreciate his patience and flexibility during my PhD. I would like to thank Dr. Christos E. Frouzakis for his continual kindness during our scientific discussions and for the huge efforts he made to transform my ideas into human-readable publications. Many thanks go to Professor Ilya V. Karlin who impressed me from day one with his intelligence and his unique way of thinking and approaching problems. Thank you, Christos and Ilya, because your doors were always open to me during frustrating stages of my working life.

I want to thank Dr. Eliodoro Chiavazzo for his advice during the first six months of my PhD and Professor Ioannis G. Kevrekidis for accepting to be my co-examiner.

Special thanks go to my colleagues, Mahmoud Jafargholi, Ali Mazloomi M., Sushant S. Pandurangi, Dr. Andrea Brambilla, Dr. Martin Schmitt, and all those good friends of mine in Zürich.

I have to thank my father Muhammad, my mother Mitra and my sister Marzieh for their love, support and prayers throughout my life. I hope I was a good son and brother.

Last but not least, thank you God.

<div dir="rtl">

اللّهم عجّل لوليّك الفرج

مهدی کوشک باغی

زوریخ

یک هزار و سیصد و نود و چهار خورشیدی

</div>

Contents

List of Tables

List of Figures

Chapter 1

Introduction

1.1 Motivation

Combustion of different types of fossil fuels is crucial for covering the global energy demand for at least the next few decades. The share of a variety of hydrocarbons from simple to complex structure, in total energy use in U.S. is predicted to be about 80% in 2040 [1]. The need for efficient combustion systems with minimal emissions of pollutants has lead to the developments in the directions of new fuels and new combustion regimes. Particularly in transportation systems (internal combustion engines and gas turbines), efficient and "near-zero" pollutant combustion process can only be designed if the system can be modeled accurately. The aim of modeling is describing a physical process of interest, with a system of equations (mostly differential equations). In combustion, the system of equations should account for the fluid flow, the interaction between chemical substances and the reciprocal influence of combustion and flow.

The fluid is modeled by the Navier-Stokes equations, differential equa-

tions for the conservation of momentum, coupled with equations for the conservation of mass, energy and species. With the help of some constitutive relations, the above system of equations is closed [2]. Chemistry can be described by detailed kinetic reaction mechanisms which has the vital role in understanding the phenomena in applied and fundamental interests involved in reactive flow problems.

The detailed reaction mechanisms of practical fuels provide accurate description of combustion kinetics over wide ranges of temperature, pressure and compositions. For practical fuels (mixture of higher hydrocarbons), the detailed description typically involves hundreds of species participating in thousands of elementary chemical reactions. Starting from H_2 and CO chemistry, detailed reaction mechanisms for hydrocarbons are constructed by adding elementary reactions involving the heavier species [3]. For large hydrocarbon fuels, automated computer programs can be used to generate the detailed mechanisms based on reaction classes [4]. The size of the detailed reaction mechanisms for hydrocarbons increases dramatically with the number of carbon atoms (Table 1.1). In addition to the large number

	CH_4 [5]	C_3H_8 [6]	C_7H_{16} [4]	$C_{10}H_{22}$ [7]	$C_{12}H_{26}$ [7]	$C_{14}H_{30}$ [7]	$C_{16}H_{34}$ [7]	$C_{20}H_{42}$-2 [8]
Species	53	136	561	940	1282	1668	2116	7200
Reactions	325	966	2539	3878	5030	6449	8130	31400

Table 1.1: Sizes of detailed reaction mechanisms for hydrocarbons

of variables, chemical kinetics introduces disparate time scales which can range from nanoseconds to fractions of a second, whereas the long-term behavior of the system is dictated by timescales much slower than dissipative ones [9]. The classes of differential equations depending on greatly differ-

ing time constants are called stiff [10] and special numerical treatment is required. For more rigorous definitions and numerical schemes see [11]. In ideal spatially homogeneous reactors, such a complexity poses no difficulty and detailed chemistry can effectively use state-of-the-art stiff integrators. However, most systems of practical interest are spatially inhomogeneous. At each computational node and for every time step, the conservation laws of mass, momentum, energy and all species should be solved, resulting in a very large system of Partial Differential Equations (PDEs). Incorporating the detailed reaction mechanisms into multidimensional simulations is practically impossible due to the enormous computational cost.

The efficient simulations of reacting systems in two and three spatial dimensions necessitates the development and utilization of accurate simplified descriptions of the chemistry with a small number of representative variables. The overall integration time will decrease with the extent of reduction due to (a) fewer number of variables, (b) decreased stiffness, and (c) decreased cost of Jacobian evaluation in stiff integrators [12].

Stiff and dissipative behavior also can also be observed in infinite-dimensional dynamical systems arising in physical kinetics. The Boltzmann kinetic equation is the governing equation covering an extended range of scales and consequently model reduction techniques can be applied to obtain reduced models for the range of scales of interest. The transition from kinetic theory for perfect gases to hydrodynamic can be considered as the construction of reduced models from the detailed one.

The aim of model reduction techniques is to construct the low dimen-

sional models of large-scale dynamical systems, which can capture accurately the complex behavior of the system.

In this work, systematic approaches for constructing low dimensional chemical and physical kinetics models will be introduced and applied in different problems.

1.2 Reduction of Reaction Mechanisms

Broadly speaking, simplifying the description of chemical kinetics is achievable via different approaches (e.g. [13]):

1. Reducing the number of variables or simplifying their governing equations by eliminating inessential species, assuming zero rate of change or by lumping some of the species into integrated components;

2. Reducing the number of reactions by eliminating unimportant reactions, or by assuming that some of the reactions have equilibrated;

3. Decomposing the kinetics into fast and slow subsystems (in the presence of timescale separation) and finding an accurate description of the evolution for the slow subsystem.

The first and second approaches typically achieving reduction in the number of species lead to the so-called *skeletal model reduction*. Methods falling within the scope of the third category provide systematic tools based on timescale analysis.

Comprehensive mechanisms usually contain a number of species and reactions which, have only minor effects on the macroscopic behavior of the system (e.g. temporal evolution of the temperature and heat release). Skeletal mechanisms have fewer number of species/reactions which makes them less complex compared to the comprehensive mechanisms [14]. On the other hand, usually unimportant reactions and species correspond to fast timescales, therefore, eliminating them makes the system less stiff. Many methods have tried to answer how to select redundant species and reactions and some of them will be referred to, latter in this chapter.

A common feature of systems enjoying timescale separation is that the relaxation has a certain geometrical structure in phase space: individual trajectories tend to relax towards chemical equilibrium or other low-dimensional attractors through a nested hierarchy of smooth hypersurfaces (inertial manifolds) (e.g. [13, 15, 16]). Sample trajectories for the oxidation of H_2 in air in an isenthalpic isobaric reactor are shown in Fig. 1.1. The detailed reaction mechanism of hydrogen involves 9 species in 21 elementary reactions [17]. Conservation of atoms for O, H, N elements imposes three constraints on the number of moles of species. Therefore, the dynamical system is effectively six-dimensional. It can be seen that, all trajectories are attracted to the neighborhood of the thick line (slow manifold) embedded in the phase space whose approximate loci is marked by the oval. For the selected trajectory (solid line), the discrete times are also marked, showing that more than 60% of the temporal evolution is restricted to dynamics on a one-dimensional manifold.
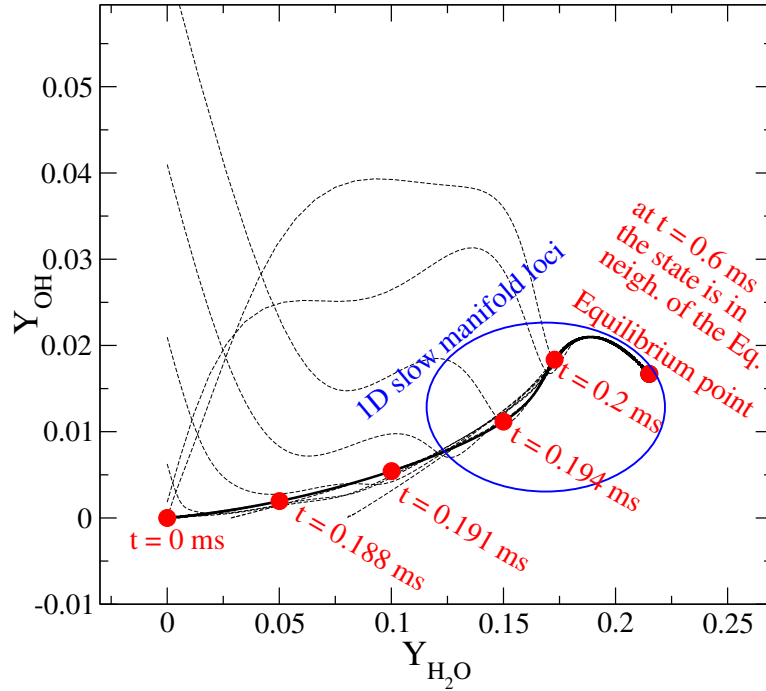
Figure 1.1: Sample trajectories (dashed lines) of the chemical reactions for H_2/air autoignition (constant pressure ($p = 1$ atm) and enthalpy $H_0 = 1024.1$ kJ/kg) projected on Y_{H_2O}-Y_{OH} plane. The circles denote the discrete time for selected trajectory (solid line) and the oval shows the approximate location of one-dimensional slow manifold of the system.

Neglecting the initial transient, the dimension of attracting manifolds are much lower than the dimension of the full state. As shown in hydrogen oxidation example, the dynamics in the neighborhood of the equilibrium evolves through a one-dimensional manifold to ends up on the zero-dimensional manifold of the equilibrium. With sufficiently separated relaxation times, the initial transient is typically short and the system state spends most of its temporal evolution on low-dimensional manifolds, known as slow manifolds.

The slow manifolds can help to formulate reduced models for the detailed evolution and modern automated approaches for model reduction are based on their computation. At present there are a number of approaches for chemical kinetics reduction. A partial list is given below. A detailed discussion and presentation of the approaches can be found in the review papers [9, 13, 18] and the recent book of Turànyi and Tomlin [15].

1.2.1 Systematic approaches for species and reactions removal

The species and reactions can be ranked according to their importance in the observed behavior. The challenge then becomes how to find the eventually redundant species and reactions systematically. Typically, removal of redundant reactions will indirectly shorten the list of species by eliminating the species which only appear in the redundant reactions. The identification of the redundant elementary reactions is in general simpler than unimportant species and sometimes chemical intuition maybe be enough to distinguish the unimportant reactions based on their class.

In one of the early attempts to generate skeletal mechanisms, the reduced model was considered as accurate when the temporal evolution of the thermal and chain reactions could be accurately captured [19]. It has been observed that in detailed mechanisms the change in the rate of some elementary reactions results in a significant change in the relaxation of the system state. These reactions, known as *rate-limiting steps* can be identified systematically by absolute and relative sensitivities. The results of

this analysis is usually expressed in terms of the sensitivity matrix including normalized sensitivity coefficients [20, 21]. However, one cannot safely eliminate the elementary reactions corresponding to small sensitivity coefficients. Principal Component Analysis (PCA) [22] has been proposed as an informative tool to scrutinize the sensitivity analysis results. Applications of PCA in skeletal mechanism generation for H_2/air and CH_4/air in premixed laminar flame and perfectly-stirred and plug-flow reactors can be found in [23, 24].

Another group of methods aimed at species and reactions removal is based on graphs. After selecting the set of important species, the network of species can be constructed around them. The skeletal mechanism can be generated by eliminating the species whose distance from the major species is greater than a user-defined threshold or by removing the elementary reactions participating in minor pathways. There are several proposals in the literature for defining the connection weight in the graph. In the *Connectivity Method* (CM), the graph edges are constructed based on the percentage change of the production rate of important species due to 1% change in the concentration of minor species [15, 20]. The method is based on the investigation of the elements of the normalized Jacobian of the chemical kinetics system. In the *Reaction Path Analysis* (RPA), the path connecting the reactants to major products are constructed based on the contribution of each reaction to the net rate of production/depletion of each species. The minor path and consequently the redundant elementary reactions (and indirectly unimportant species) can then be removed from the detailed mechanism

(see for example the oxidation path of C_1 and C_2 hydrocarbons [25] and skeletal mechanism for methane at lean condition [24]). The atomic flux analysis considers the elemental flux of atom A from species i to species j through reaction k. Normalized fluxes define the connectivity topology and the relatedness strengths between nodes of the graphs [24, 26]. Similar to CM, the *Directed Relation Graph* (DRG) method was proposed to quantify the directed influence of one species on production rate of another [27] and the algorithm is computationally more effective than computing and analyzing the Jacobian for large mechanisms. Path Flux Analysis (PFA) is another approach similar to RPA and DRG in which the production and consumption fluxes of the species are used to define the connection weights in the graph [28].

In *Trial and Error* approaches [15, 29], important/redundant species can be determined by generating series of skeletal mechanisms where in each one a species is removed and the results are compared with the detailed mechanism. The *necessity analysis method* is introduced to combine the sensitivity and reaction path analysis with trial and error method to generate as small as possible skeletal mechanism with a wide range of applicability [30]. A necessity value is assigned to each species which is the maximum of the total amount of formation and consumption includes both reaction flow values and sensitivity coefficients [30].

Another category of approaches is based on *optimization* which aims at minimizing a target function using the smallest number of species from the detailed description. The target function is a user-defined functional

measuring the error in the feature (e.g. ignition delay) of the original system which is of interest [12, 31] or the minimization of the number of reactions, while the error with respect to the detailed model is constrained [32].

The important species and reactions can also be identified based on their supporting or opposing contribution in the development of the mode of the system corresponding to the time-scale of interest. In the scope of time-scale based methods, the *Computational Singular Perturbation* (CSP) proposes a systematic approach for understanding the chemical processes and their relation to the observed behavior. In the scope of skeletal mechanism construction, CSP introduced several diagnosis tools like the CSP *radical pointer*, pointing to the species which are mostly affected by the corresponding time scale, and the *amplitude participation index*, measuring the contribution of elementary reaction k to the i-th CSP mode (see chapter 5). In the last two decades several modifications have been proposed including a modified algorithm for constructing the skeletal mechanism for hydrocarbons [33] and additional diagnostic tools like *timescale participation index* [34].

1.2.2 Slow-Fast motion decomposition

Slow-fast systems are dynamical systems, enjoying disparate timescales. An arbitrary slow-fast initial value problem can be written in the form

$$\varepsilon \frac{d\boldsymbol{x}}{d\tau_s} = \boldsymbol{f}(\boldsymbol{x}, \boldsymbol{y})$$
$$\frac{d\boldsymbol{y}}{d\tau_s} = \boldsymbol{g}(\boldsymbol{x}, \boldsymbol{y})$$

where $\boldsymbol{f} : \mathbb{R}^n \times \mathbb{R}^m \to \mathbb{R}^n$, $\boldsymbol{g} : \mathbb{R}^n \times \mathbb{R}^m \to \mathbb{R}^m$. The components of $\boldsymbol{x} \in \mathbb{R}^n$ are fast while $\boldsymbol{y} \in \mathbb{R}^m$ are slow variables and the timescale separation parameter is $0 < \varepsilon \ll 1$. The slow timescale is τ_s and the fast time scale can be set by $\tau_f = \tau_s/\varepsilon$, and the associated form of the original system with respect to the fast time τ_f can be written as:

$$\frac{d\boldsymbol{x}}{d\tau_f} = \boldsymbol{f}(\boldsymbol{x}, \boldsymbol{y})$$
$$\frac{d\boldsymbol{y}}{d\tau_f} = \varepsilon \boldsymbol{g}(\boldsymbol{x}, \boldsymbol{y})$$

In the adiabatic limit $\varepsilon \to 0$ the system of differential equations becomes a system of Differential Algebraic Equations (DAEs)

$$0 = \boldsymbol{f}(\boldsymbol{x}, \boldsymbol{y})$$
$$\frac{d\boldsymbol{y}}{d\tau_s} = \boldsymbol{g}(\boldsymbol{x}, \boldsymbol{y})$$

The set $\mathcal{M} := \{(\boldsymbol{x}, \boldsymbol{y}) | \boldsymbol{x} = \boldsymbol{x}^*(\boldsymbol{y}) \wedge f(\boldsymbol{x}^*(\boldsymbol{y}), \boldsymbol{y}) = 0\}$ is the slow manifold which the system trajectories reach after a short initial transient [35, 36]. The slow manifolds which are invariant under the action of the dynamical system are known as Slow Invariant Manifolds (SIM) (see chapter 2).

The traditional approaches for simplifying reaction mechanisms are based on the *Quasi Steady State Approximation* (QSSA) and the *Partial Equilibrium Assumption* (PEA) [9, 37]. In QSSA, the production and destruction rates of the Quasi Steady State (QSS) species are much larger than the net rate of formation [9]. The rate of formation for the QSS species can be set to be zero, turning the system of differential equations to a system

of DAEs. The solution of the algebraic equations defines the QSS manifold, which is parametrized by the non-QSS species. The concentrations of the QSS species can be computed from the non-QSS species concentrations.

On the other hand, under certain conditions, a reaction or a group of reactions can have very large forward and backward rates so that they rapidly relax towards the quasi-equilibrium state. In the PEA approach, the net rate of these reactions can be approximately set to zero, and similar to QSSA a system of DAEs can be constructed for the net rate of the concentration of the species participating in the equilibrated reactions.

In order to employ QSSA and PEA for reduction, chemical insight is needed to identify the QSS species or the equilibrated reactions. In addition, the system of DEAs deduced from these methods was constructed analytically and the results were case dependent. Different approaches have been proposed to identify the slow and fast variables and construct the slow manifold in a systematic way. For the purposes of this work, low-dimensional manifold construction techniques for chemical kinetics can be broadly classified into two categories [38], timescale-based and geometrical approaches.

The first category is based on timescale analysis to identify the slow and fast modes of the system. Generally, *singular perturbation* provides a rigorous framework for analyzing systems with slow-fast characteristics. In this context, CSP proposed an iterative refinement procedure aiming at approximating the basis vectors spanning the slow and fast subspaces [39]. Starting with an arbitrary initial basis, the refinement procedure can be written in terms of evolution equations of slow and fast basis vectors

which approximate the slow manifold and the accuracy of reduced dynamics improves by one order after each iteration [40]. After a number of iterations the vectors spanning the slow and fast subspaces are stored columnwise in matrices $\boldsymbol{A}_s$ and $\boldsymbol{A}_f$ and the corresponding $\boldsymbol{B}^s$ and $\boldsymbol{B}^f$ include the orthogonal row vectors. The approximation of the slow manifold is the solution of $\boldsymbol{B}^f[\boldsymbol{f}, \boldsymbol{g}]^T = 0$ ($[:,:]$ denotes vertical concatenation) while the reduced dynamics is governed by $d[\boldsymbol{x}, \boldsymbol{y}]^T/d\tau_s = \boldsymbol{A}_s(\boldsymbol{B}^s[\boldsymbol{f}, \boldsymbol{g}]^T)$ [41].

Based on the spectral decomposition of the Jacobian, which recovers the CSP basis to leading order, the *Intrinsic Low Dimensional Manifold* (ILDM) method [42] constructs a first-order approximation of the slow manifold [43]. ILDM assumes that the slow and fast subspaces can be locally spanned by the left and right eigenvectors at every point in phase space.

The second category of low-dimensional manifold construction methods includes geometrical approaches. For example, the thermodynamic properties which are known functions of the system state can be used to determine low-dimensional thermodynamic manifolds, which are 'good' in the sense that they are not folded, multi-valued, discontinuous, non-realizable or non-smooth [18]. The Rate-Controlled Constrained Equilibrium (RCCE) method assumes that the variables evolve from the initial to the equilibrium (steady) state through a sequence of quasi-equilibrium states, which can be computed by minimizing a thermodynamic Lyapunov function under appropriate predefined constraints [44, 45]. The temporal evolution of the system can be expressed as a function of the rate of change of the constraints. Similarly, an invariant constrained equilibrium edge (ICE) manifold is con-

structed from trajectories emanating from the constrained equilibrium edge, which can be defined by an RCCE-like approach; the local species reconstruction can be obtained with the help of preimage curves [46]. Trajectories, which are closest to equilibrium, are alternative candidates for the slow manifold. The slow manifold is the trajectory which is discriminated from the others via minimal entropy production analysis [47]. It is worth noting that manifolds obtained using thermodynamic functions are approximations of the SIM, which often are neither slow nor invariant [38].

Another constructive geometrical method proposed by Roussel and Fraser [16] is based on the iterative solution of the *Partial Differential Equations* (PDEs) defining the slow manifold. The n_d-dimensional inertial manifold is assumed to have the form $\mathcal{M} = \mathcal{M}(\xi_1, ..., \xi_{n_d})$ where ξ_i are representing the slow manifold parametrization variables and n_d is the dimension of manifold. By substituting this form in to the system of ODEs, one can find the *functional* equation in the form of PDEs which govern the convergent sequence of surface functions $\mathcal{M}_i$, where i is the number of iterations.

Gear et al. [48] presented a procedure to find the slow manifold by iterative integration. Starting from an arbitrary initial point, time integration brings the system toward the state where fast components are relaxed. This state is then extrapolated back to the same value of slow variables by polynomial extrapolation. The extrapolated state provides the approximation of initial point where the fast components of dynamics are quietened. After several iterations, the initial point is projected on the slow manifold

and by time integration from this new initial point one can construct the slow manifold or solve the full system which is now less stiff. The reduced dynamics is achieved without having it in the closed form, which is the basic of equation-free algorithms [49].

1.3 Hydrodynamic limits of the Boltzmann Equation

At the International Congress of Mathematicians (ICM) held in Paris in 1900, Hilbert posed 22 problems [50]. Hilbert's 6th problem ("Mathematical treatment of the axioms of physics") can be recast as the question whether macroscopic concepts such as the viscosity or the nonlinearity can be understood microscopically [51] or how to derive continuum compressible gas dynamics at low Knudsen number from the Boltzmann equation for rarefied gases [52]. The problem is revisited in the *hydrodynamic limit of the Boltzmann equation* in which *the derivation of hydrodynamics from the Boltzmann equation and related dissipative systems is formulated as the problem of a slow invariant manifold in the space of distributions [53].* Several approaches including the well-known Chapman-Enskog expansion [54], Grad's moment method [55] and direct solution of the invariance equation [53] have been proposed for the construction of the hydrodynamic manifolds which cover a wide range of Knudsen numbers. The problem is well studied up to the conditions where the solutions are smooth i.e. before shock formation [52]. The Chapman-Enskog expansion is divergent and by decreasing

the truncation error one can get a better approximation of hydrodynamic manifold for small Knudsen numbers. However, at the same time consequent continuum equations (such as Burnett approximation) are divergent and violate the basic physics behind the Boltzmann equation [56].

Ongoing studies in pure mathematics are carried out to answer (a) whether it is possible in a mathematically rigorous way to obtain the macroscopic equations from the microscopic point of view, (b) and how to construct such a manifold. The model reduction approaches aim at proposing answers to the second question.

1.4   Outline of the thesis

The rest of the thesis is organized as follows (Fig. 1.2)
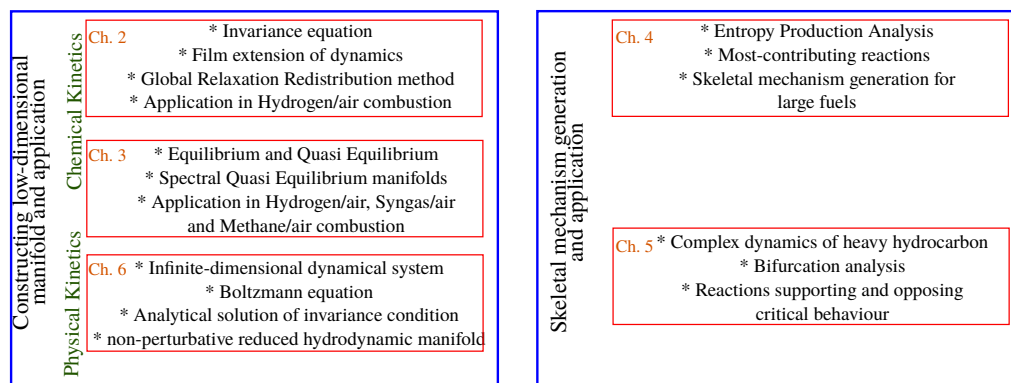
Figure 1.2: Thesis in a nutshell

- Chapter 2 presents the basic notion of chemical kinetics equations governing the dynamics of homogeneous reactive flows and the Slow Invariant Manifold (SIM) concept is briefly discussed. The first sys-

tematic approach proposed in this thesis for the construction of a SIM, the *global Relaxation Redistribution Method* (gRRM) is then presented. It is an extension of the RRM procedure, which can be regarded as an efficient and stable scheme for solving the *film equation of dynamics* (see 2.2) where a discrete set of points is gradually relaxed towards the SIM. The algorithm is applied for the construction of a one-dimensional SIM of a simple singularly-perturbed nonlinear system model and the results are compared with those of the ILDM slow manifold. gRRM is then applied to the detailed combustion mechanism for hydrogen/air and two- and three-dimensional SIMs are constructed. Finally, the SIM is used as a reduced model for auto-ignition and laminar premixed flame of hydrogen-air mixtures.

- Chapter 3 is devoted to a geometrical approach in the scope of thermodynamics manifold category, called the Spectral Quasi-Equilibrium Manifold (SQEM) method, for the construction of SIMs. SQEM is a class of model reduction techniques for chemical kinetics based on the entropy maximization under constraints built by the slowest eigenvectors at equilibrium. The method is first discussed and validated through the Michaelis-Menten kinetic scheme, and the quality of the reduction is discussed and related to the temporal evolution and the gap between eigenvalues and Lyapunov exponents. SQEM is then applied to detailed reaction mechanisms for homogeneous mixtures of hydrogen/air, syngas/air and methane/air, in an adiabatic constant pressure reactor. The states of the system determined by SQEM are

compared with those obtained by direct integration of the detailed mechanism, and good agreement between the reduced and the detailed descriptions is demonstrated. The SQEM reduced model of hydrogen/air combustion is also compared with another similar technique, Rate-Controlled Constrained Equilibrium (RCCE). For the same number of representative variables, SQEM is found to provide a more accurate description.

- In Chapter 4 we proposed a systematic approach for skeletal mechanism generation based on the relative contribution of the elementary reactions to the total entropy production. The notion of the entropy production for chemical kinetics is briefly reviewed, and the approach is applied to a database of solutions for homogeneous constant pressure auto-ignition of n-heptane to construct two skeletal schemes for different threshold values defining the important reactions contributing to the total entropy production. The accuracy of the skeletal mechanisms is evaluated in spatially homogeneous systems for ignition delay time and a single-zone engine model in a wide range of thermodynamic conditions. High accuracy is also demonstrated for the laminar speed and the flame structure of spatially-varying premixed flames.

- Chapter 5: The ability of the entropy production method to significantly reduce the size and complexity of detailed mechanism enables us to investigate the complex dynamics of large hydrocarbons where the implementation of the comprehensive mechanism would require ex-

cessive computational cost. The dynamics of n-heptane/air mixtures in perfectly-stirred-reactors (PSR) is investigated systematically using bifurcation and stability analysis and time integration. In addition to residence time, which is the well-studied "S-shape" curve in combustion community, the effect of equivalence ratio, volumetric heat loss and the simultaneous variation of residence time and inlet temperature on the reactor state are investigated. Multiple ignition and extinction turning points leading to steady state multiplicity and oscillatory behavior of both the strongly burning and the cool flames are found, which can lead to oscillatory (dynamic) extinction. Two-parameter continuations revealed isolas and co-dimension two bifurcations (cusp, Bagdanov-Takens, and double Hopf). Particularly, the extension of the bifurcation analysis to multiple parameters is owing to less complex skeletal mechanism found in Chapter 4. The CSP method is briefly presented and used along with entropy production analysis to probe the complex kinetics at interesting points of the bifurcation diagrams.

- Chapter 6: The non-equilibrium states of a thermodynamic system can be described by the Boltzmann equation. The derivation of hydrodynamics from the kinetic description can be considered as construction of a reduced model from the Boltzmann equation. As stated in the recent review [53] : "*The reduction from Boltzmann kinetics to hydrodynamics may be split into three problems: existence of hydrodynamics, the form of the hydrodynamic equations, and the relaxation of*

the Boltzmann kinetics to hydrodynamics." In chapter 6 we present a new approach for constructing the hydrodynamic manifold for infinite-dimensional system. In the Chapman-Enskog approach conventionally the distribution function is expanded in terms of a small parameter (Knudsen number) to derive the Navier-Stokes equation and its transport coefficients. The first-order expansion is valid for the slip-flow regime ($\text{Kn} \lesssim 0.1$). By construction, the Chapman-Enskog expansion and consequently the Navier-Stokes equations fail for appreciable Knudsen numbers. In Chapter 6 we address the second problem raised from the Boltzmann kinetic reduction field by constructing the semi-analytic hydrodynamic manifold for the one-dimensional diffusion equation by non-perturbative extension. This approach has the potential to extend the construction of hydrodynamic manifold from the kinetic equation (Navier-Stokes type equations which are valid for extended range of Knudsen number) to multi-dimensional flows.

Chapter 2

The global Relaxation Redistribution Method [1]

2.1 Introduction

In this chapter we will discuss the first geometric approach we have proposed for the construction of slow invariant manifolds.

Formally, the slow dynamics can be described by the film equation (see Sec. 2.2), which in the general case can be solved iteratively starting from an initial guess that is gradually relaxed to the slow manifold. The *Method of Invariant Grid* (MIG) defines the slow manifold as a collection of discrete points in concentration space, which lie on the steady solution of the film equation [57].

In the spirit of the MIG, the Relaxation Redistribution Method (RRM)

---

was proposed as a way to construct slow manifolds of any dimension by refining an initial guess (initial grid) until it converges to a neighborhood of the SIM [58]. In its local realization, the stability of the RRM refinements provides a criterion for finding the dimension of the local reduced model [58]. This dimension may become large when extending the manifold to cover the whole composition space (up to the full system dimension in the hydrogen combustion example considered in [58]). As such, the local formulation of RRM requires smart storage/retrieval tabulation methods for computational efficiency.

In this chapter, we propose an RRM-based method for the construction and tabulation of manifolds of fixed pre-selected dimension. For this purpose, an initial guess for the manifold is constructed based on the thermodynamic manifold found by Rate-Controlled Constrained Equilibrium (RCCE), and the manifold boundary is kept fixed while the RRM algorithm is applied to the interior points. For the region within the RCCE-defined boundary where the slow dynamics can be described by a SIM with the chosen dimension, the algorithm converges to the slow invariant manifold. An indicator for the quality of the reduction is proposed based on a measure of the manifold invariance. For the region where a higher-dimensional reduced description is required, the algorithm still converges to a manifold which approximates the invariant manifold better than the RCCE manifold of the same dimension. The algorithm is applied to hydrogen-air mixtures and the tabulated reduced description is validated in homogeneous systems as well as in a laminar premixed flame in Sec. 2.5.

2.2 Slow invariant manifold: Concept and Construction

Consider an autonomous system satisfying the Cauchy-Lipschitz existence and uniqueness theorem with a single stable fixed point (unique equilibrium) whose detailed (*microscopic*) dynamics are described by the evolution of its state vector $\mathbf{N}(t)$ in a n_s-dimensional phase space S, $\mathbf{N}(t) \in S \subset \mathbb{R}^{n_s}$,

$$\frac{d\mathbf{N}}{dt} = \boldsymbol{f}(\mathbf{N}) \qquad (2.1)$$

where $\boldsymbol{f}$ is a vector valued function, $\boldsymbol{f} : S \to \mathbb{R}^{n_s}$.

A domain $U \subset S$ is a *positively invariant manifold* if every trajectory of system (2.1) starting on U at time t_0 remains on U for any $t > t_0$. Therefore, $\mathbf{N}(t_0) \in U$ implies $\mathbf{N}(t) \in U$ for all later times $t > t_0$.

The dynamics of (2.1) is typically characterized by different time scales. For significant time scale disparity, after an initial transient, trajectories are quickly attracted to a lower-dimensional manifold where they continue to evolve at a slower time scale towards the steady state $\mathbf{N}^{eq} \in S$. This positively-invariant manifold is the SIM [59], and its construction can be based on the definition of fast and slow sub-spaces within the phase space [60–62].

Neglecting the initial fast transient, the long-time dynamics can be described by a (possibly significantly) smaller number of the slowly-evolving *macroscopic* variables $\boldsymbol{\xi}$, which can be used to parametrize the SIM. The

$n_d < n_s$ macroscopic variables $\boldsymbol{\xi}$ belong to an n_d-dimensional space Ξ, and can be used for the description of the reduced dynamics of (2.1). The manifold parametrization space Ξ can be spanned by different combinations of the state variables, $\mathbf{N} \in S$. A microscopic state $\mathbf{N}$ located on the low-dimensional manifold is shown schematically in Fig. 2.1(a). More formally,
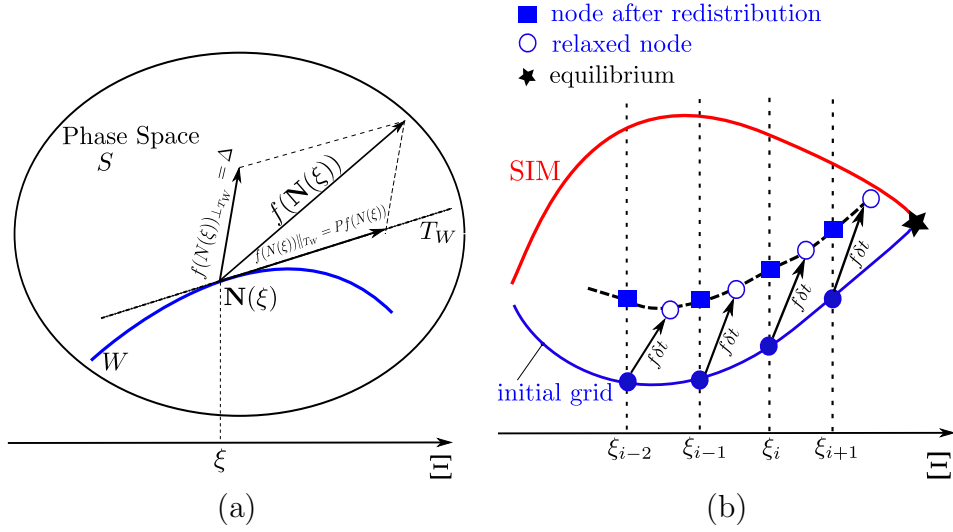
Figure 2.1: (a) Schematic of the motion decomposition which is exploited in the construction of the slow manifold; (b) Relaxation Redistribution algorithm: the effect of slow motions are neutralized via redistribution.

any point x on $\mathbf{W}$ satisfies $x = \mathscr{F}(\boldsymbol{\xi})$ where $\mathscr{F} : \Xi \to S$ maps points $\boldsymbol{\xi} \in \Xi$ in the manifold parametrization space onto the corresponding point on the manifold $\mathbf{W}$ which is embedded in the phase space S (see [59]).

The evolution of a state $\mathbf{N}$ can be decomposed into the slow component along $T_{\mathbf{W}}$, the tangent space of $\mathbf{W}$, and its complement in the transverse direction (Fig. 2.1(a)),

$$\boldsymbol{f}(\mathbf{N}(\boldsymbol{\xi})) = \boldsymbol{f}(\mathbf{N}(\boldsymbol{\xi}))_{\| T_{\mathbf{W}}} + \boldsymbol{f}(\mathbf{N}(\boldsymbol{\xi}))_{\perp T_{\mathbf{W}}} \qquad (2.2)$$

The slow and fast components are defined, respectively, as

$$\boldsymbol{f}(\mathbf{N}(\boldsymbol{\xi}))_{\parallel T_{\mathbf{W}}} = \mathbf{P}\boldsymbol{f}(\mathbf{N}(\boldsymbol{\xi})) \tag{2.3}$$

$$\boldsymbol{f}(\mathbf{N}(\boldsymbol{\xi}))_{\perp T_{\mathbf{W}}} = \boldsymbol{\Delta}(\mathbf{N}(\boldsymbol{\xi})) = \boldsymbol{f}(\mathbf{N}(\boldsymbol{\xi})) - \mathbf{P}\boldsymbol{f}(\mathbf{N}(\boldsymbol{\xi})) \tag{2.4}$$

in terms of an $n_s \times n_s$ projection matrix $\mathbf{P}$ and the defect of invariance $\boldsymbol{\Delta}(\mathbf{N}(\boldsymbol{\xi}))$.

By definition, $\mathbf{W}$ is a positively-invariant manifold if any state that is initially on $\mathbf{W}$ remains on it during the subsequent time evolution. Hence, relaxation will only proceed along the tangent space and the normal component should be zero,

$$\boldsymbol{\Delta}(\mathbf{N}(\boldsymbol{\xi})) = 0, \qquad \boldsymbol{\xi} \in \Xi \tag{2.5}$$

Equation (2.5) is known as the invariance condition, and can be solved for the unknown slow invariant manifold. In the method of invariant manifold (MIM), the SIM is the stable solution of the so-called film extension of dynamics [59],

$$\frac{d\mathbf{N}(\boldsymbol{\xi})}{dt} = \boldsymbol{\Delta}(\mathbf{N}(\boldsymbol{\xi})) \tag{2.6}$$

which defines an evolutionary process guiding an initial guess for the manifold towards the slow invariant manifold. In numerical realizations, manifolds are usually represented by a grid (discrete set of points), as proposed in the method of invariant grid (MIG) [57]. Due to the locality of MIM construction, we make no further distinction between manifold and grid.

If the initial grid is subjected to the system dynamics, the distance between the grid nodes shrinks and the whole grid contracts to a neighborhood around the equilibrium state. The key idea of RRM is to alternate a relaxation step with an appropriate movement that counterbalances shrinking. One iteration step of RRM is shown schematically in Fig. 2.1(b). After relaxation, the nodes of the initial grid (filled circles) evolve to different positions (open circles) and the macroscopic coordinates change. The increased density of the grid points close to equilibrium can result in a reduction of the grid spacing. To prevent this, the redistribution step brings the macroscopic coordinates $\boldsymbol{\xi}$ back to their previous values by interpolation between the inner relaxed states and extrapolation for grid points outside the contracted boundaries. The converged solution is the manifold containing all the states for which further relaxations result in movement only along the manifold.

In order to clarify the aforementioned notions, the singularly-perturbed dynamical system proposed in [63] is considered with $\mathbf{N} = (x, y)^T$

$$\frac{dx}{dt} = 2 - x - y \tag{2.7a}$$

$$\frac{dy}{dt} = \gamma(\sqrt{x} - y) \tag{2.7b}$$

For $x(t), y(t) \in \mathbb{R}$, $x(t) \geq 0$ and $\gamma \gg 1$, the system evolves from any initial condition (x_0, y_0) towards the fixed point at $(1, 1)$.

For $\gamma = 20$, choosing $\xi = x$ to parametrize the manifold and $y = 1 - x$ as the initial grid, after a single integration step (relaxation) with $\delta t = 0.07$,

the initial grid (open squares) contracts significantly (Fig. 2.2(a), open circles). Redistribution is then applied to find the y values at the original locations of the parameterizing macroscopic coordinates by linear interpolation between relaxed states on the interior grid and linear extrapolation at the boundary (two leftmost star symbols). The RRM converges to the slow
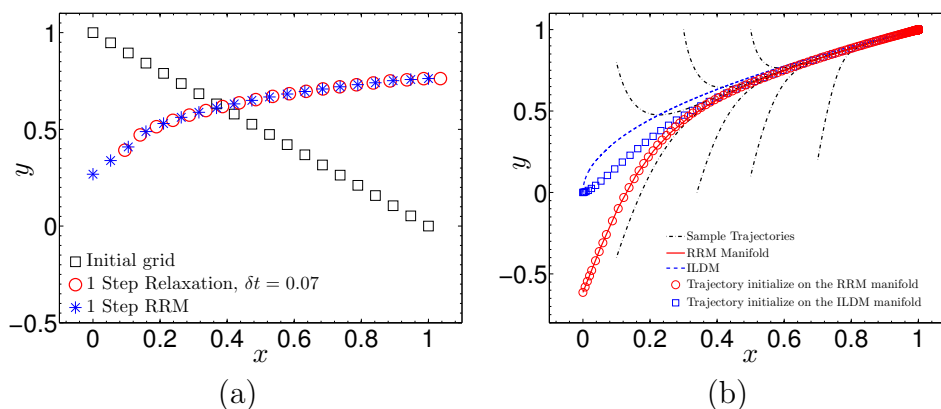
Figure 2.2: (a) The effect of applying a single RRM step on the nodes of the initial grid; (b) comparison between ILDM manifold, RRM manifold and sample trajectories $\gamma = 20$.

invariant manifold after 10 iterations for a tolerance of 10^{-4} (Fig. 2.2(b), solid line).

The defect of invariance $\mathbf{\Delta}$ can be used as an indicator for the time after which the reduced description becomes accurate. For the chosen parametrization, the kernel of the projector $\boldsymbol{P}$ is $(1,0)$. $\boldsymbol{P}$ is spanned by its image, which is the tangent subspace to the manifold, $T_W = im\mathbf{P}$, and the orthogonal to the kernel. Hence,

$$\mathbf{P} = \begin{pmatrix} 1 \\ \frac{dy}{dx} \end{pmatrix} (1,0) = \begin{pmatrix} 1 & 0 \\ \frac{dy}{dx} & 0 \end{pmatrix} \tag{2.8}$$

37

From (2.4), the defect of invariance is then

$$\boldsymbol{\Delta} = (\boldsymbol{I} - \boldsymbol{P})\boldsymbol{f} = \begin{pmatrix} 0 \\ -\frac{dy(\xi)}{d\xi}\left(2 - \xi - y(\xi)\right) + \gamma\left(\sqrt{\xi} - y(\xi)\right) \end{pmatrix} \tag{2.9}$$

In this case, the manifold is smooth and $\frac{dy(\xi)}{d\xi}$ along the manifold can be accurately approximated numerically by second-order central differences.

In order to compare the manifold and its invariance with the ILDM, the Jacobian $\boldsymbol{J}$ of (2.7)

$$\boldsymbol{J} = \begin{pmatrix} -1 & -1 \\ \frac{\gamma}{2\sqrt{x}} & -\gamma \end{pmatrix} \tag{2.10}$$

is needed. The symmetrized Jacobian $\boldsymbol{J}_{sym} = \boldsymbol{J}\boldsymbol{J}^T$, which offers the advantage of real eigenvalues, λ, and orthogonal eigenvectors, $\boldsymbol{v}$, can be used to define the fast and slow invariant subspaces of (2.7) [13, 64]. Let us define the matrix $\boldsymbol{V}$ with a column partitioning given by the eigenvectors of $\boldsymbol{J}_{sym}$ ordered according to decreasing magnitude of the corresponding eigenvalues, $\boldsymbol{V} = (\boldsymbol{v}_{slow}, \boldsymbol{v}_{fast})$ and its inverse $\boldsymbol{V}^{-1} = \left(\ \widetilde{\boldsymbol{v}}_{slow}, \widetilde{\boldsymbol{v}}_{fast}\ \right)^T$. For $\gamma \gg 1$, the ILDM manifold, y_{ILDM}, can be obtained by setting the inner product of $\widetilde{\boldsymbol{v}}_{fast}$ with $\boldsymbol{f}$ [42, 64] equal to zero. Assuming that y is the intrinsic fast variable, the approximate form of slow manifold is

$$y = \sqrt{x}. \tag{2.11}$$

The ILDM manifold is plotted in Fig. 2.2(b) (dashed line) together with

several trajectories (dot-dashed lines) and the RRM manifold (solid line). Trajectories initialized at the leftmost boundary of the ILDM (open squares) and RRM (open circles) manifolds are also shown. In this case, the ILDM manifold is neither invariant nor slow, except close to the steady state. On the other hand, different solution trajectories are quickly attracted (Fig. 2.2(b)) to the RRM manifold, which is also found to be invariant.

For the initial condition $(x_0, y_0) = (0.1, 1.0)$, the temporal evolution of the state and the Euclidean norm of $\boldsymbol{\Delta}$ for the RRM and ILDM manifolds of system (2.7) are plotted in Fig. 2.3(a). The defect of invariance for the
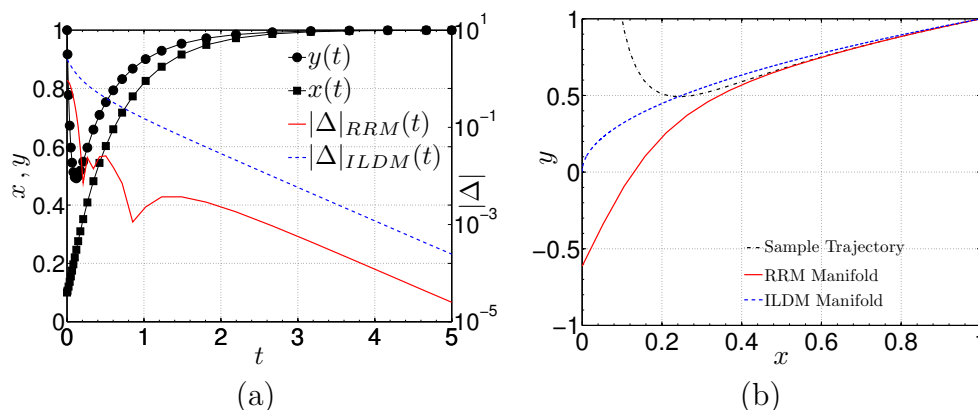
Figure 2.3: Analysis of ILDM and RRM manifold for (2.7). (a) Defects of invariance and temporal evolution of the state for a sample trajectory (b) Sample trajectory, ILDM and RRM manifolds in phase space for $\gamma = 20$.

RRM manifold is an order of magnitude lower than for ILDM, implying that the RRM manifold is a better approximation for the SIM. As it can be seen from Fig. 2.3(b), the trajectory is attracted to the RRM manifold at $(x, y) \simeq (0.4, 0.6)$. At this location, the defect of invariance for the RRM manifold is less than 0.03, while for ILDM it is approximately 0.6.

2.3 Chemical kinetics

Consider a homogeneous mixture of ideal gases consisting of n_s species and n_e elements reacting under constant pressure p in a closed system. The number of moles are represented by the vector $\mathbf{N} = (N_1, N_2, \cdots, N_{n_s})^T$ and the change in the chemical composition of the species, results from n_r reversible reactions between the n_s reactants M_i

$$\sum_{i=1}^{n_s} \nu'_{ik} M_i \rightleftharpoons \sum_{i=1}^{n_s} \nu''_{ik} M_i, \quad k = 1, \cdots, n_r \tag{2.12}$$
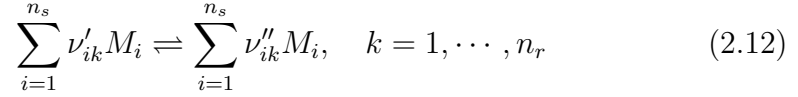
where ν'_{ik} and ν''_{ik} are the stoichiometric coefficients of species i in reaction k for the reactants and products, respectively. The rate of progress of reaction k is

$$q_k = k_{f_k} \prod_{i=1}^{n_s} [X_i]^{\nu'_{ik}} - k_{r_k} \prod_{i=1}^{n_s} [X_i]^{\nu''_{ik}}, \quad k = 1, \cdots, n_r \tag{2.13}$$

where $[X_i]$ denotes the molar concentration of species i and k_{f_k} and k_{r_k} are the forward and reverse rate constants having the modified Arrhenius form

$$k_{f_k} = A_k T^{\beta_k} \exp\left(\frac{-E_k}{R_c T}\right) \tag{2.14}$$

with A_k, β_k, E_k and R_c being the pre-exponential factor, temperature exponent, activation energy and ideal gas constant, respectively. The forward and reverse rate constants are related via the equilibrium constant, $K_{c_k}(T)$

$$k_{r_k} = \frac{k_{f_k}}{K_{c_k}} \tag{2.15}$$

The rate equation for species i is given by

$$\frac{d[X_i]}{dt} = \sum_{k=1}^{r}(\nu''_{ik} - \nu'_{ik})q_k, \quad i = 1, \cdots, n_s \qquad (2.16)$$

Using the reactor volume V, the change in the mole number of species i can be rewritten in the form of equation (2.1)

$$\frac{d\mathbf{N}}{dt} = \frac{d[V\boldsymbol{X}]}{dt} = \boldsymbol{f}(\mathbf{N}) \qquad (2.17)$$

The n_e elemental conservation constraints can be expressed in terms of an $n_e \times n_s$ elemental constraints matrix, $\mathbf{E}$, as [65]

$$\mathbf{EN} = \boldsymbol{\xi}^e \qquad (2.18)$$

where $\boldsymbol{\xi}^e$ is specified by the initial composition and E_{ji} denotes the number of atoms of element j in species i.

In a constant pressure adiabatic system the reactions proceed at constant enthalpy and the temperature evolution is governed by

$$\frac{dT}{dt} = -\frac{1}{\rho c_p}\Sigma_{i=1}^{n_s}h_i\dot{\omega}_iW_i$$

where, ρ is the mixture density and W_i, h_i and $\dot{\omega}_i$ molecular weight, enthalpy and production/destruction rate of species i. According to the second law of thermodynamics, the system under consideration is equipped with a concave state function, the entropy S, which attains its global maximum at equilibrium. The negative of entropy, which for ideal gases mixtures under

isobaric and isenthalpic conditions takes the form [58]

$$G = -S = -\frac{\sum_{i=1}^{n_s} X_i \left(s_i(T) - R_c \ln(X_i) - R_c \ln\left(\frac{p}{p_{ref}}\right) \right)}{\overline{W}} \qquad (2.19)$$

is a thermodynamic Lyapunov function for the dynamics defined by (2.17) in terms of s_i, the specific entropy of species i, $\overline{W} = \sum_{i=1}^{n_s} X_i W_i$ the mean molecular weight, p and p_{ref}, the system and reference pressure; $X_i = N_i / \sum_{j=1}^{n_s} N_j$ is the mole fraction of species i.

The equilibrium composition, $\mathbf{N}^{eq}$, is the solution of the constrained minimization problem:

$$\begin{aligned} \min \quad & G \\ \text{s.t.} \quad & \mathbf{EN} = \boldsymbol{\xi}^e \end{aligned} \qquad (2.20)$$

This Lyapunov function can be exploited not only to compute the equilibrium, but also for the derivation of the reduced description as described in the next section.

2.4   Construction of the reduced description

The local realization of the Relaxation Redistribution Method [58] constructs and tabulates SIMs with dimension n_d adaptively varying in different regions of the phase space. Adaptation of the dimension is based on the failure of the algorithm to converge after a fixed number of iterations, which is taken as an indicator that the SIM dimension should be increased.

However, the computational cost associated with the manifold representation on a grid and the retrieval of information from high-dimensional

tables imposes restrictions on the dimensionality of the slow manifold, the target being a two- or three-dimensional table [18]. A low-dimensional SIM is usually limited to a small neighborhood of phase space around the equilibrium point, leaving open the problem of its extension to cover all admissible states [66].

In this work, the global realization of the RRM with an a priori chosen manifold dimension is employed. In particular, an RCCE manifold, which provides 'good' manifolds as discussed in the introduction, with dimension up to three is used to define the initial SIM. The initial approximation is subsequently refined using RRM. For regions of the phase space in the neighborhood of the equilibrium, the method converges to the SIM. For states farther away, where no SIM with the chosen dimension exists, the refined Quasi-Equiibrium Manifold (QEM) defined below provides an accurate extension as will be shown in section 2.5. In addition to the parametrization of the SIM, the initial RCCE manifold defines the boundaries which are kept fixed during the application of RRM.

2.4.1   Initialization: the Quasi-Equilibrium Manifold

For systems equipped with a Lyapunov function, a reduced description can be obtained based on the notion of the Quasi-Equilibrium Manifold (QEM) [59] (known as Constrained Equilibrium Manifold (CEM) in the combustion literature [44, 45]). QEM assumes that the system relaxes to equilibrium through a sequence of quasi-equilibrium states at a rate controlled by a set of appropriate slowly-varying constraints $\boldsymbol{\xi}$ [44, 45, 59, 67]. Since the

Lyapunov function G decreases in time, a QEM can be interpreted as the constrained minimum of G.

In addition to the elemental conservation constraints (Eq. (2.18)), QEM imposes a priori n_d linear constraints on the system state defining the slow macroscopic variables

$$\boldsymbol{\xi}^d = (\mathbf{B}^d)\mathbf{N} \qquad (2.21)$$

$\mathbf{B}^d$ is an $n_d \times n_s$ matrix with rows obtained from the coefficients of the linear combinations of the number of moles providing the n_d slow parameterizing variables $\boldsymbol{\xi}^d$. Thus, the total number of constraints amounts to $n_c = n_e + n_d$, and the QEM is the map $\mathbf{N}^{QEM}(\boldsymbol{\xi})$, obtained by solving the following constrained convex minimization problem

$$\begin{aligned} \min \quad & G \\ \text{s.t.} \quad & \mathbf{B}\mathbf{N} = \boldsymbol{\xi} \end{aligned} \qquad (2.22)$$

Here, $\mathbf{B} = [\mathbf{E}\ \mathbf{B}^d]$ is the $n_c \times n_s$ constraint matrix and $\boldsymbol{\xi} = [\boldsymbol{\xi}^e\ \boldsymbol{\xi}^d]$ the constraint vector with n_c elements. The n_s-dimensional state $\mathbf{N}$ can then be parametrized by the n_c variables $\boldsymbol{\xi}$. For model reduction purposes, $n_c \ll n_s$.

In closed reactive systems, the elemental mole numbers must be conserved. Hence, $\mathbf{E}\mathbf{N} = \boldsymbol{\xi}^e$ is fixed upon definition of the fresh mixture condition. The constraint matrix $\mathbf{B}^d$ can be selected on the basis of numerical results of detailed solutions for similar problems, as suggested for example in [68]. Alternatively, a suitable parametrization can be extracted using the spectral decomposition of the Jacobian matrix evaluated at the equilibrium

point [41]. It should be pointed out that a QEM is typically neither an invariant nor a slow manifold [67].

The choice of a good set of constraints can be challenging. In addition to intuition and the mentioned approaches, CSP analysis of detailed simulations can aid in the selection [68]. The Level Of Importance (LOI), which finds the species associated with the short time scales by means of a combined species lifetime and sensitivity parameters, has also been used in the RCCE context [69]. In general, the constraints must [70, 71]

(a) be linearly independent

(b) constrained initial state should approximate the initial composition

(c) constrain global reactions in which reactants or intermediates go directly to products

(d) determine the energy and entropy of the system within experimental accuracy.

The RCCE method, which is based on the QEM approach can be used either as proposed originally [72–74], or in combination with other methods [75]. The most commonly employed slowly-changing constraints are the total number of moles (TM), the total number of radicals referred to active valence (AV), and free oxygen (FO), which refers to the reactions where the O-O bond is broken [67]. These RCCE linear constraints for hydrogen/air combustion are specified in Table 2.1. The RCCE manifold is unique and infinitely differentiable, and can be used even for states far from equilibrium [65, 70]. In this chapter, we exploit the QEM notion only to construct the

Table 2.1: Matrix B^d for the H_2/air mixture

Reduced variable	H$_2$	N$_2$	H	O	OH	O$_2$	H$_2$O	HO$_2$	H$_2$O$_2$
ξ_1^d=TM	1	1	1	1	1	1	1	1	1
ξ_2^d=AV	0	0	1	2	1	0	0	0	0
ξ_3^d=FO	0	0	0	1	1	0	1	0	0

initial approximation of the SIM and to define the manifold boundaries.

2.4.2   The global Relaxation Redistribution algorithm

As discussed in section 2.2, the boundaries of the initial grid shrink during relaxation. In the local RRM, reconstruction of the boundary points by re-stretching the relaxed grid to the fixed boundaries is done by linear extrapolation. However, such an approach cannot always guarantee physically meaningful values for the species concentrations. In order to avoid this difficulty, the boundary of the SIM can be fixed to the initial guess provided by the QEM, and the RRM procedure is applied only to the interior grid points.

The embarrassingly simple steps for the computation of the global manifold proceed as follows:

1. Choose the manifold dimension n_d and select the parameterizing variables ξ_i

2. Construct the n_d-dimensional QEM, $\mathbf{N}^{QEM}(\boldsymbol{\xi}^d)$, by solving the minimization problem (2.22). This manifold corresponds to constructing the initial grid indicated by the solid line with filled circles in Fig. 2.1(b).

3. Fix the grid boundaries to the boundaries of QEM

4. Relax the interior grid nodes by integrating

$$\frac{d\mathbf{N}}{dt} = \boldsymbol{f}(\mathbf{N}^{QEM}(\boldsymbol{\xi}^d)) \tag{2.23}$$

for a fixed time step Δt to obtain $\mathbf{N}^{relax}$.

As shown schematically in Fig. 2.1(b) (filled circles relaxing towards the open circles), this equation expresses the temporal evolution of composition confined onto the approximation of the SIM. The new locations of the relaxed nodes in the manifold parametrization space Ξ are then obtained from

$$\boldsymbol{\xi}_r^d = (\mathbf{B}^d)\mathbf{N}^{relax} \tag{2.24}$$

5. Redistribute the grid nodes back to the original locations in the manifold parametrization space

$$\mathbf{N}^{relax}(\boldsymbol{\xi}_r^d) \to \mathbf{N}^{RRM}(\boldsymbol{\xi}^d) \tag{2.25}$$

using interpolation through the scattered relaxed nodes. This is similar to finding the filled squares in Fig. 2.1(b), with the difference that boundaries are fixed and there is no extrapolation between the relaxed nodes.

6. Repeat steps 4-5 until the grid points do not change appreciably.

It should be pointed out that the reduced descriptions obtained by this algorithm are closely related to the ICE-PIC approach suggested by Ren et al. in [46], as both procedures construct invariant manifolds forced to pass through the fixed boundary points (QEM boundary points).

2.4.3   Rate equations for the slow variables

Once the slow invariant manifold is constructed, the temporal evolution of the reduced system along the SIM can be recast in the following general form in terms of the macroscopic slow variables $\boldsymbol{\xi}^d$ chosen to parametrize the SIM:

$$\frac{d\boldsymbol{\xi}^d}{dt} = (\mathbf{B}^d)\mathbf{P}\boldsymbol{f}(\mathbf{N}^{RRM}(\boldsymbol{\xi}^d)) \tag{2.26}$$

If the slow invariant manifold is known accurately, the vector field $\boldsymbol{f}$ is perfectly aligned with the manifold's tangent space and the state would never depart from the manifold. In most computational applications of practical interest, however, SIM approximations with different levels of accuracy are employed, and the chosen parametrization cannot completely decouple the fast and slow components. In these cases, $(\mathbf{B}^d)\boldsymbol{f}$ does not lie on the tangent space of the SIM and a projector $\mathbf{P}$ is needed to bring the state back to the manifold.

Different projectors have been proposed in the literature. The ILDM projector recovers the fast subspace to leading order [76], and the kernel of the projector is constructed using the fastest eigenvectors of the local Jacobian. Higher-order approximations can be constructed using the CSP basis vectors. Details on the ILDM and CSP projectors can be found in

[42, 77]. Another option for $\mathbf{P}$ is the thermodynamic projector [78], which can be constructed on the basis of the local tangent space to the SIM and the derivatives of a thermodynamic Lyapunov function (2.19) [79].

In the classical RCCE method, it is assumed that states of the system always remain on the QEM and the rate equations for the slow parameterizing variables is close to the tangent space of the manifold [67]. The n_s-dimensional composition space is decomposed into the n_d-dimensional *represented* subspace spanned by the rows of $\mathbf{B}^d$ and its orthogonal complement, the *unrepresented* subspace of dimension $n_s - n_d$. The projection is illustrated schematically in Fig. 2.4. The projection matrix then becomes the $n_s \times n_s$-dimensional identity matrix which implies that the rate of change in the unrepresented subspace is negligible. Therefore we rely upon the fact that fast motions are expected to mostly occur in the null space of the $\mathbf{B}^d$ matrix. The same approach was used in the applications of the results section. For a more detailed analysis of this projector see [75].

The following steps describe the implementation of reduced chemistry in a reacting flow simulation: (a) From the specified composition at time t_n, $\mathbf{N}_n = \mathbf{N}(t_n)$, and the thermodynamic conditions, the values for the parameterizing variables can be found using equation (2.21),

$$(\mathbf{B}^d)\mathbf{N}_n = \boldsymbol{\xi}_n^d \tag{2.27}$$

(b) The rate equations (2.26) for $\boldsymbol{\xi}^d$, are advanced in time to find $\boldsymbol{\xi}_{n+1}^d$, where $\mathbf{N}_n^{RRM}$ are the projected values of $\mathbf{N}(t_n)$ on the SIM.
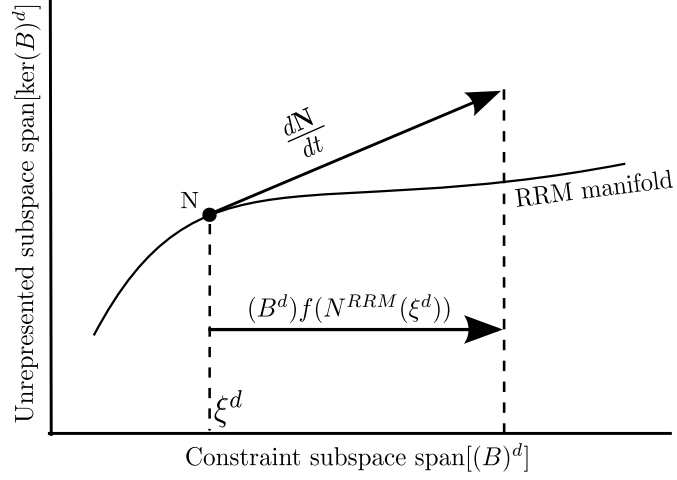
Figure 2.4: Project in the unrepresented subspace of RRM manifold. The projection is same as classical RCCE [67]

The reduced model can be tabulated in terms of either the reduced state $\mathbf{N}^{RRM}$ or of the projected right hand side of the evolution equations $(\mathbf{B}^d)\boldsymbol{f}(\mathbf{N}^{RRM})$. In the former case, interpolation of the tabulated data is used to retrieve the composition vector corresponding to $\boldsymbol{\xi}^d_{n+1}$. In the latter, the right hand side of (2.26) is obtained directly to proceed with the integration of the reduced system and the compositions can be obtained separately in a post-processing step.

The overall computational cost for the integration of the full system of n_s differential equations is thus replaced by the cost of integrating n_d differential equations and of interpolation. The following practical issues should be pointed out: (i) Choosing the appropriate constraints with respect to the initial composition is important. The kernel of $\mathbf{B}^d$ should not be spanned by the $\boldsymbol{f}(\mathbf{N}^{RRM}_n(\boldsymbol{\xi}^d))$ vector, since in that case $\frac{d\boldsymbol{\xi}^d}{dt}$ becomes zero and there is no temporal evolution of $\boldsymbol{\xi}^d$; (ii) Interpolation can affect the result strongly

as shown in [80]. This effect can be controlled by refining the table and/or using appropriate interpolation methods, albeit at higher computational cost; (iii) By construction, the approach presented here guarantees that the equilibrium will be accurately captured by the reduced description. This appears to not always be the case with reduced mechanisms proposed in the literature; (iv) In problems like the ignition delay time considered in the next section, the projection of the initial state on the manifold is crucial for the comparison with the prediction of the detailed reaction mechanism. In the literature, the comparison is often made by taking the initial state to lie *on* the manifold. In the auto-ignition validation of the next section good results are obtained by comparing the detailed solution with those obtained by projecting the initial state on the manifold using the constrained equilibrium assumption.

2.5 Validation and discussion

2.5.1 Auto-ignition of homogeneous mixtures

The global RRM method is applied to a homogeneous H_2/air mixture using the detailed reaction mechanism of Li et al. [17]. ($n_s = 9$ species and 21 reactions) at atmospheric pressure and different initial temperatures T_0.

The initial reactant composition is that of a stoichiometric mixture ($N_{H_2}^0 = 1.0$, $N_{O_2}^0 = 0.5$ and $N_{N_2}^0 = 1.881$ mole), while the remaining species are assigned the chemically insignificant positive values $N = 10^{-12}$ mole to ensure strictly positive species compositions at the constrained equilibrium

state and guarantee the existence and uniqueness of the solution to the minimization problem (2.22) [67].

The equilibrium point (steady state) can be computed by minimizing the Gibbs function under constant pressure and enthalpy. Then, the initial and equilibrium states are projected on the manifold parametrization space, Ξ, using (2.21). Different combinations of constraints for hydrogen combustion have been investigated in the literature [67, 70]. The TM and AV constraints (Table 2.1) have been found to give better agreement with respect to ignition delay times for a wide range of thermodynamic conditions and are chosen for the $\boldsymbol{\xi}$ parameterization. Starting from a sufficiently large range in the parametrization space that contains the initial and steady states, the CEQ code [81,82] is used for the construction of the RCCE-based initial manifold as discussed in section 2.4.2. The code computes the constrained equilibrium state by minimizing the Gibbs function under fixed pressure and enthalpy; the projection of the computed initial manifold on Ξ is shown in Fig. 2.5. The boundary nodes are then fixed, and the RRM procedure is applied to the interior nodes. For the redistribution step, the linear Shepard method implemented in the SHEPPACK package [83] is used for interpolation,

$$\mathbf{N}^{RRM}(\boldsymbol{\xi}^d) = \frac{\sum_{k=1}^{n_{gp}} \alpha_k(\boldsymbol{\xi}^d)\mathbf{N}^{relax}(\boldsymbol{\xi}_r^d)}{\sum_{k=1}^{n_{gp}} \alpha_k(\boldsymbol{\xi}^d)} \tag{2.28}$$

where n_{gp} is the total number of grid points and the weights $\alpha_k(\boldsymbol{\xi}^d)$ are
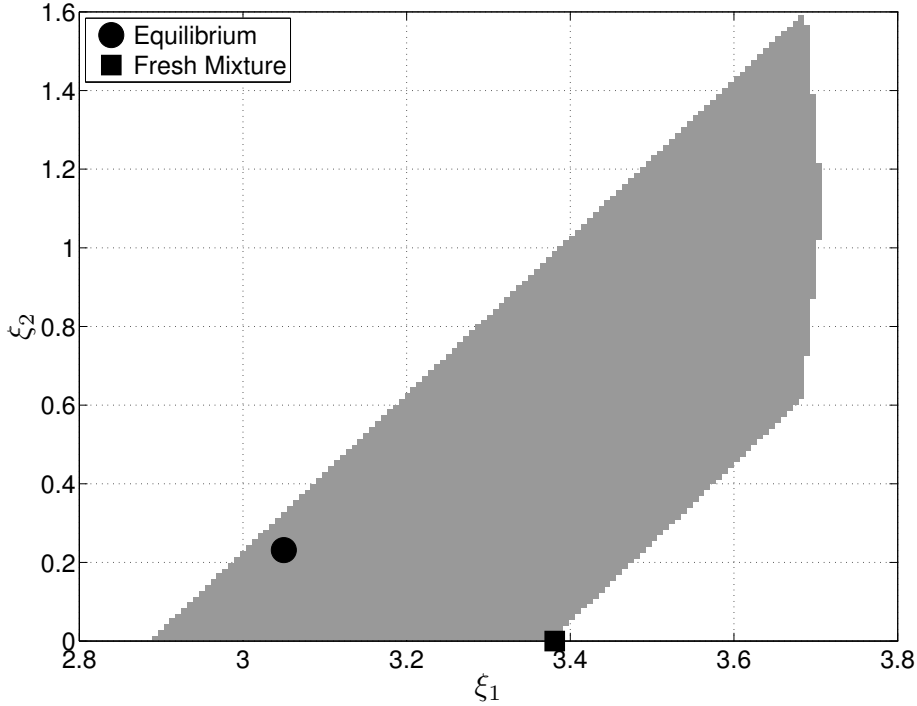
Figure 2.5: Projection of manifold (grid) onto Ξ. The initial grid should contain both the fresh mixture and equilibrium point, and extend in the manifold parametrization space as far as the QEM convex minimization calculations converge.

defined as

$$\alpha_k(\boldsymbol{\xi}^d) = \frac{1}{\|\boldsymbol{\xi}^d - \boldsymbol{\xi}_r^{d(k)}\|_2^2} \tag{2.29}$$

For initial temperature $T_0 = 1500$ K, the two-dimensional RCCE and global RRM manifolds for selected species are plotted in Fig. 2.6 together with the trajectory obtained using the detailed mechanism (thick solid line). For the major species, the global RRM manifold brings only a slight improvement over the RCCE manifold, while for HO_2 and H_2O_2 the improvement is significant. As it can be seen in Fig. 2.6, the RCCE manifold is not invariant. This is more clearly seen in the temporal evolution of the temperature and
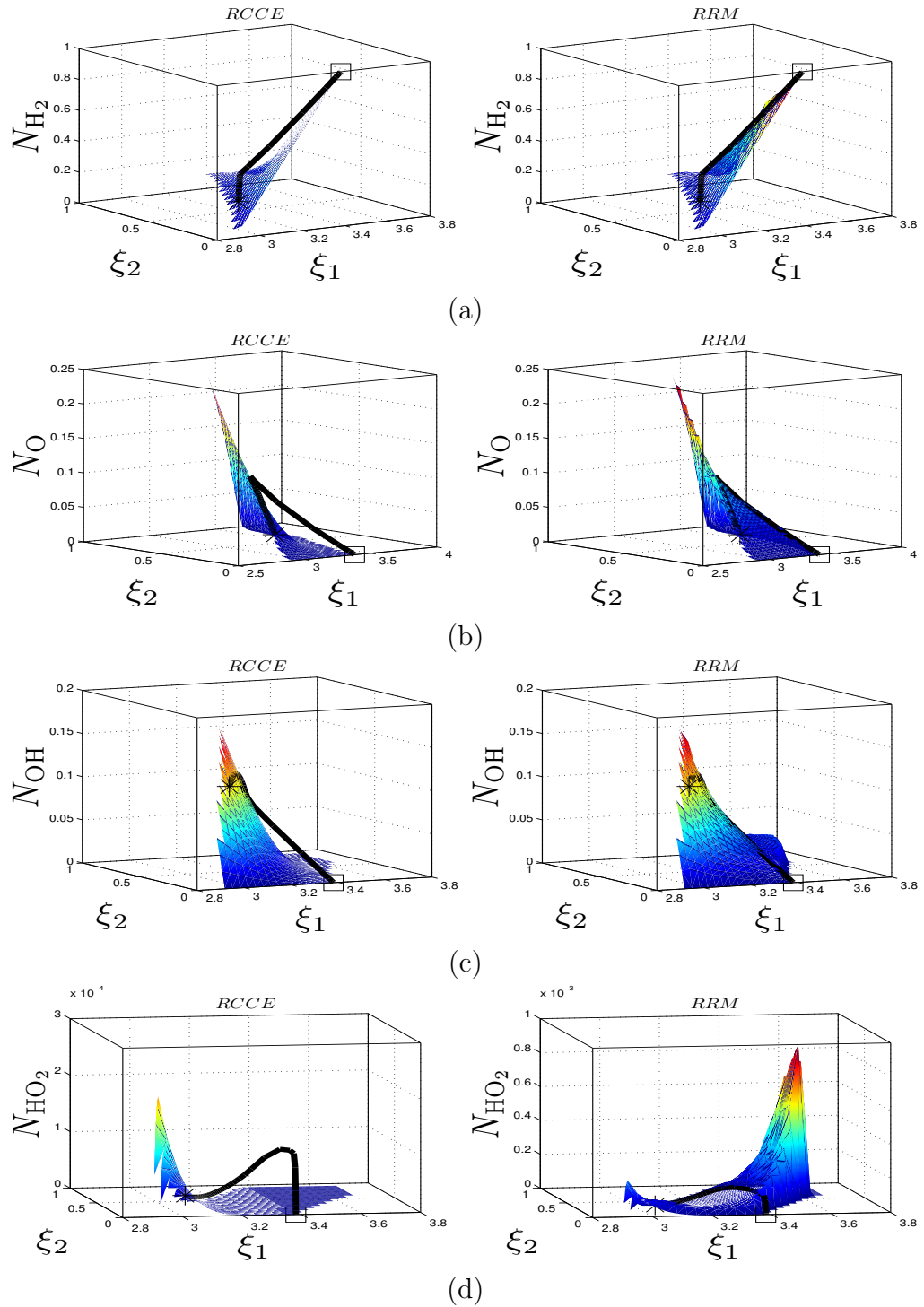
Figure 2.6: Comparison of the RCCE (left column) and RRM (right column) manifolds for $T_0 = 1500$ K. ($\square$: fresh mixture; $\star$: equilibrium point; $-$: detailed kinetics trajectory).

species mass fractions, plotted in Fig. 2.7. Good agreement is found with the detailed description for the temperature and major reactants as well as the radicals with high enough concentration. Far away from equilibrium, the RCCE manifold strongly underpredicts the concentration of HO_2 and H_2O_2.
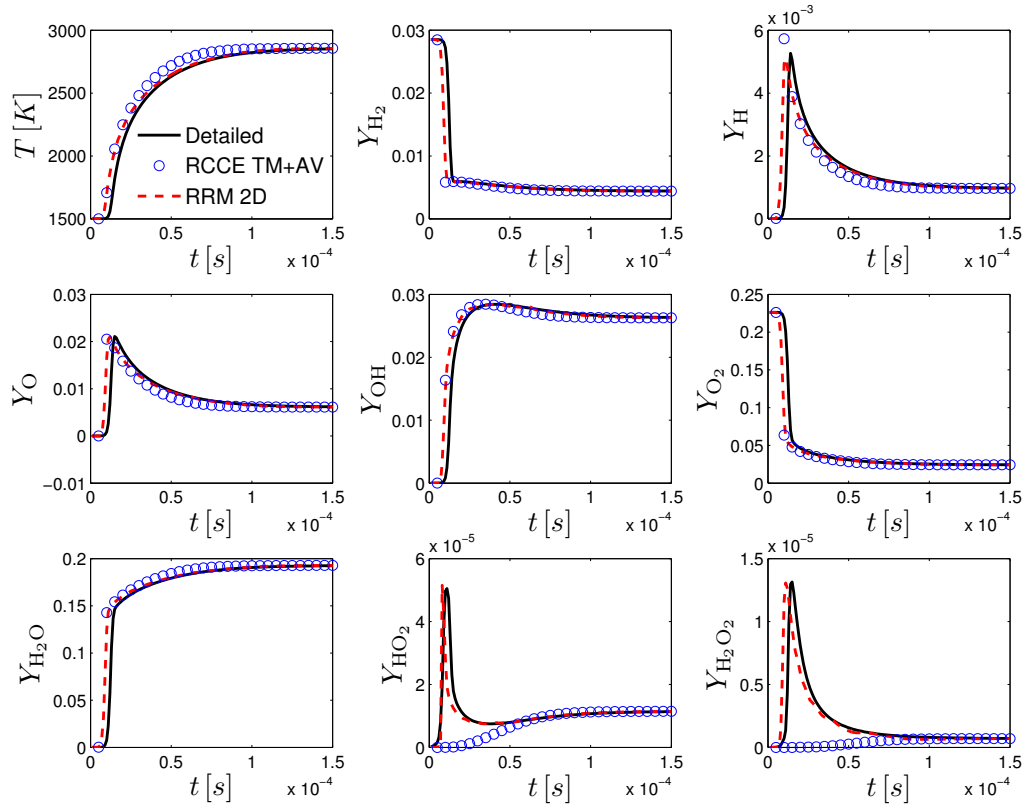
Figure 2.7: Time histories of the temperature and species mass fractions for H_2/air autoignition with unburnt temperature $T_0 = 1500\,K$.

The time history of the weighted root mean square norm as used for error estimation in [84] of the defect of invariance vector is plotted in Fig. 2.8(a) together with the temperature profiles computed using the detailed and reduced descriptions. After $40\,\mu s$, the defect drops below 10^{-4}

and the detailed and reduced models are in good agreement. This illustrates that the defect of invariance is a convenient indicator of the accuracy of the reduced description. During the initial transient, a higher-dimensional manifold should be used.

The number of right hand side function evaluations n_{fe} during integration can be used as an indicator for the stiffness. Figure 2.8(b) shows the temperature and n_{fe} obtained by using the stiff ODE integrator DVODE [84] with an output time step $\delta t = 10^{-5}$ (the integrator adapts the time step during integration from time t to $t + dt$). The initial composition for the detailed mechanism was the stoichiometric mixture, while for the reduced description its projection on the RRM manifold was used. With the exception of a single time instant close to ignition, n_{fe} is lower for the reduced model during the whole integration interval.

At a lower initial temperature $T_0 = 1000$ K, the 2-D manifold can no longer provide an accurate reduced description (Fig. 2.9). The construction of a 3-D slow manifold is straightforward starting from an initial manifold constructed using all constraints of Table 2.1. The results obtained with RCCE with two (open squares) and three (open circles) constraints, the RRM 2-D (dot-dashed line) and 3-D (dashed line) manifolds are compared with the detailed evolution (solid line) in Fig. 2.9. While the 3-D RCCE manifold results in small improvement, the increase in the manifold dimension of the RRM manifold leads to very good agreement with respect to the prediction accuracy of the ignition delay time and the temporal evolution of temperature and species, with the exception of the $Y_{\mathrm{H_2O_2}}$ profile which

(a)

(b)
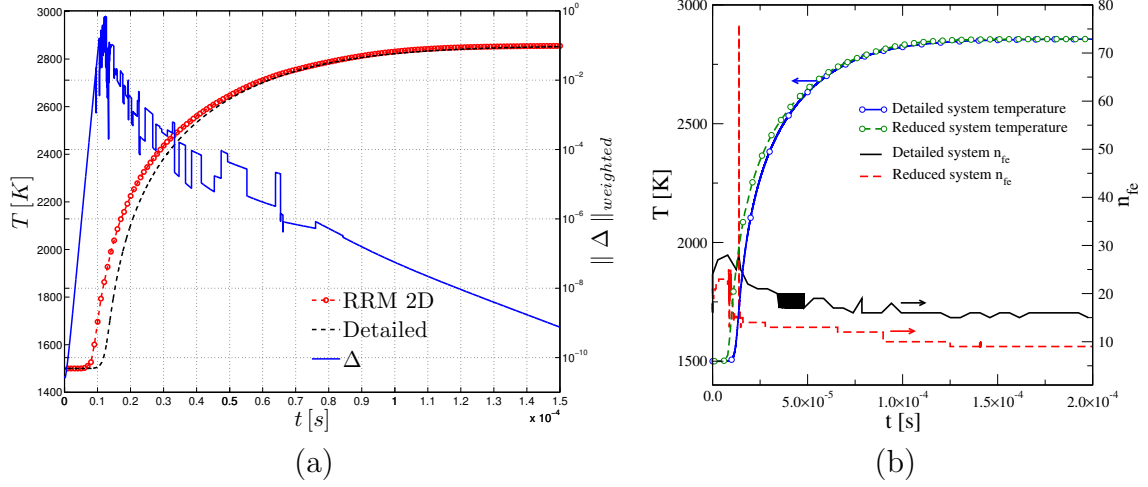
Figure 2.8: (a) Comparison of the temperature profiles obtained with the detailed and the reduced 2-D RRM description and evolution of the norm of the defect of invariance for $T_0 = 1500$ K; (b) Comparison of temperature evolution and number of source term evaluations n_{fe} obtained with the detailed mechanism and the reduced 2-D RRM description at $T_0 = 1500$ K.

displays a noticeable deviation from the detailed mechanism profile. The ignition delay times, τ_{ig}, defined as the time corresponding to the inflection point of the temperate profile are summarized in Table 2.2. The magnitude

Table 2.2: Comparison of ignition delay times deduced from detailed and reduced models.

Method	$\tau_{ig}(sec)$
Detailed	0.000213
RCCE TM+AV	0.000169
RCCE TM+AV+FO	0.000178
RRM 2D	0.000170
RRM 3D	0.000207

of the real part of the six non-trivial eigenvalues of the Jacobian matrix during the temporal evolution for $T_0 = 1000$ K and $T_0 = 1500$ K are reported in Fig. 2.10. The absolute value of the inverse of the eigenvalues
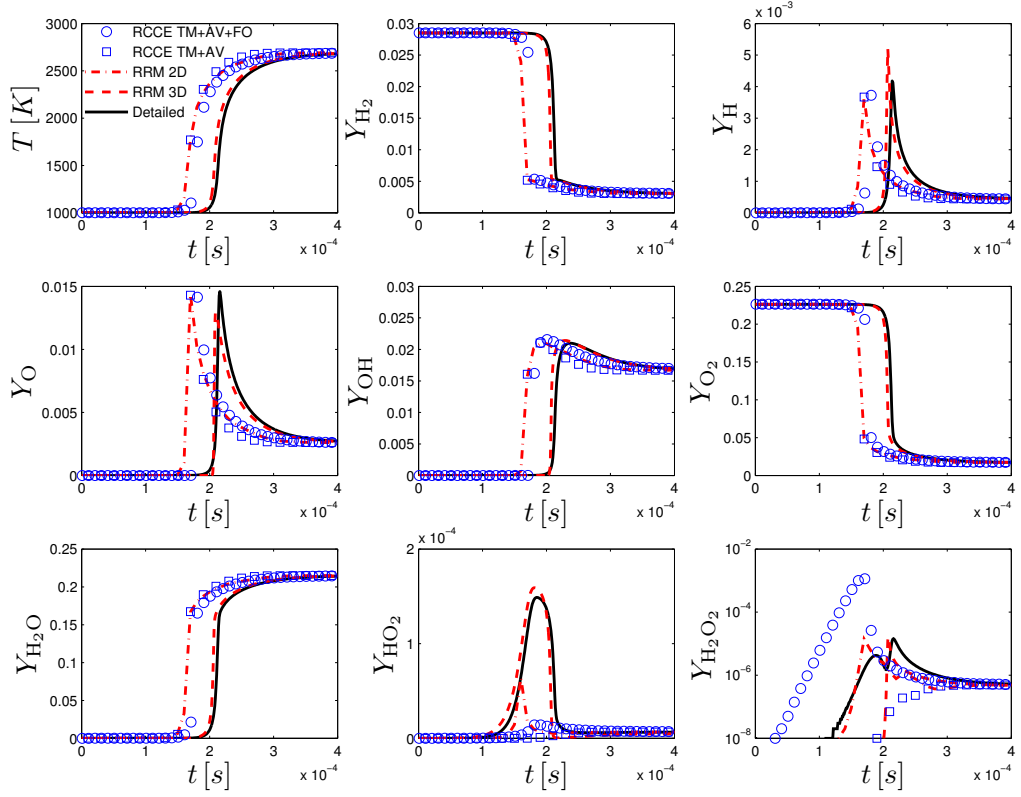
Figure 2.9: Temperature and species mass fractions as the function of time for H_2/air auto-ignition, $T_0 = 1000$ K. Detailed, RCCE with 2 Constraints, RCCE with 3 Constraints, RRM 2D manifold, RRM 3D manifold are compared.

determine the time scales of the chemical modes and the ratio λ_f/λ_s of the most to the less negative eigenvalues, an estimation for stiffness. For $T_0 = 1000$ K, the gap is $\lambda_f/\lambda_s \simeq 8.5 \times 10^8$, while for $T_0 = 1500K$ the ratio becomes $\lambda_f/\lambda_s \simeq 5.6 \times 10^5$, reflecting the higher stiffness at lower temperatures. Eigenvalues with positive real part indicating explosive behavior were found initially in both cases and time intervals where the eigenvalues cross and become complex pairs were observed during the evolution from the initial to the equilibrium state. Manifolds of higher dimensions would
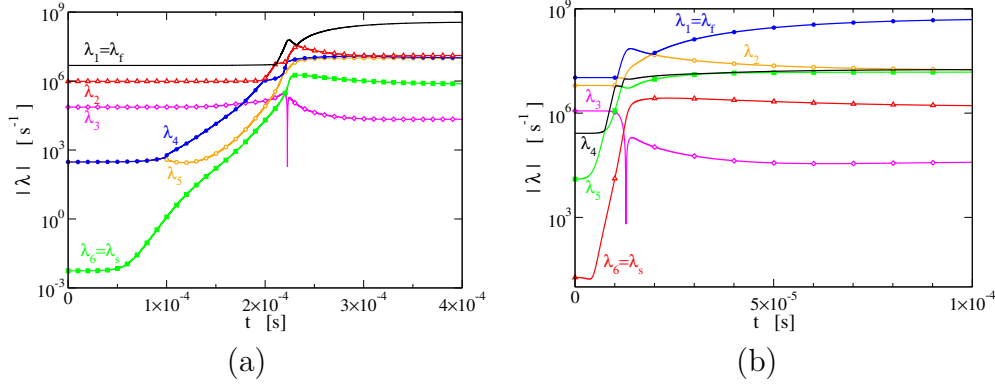
Figure 2.10: Temporal evolution of the six non-trivial eigenvalues of the Jacobian along the solution trajectory: (a) $T_0 = 1000$ K, (b) $T_0 = 1500$ K.

be needed to capture more accurately the reduced dynamics in these intervals, as was done in the adaptive version of RRM [58]. Careful examination of Fig. 2.10 for $T_0 = 1500$ K reveals that eigenvalue crossings correspond to jumps in (a) the defect of invariance vector (Fig. 2.8(a)) and (b) the number of source term evaluations n_{fe} (Fig. 2.8(b)). The effect of eigenvalues crossing on the quality of reduced model is discussed in [85]. It nevertheless appears that these short intervals do not affect the quality of the manifold significantly.

2.5.2 Premixed laminar flame

The steady, atmospheric, adiabatic, one-dimensional laminar premixed flame of a stoichiometric hydrogen/air mixture and multi-component transport properties was considered in order to study the ability of the 2-D RRM manifold constructed from the homogeneous auto-ignition of an unburnt mixture at $T_u = 700$ K to reconstruct the unrepresented variables in a case where transport phenomena play a dominant role. A similar procedure was

used for the validation of the ICE-PIC manifold by Ren el al. [46].

In this case, the manifold parametrization becomes important since in the general case of non-unity Lewis numbers it is difficult to solve the partial differential equations even when the parameterizing variables are linear combinations of the original variables [86]. Here, the quasi-equilibrium manifold was constructed using the mole fractions of H_2O and H_2 as slow constraints ($\xi_1 = X_{H_2O}$ and $\xi_2 = X_{H_2}$). The RRM refinement process was applied starting from the QEM to find the global two dimensional manifold for $T_u = 700$ K. The species concentrations as a function of the distance,
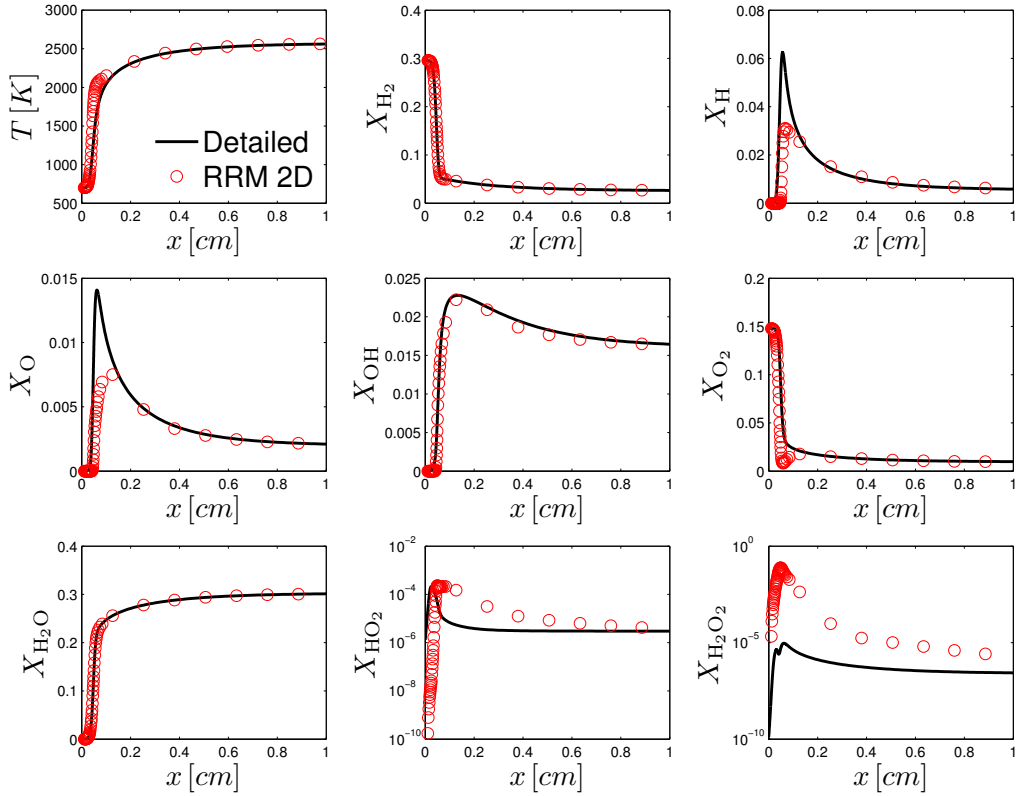
Figure 2.11: Comparison of the temperature and species mole fractions profiles computed by PREMIX (lines) and reconstructed using the 2-D RRM manifold (symbols) for unburnt mixture at $T_0 = 700$ K.

x, is computed using PREMIX from the CHEMKIN application suite [87]. The local values of X_{H_2} and X_{H_2O} from the detailed chemistry 1-D flame structure were used to reconstruct the remaining species using the RRM manifold. The agreement for the major species and temperature between the detailed solution and the reconstruction is excellent (Fig. 2.11). The largest differences are observed for the H_2O_2 species and they can be mainly attributed to the incorrectly predicted value of QEM at the "cold" (unburned mixture) boundary. In addition to low dimensionality effects, molecular diffusion in laminar flames can drive the compositions away from the manifold, potentially contributing in the differences observed in the O and H radicals profiles. Similar observations are reported in the literature, where different methods of projecting the diffusion term onto the manifold were studied (see, for example, [76, 88])

2.6 Summary and Conclusions

In this chapter we presented an algorithm based on the Relaxation Redistribution Method (RRM) for the construction of the Slow Invariant Manifold (SIM) of an a priori chosen dimension which covers a large fraction of the admissible composition space that includes the equilibrium as well as the initial state.

The manifold parametrization and boundaries are determined with the help of the Rate Controlled Constrained Equilibrium (RCCE) method, which also provides the initial guess for the SIM. The guess is iteratively refined and the converged manifold is tabulated. The method is easy to

implement and robust to use for the construction of reduced manifolds of high dimensionality, which were found to be invariant over extended regions of the admissible space. A criterion based on the departure from invariance is proposed to find the region over which the reduced description is valid. The accuracy of the method was assessed by comparing trajectories for auto-ignition calculations of homogeneous H_2/air mixtures at different initial temperatures T_0. At $T_0 = 1500$ K, a 2-D manifold is found to capture accurately both the ignition delay time and the temporal evolution of all the species and shows significant improvement with respect to the low concentration species (HO_2 and H_2O_2) compared to an RCCE manifold. At T_0=1000 K, a 3-D manifold is needed to reproduce accurately the detailed dynamics with the exception of the pre-ignition profiles of H_2O_2 while, constructing the 3-D manifold is barely reported in chemical kinetics reduction literature.

The significant reduction in the number of source term evaluations indicates that the reduced descriptions are less stiff. However, similar to all other reduction methods based on tabulation, fast table searching and interpolation algorithms are essential for the overall efficiency of the reduced scheme.

The 2-D RRM manifold can reconstruct the laminar premixed flame structure fairly accurately compared with the results obtained with the detailed mechanism, indicating that it can be used in multidimensional simulations where transport properties play a dominant role.

Chapter 3

Spectral Quasi Equilibrium

Manifold

3.1 Introduction

Entropy and entropy production are two well-studied thermodynamic functions, which can be more informative than the original system dynamics. Entropy can be considered as a Lyapunov function of a closed system which can create a logical bridge between thermodynamics and dynamical system analysis. For example, trajectories with minimal entropy production have been considered as candidates for one-dimensional slow manifolds [47]. On the other hand, it can be assumed that physical and chemical kinetic systems evolve in the vicinity of Quasi Equilibrium States (QES), where entropy is maximized under certain constraints [59].

In physical kinetic, the works on hydrodynamic limits of the Boltzmann equation is an example of reducing the infinite system of moments of particle distribution to a smaller number of representative moments. The

closure of this infinite system should approximate the hierarchy of moments, and can be found by assuming that the particle distribution is near the local equilibrium [55]. The closed system of moments can be derived by a non-perturbative systematic approach, assuming that the distribution is mostly embedded in the low dimensional Quasi Equilibrium Manifold (QEM) of the system [89–91].

In chemical kinetics, as explained in chapter 2, Rate-Controlled Constrained Equilibrium (RCCE) is a well known QEM-based method, which uses the maximum entropy principle and assumes that: (i) slow reactions impose constraints on the system composition which correspond to slow relaxation towards equilibrium, and (ii) fast reactions equilibrate the system. Consequently, the system relaxes towards chemical equilibrium through a sequence of constrained equilibrium states (which belong to QEM) at a rate controlled by the slowly changing constraints [45, 70, 74].

Originally, chemical intuition guided by numerical simulations were used for the selection of constraints in the RCCE method [70], implying that good knowledge of detailed chemical kinetics is necessary for finding the class of slow and fast reactions. Other studies, tried to determine the species which must be retained in the reduced model based on timescale analysis (e.g Level of Importance (LOI) [69]), generalizing the parametrization of the RCCE manifold for any comprehensive reaction mechanism.

The majority of fast time scales are exhausted around the equilibrium point, therefore a low dimensional SIM is limited around that state. To cover the entire admissible space with a uniform SIM, one should find a way

to extend the manifold. The quasi-equilibrium manifold has been proposed in the literature both for species reconstruction (manifold extension) for the states far from equilibrium and for obtaining the manifold boundaries [46, 92].

In the spirit of the QEM, the Spectral Quasi Equilibrium Manifold (SQEM) has been employed as an initial manifold which is subsequently refined towards the SIM [13, 41, 93]. The method has been applied to small systems of ODEs (up to hydrogen combustion which is effectively six dimensional). In this chapter, the ability of the spectral quasi-equilibrium method to provide general constraints, which do not resort on intuition, is investigated and applied for the construction of quasi-equilibrium manifolds for hydrogen, syngas and methane combustion.

The method is first validated through the two-dimensional Michaelis-Menten kinetic scheme, where the quality of the reduction is discussed and related to the temporal evolution and the gap in the spectra of eigenvalues and Lyapunov exponents. In addition to simple enzyme kinetics, the ability of the method is explored for detailed combustion mechanisms. The temporal evolution of temperature and species concentrations deduced from reduced and detailed models are used as indicators of the quality of reduction, showing the potential of SQEM for the reconstruction of species concentrations and temperature profiles. The comparison also shows that the spectral constraints show better agreement with the detailed model compared to the classical RCCE constraints.

3.2 Equilibrium and quasi-equilibrium

Lyapunov functions can be more informative and fundamental than the original system (2.17) itself. For example, even for dynamical systems whose detailed behavior is unpredictable, Lyapunov functions can be used as the quantity, measuring how "complex" or unpredictable, the motion is [94–96].

The entropy S, as the distinguished Lyapunov function, which monotonically increases along all possible trajectories in phase space is widely used in physical and chemical kinetics to describe different features of the system. Because entropy is increasing monotonically through the relaxation, the global equilibrium state corresponds to the global maximum entropy state. Therefore, instead of integrating the system for long (more formally infinite) time, one can find the equilibrium via maximization of the entropy.

The equilibrium composition, $\boldsymbol{N}^{eq}$, is the constrained minimum of the thermodynamic potential $G(\boldsymbol{N}, p, T)$ (Eq. (2.20)). The concept of the Quasi-Equilibrium Manifold stems from Grad's approximation for the closure of the system of moments. "*Of course, to any degree of approximation, these solutions approximate to only a small part of the manifold of solutions of the Boltzmann equation [55].*" The QEM is the loci of states $\boldsymbol{N}^{QEM}$, obtained by solving the following constrained optimization problem,

$$
\begin{aligned}
\max \quad & S \\
\text{s.t.} \quad & \boldsymbol{\xi} = \mathscr{G}(\boldsymbol{N})
\end{aligned}
\tag{3.1}
$$

where, $\boldsymbol{\xi} = \mathscr{G}(\boldsymbol{N})$ is the set of selected moments and the map $\mathscr{G}^{-1} : \boldsymbol{\xi} \longrightarrow \boldsymbol{N}$

is a closure assumption [59]. The system of equations (3.1) is the same as system (2.22). As we know, the global equilibrium is the state where all processes are relaxed. We consider the case where only fast processes of the system are relaxed. This Quasi Equilibrium State (QES) can be found similarly by maximizing the entropy but under additional constraints on the original dynamics (see Eq. (2.21)).

3.2.1 Spectral quasi-equilibrium manifold

The general form of the constraint matrix $\boldsymbol{B}^d$ in (2.21) reads

$$\boldsymbol{B}^d = \begin{bmatrix} \boldsymbol{v}_1 \\ \vdots \\ \boldsymbol{v}_{n_d} \end{bmatrix} \tag{3.2}$$

where $\boldsymbol{v}_i$ is a n_s-dimensional vector defining the ith constraint. A different set of constraints for the construction of the pertinent quasi-equilibrium was proposed by Gorban and Karlin [13] based on the left eigenvectors of the Jacobian system at equilibrium,

$$J_{ij}^{eq} = \left[\frac{\partial f(N_i)}{\partial N_j} \right]_{\boldsymbol{N} = \boldsymbol{N}^{eq}} \tag{3.3}$$

where $\boldsymbol{f}$ for the case of homogeneous reactor is introduced in (2.17).

Let us define the matrix $\boldsymbol{V}^{eq}$ with a column partitioning given by the right eigenvectors of $\boldsymbol{J}^{eq}$ ordered according to decreasing values of the cor-

responding eigenvalues, $\boldsymbol{V}^{eq} = [\tilde{\boldsymbol{v}}^{eq}_{slow}, \tilde{\boldsymbol{v}}^{eq}_{fast}]$ and its inverse

$$\boldsymbol{V}^{eq^{-1}} = \left(\boldsymbol{v}^{eq}_{slow}, \boldsymbol{v}^{eq}_{fast}\right)^T. \tag{3.4}$$

The $\boldsymbol{v}^{eq}_{slow}$ at equilibrium can be used as the vectors which define the direction of slow processes leading the relaxation towards the final state, so that the rows of $\boldsymbol{B}^d$ in Eq. (3.2) are the first n_d slow left eigenvectors at equilibrium.

The construction of SQEM is local, hence, instead of constructing and tabulating the manifold, the subsequent states of detailed models can be compared with the evolution of spectral quasi-equilibrium states (SQES). Before considering application of the above SQEM to combustion mechanisms, let us consider a simple example.

3.2.1.1   Example: Reversible Michaelis-Menten mechanism

The reversible Michaelis-Menten mechanism is a simple enzyme reaction where enzyme E binds to a substrate S to form the intermediate complex ES which is then converted into the product P, releasing the free enzyme E [97]

$$\text{S} + \text{E} \underset{k_{r1}}{\overset{k_{f1}}{\rightleftharpoons}} \text{ES} \underset{k_{r2}}{\overset{k_{\text{cat}}}{\rightleftharpoons}} \text{E} + \text{P} \tag{3.5}$$
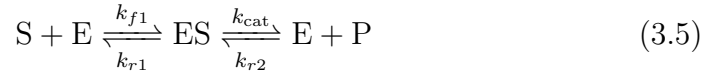
Here, k_{f1}, k_{cat} and k_{r1}, k_{r2} are respectively the rate constants of the forward and reverse reactions. The system of differential equations describing the

temporal evolution of species concentrations is

$$\frac{d[\text{S}]}{dt} = -k_{f1}[\text{S}][\text{E}] + k_{r1}[\text{ES}] \tag{3.6a}$$

$$\frac{d[\text{E}]}{dt} = -k_{f1}[\text{S}][\text{E}] + k_{r1}[\text{ES}] + k_{\text{cat}}[\text{ES}] - k_{r2}[\text{E}][\text{P}] \tag{3.6b}$$

$$\frac{d[\text{ES}]}{dt} = k_{f1}[\text{S}][\text{E}] - k_{r1}[\text{ES}] - k_{\text{cat}}[\text{ES}] + k_{r2}[\text{E}][\text{P}] \tag{3.6c}$$

$$\frac{d[\text{P}]}{dt} = k_{\text{cat}}[\text{ES}] - k_{r2}[\text{E}][\text{P}] \tag{3.6d}$$

where $[\text{X}_i]$ denotes the molar concentration of species i. In the absence of an analytical solution, two approaches, the quasi-equilibrium approximation and the steady-state assumption, have been used in the literature to find an expression for the rate of the catalytic step. The Michaelis-Menten equilibrium analysis is valid if the substrate reaches equilibrium on a much faster timescale than the product is formed [97], i.e.

$$\frac{k_{\text{cat}}}{k_{r1}} \ll 1 \tag{3.7}$$

The geometrical picture of the phase space evolution can be found in [98,99].

The system (3.6) is constrained by two constants for the total enzyme and total substrate,

$$[\text{E} + \text{ES}] = \xi_1^e \tag{3.8a}$$

$$[\text{S} + \text{ES} + \text{P}] = \xi_2^e \tag{3.8b}$$

which can be recast in the form (2.18) with $\boldsymbol{E} = \begin{bmatrix} 0 & 1 & 1 & 0 \\ 1 & 0 & 1 & 1 \end{bmatrix}$. The nonlinear system (3.6) is therefore effectively two-dimensional. The phase portrait for $\xi_1^e = 1.0$ and different reactions rates are shown in Fig. 3.1 where the positive semiorbits $\bigcup_{t \geq 0} \boldsymbol{f}(\boldsymbol{N}(t))$ for different initial conditions are projected on the two-dimensional $[S] \times [ES]$ plane. It can be seen that after short tran-
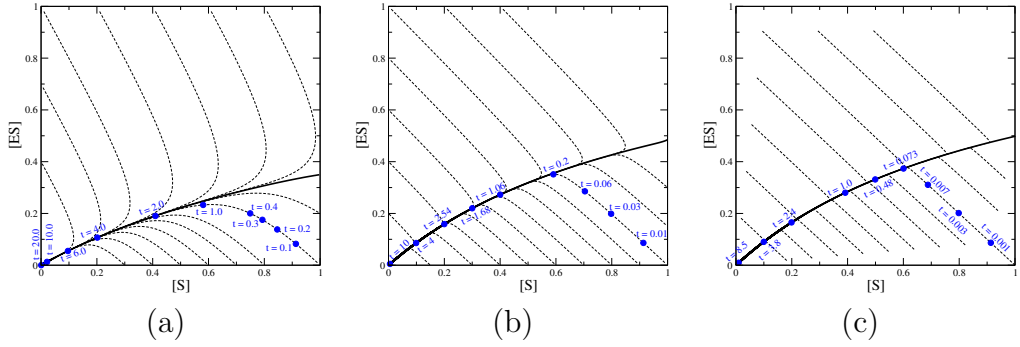
Figure 3.1: The phase portrait in $[S] \times [ES]$ space for Michaelis-Menten mechanism with $\xi_1^e = 1.0$, $k_{\text{cat}} = 1.0$ and $k_{r2} = 10^{-5}$ (a) $k_{1f} = k_{1r} = 1$, (b) $k_{1f} = k_{1r} = 10$, (c) $k_{1f} = k_{1r} = 100$; Dashed line: sample trajectories, solid line: slow manifold, circles: discrete times for selected trajectories.

sients trajectories (dashed lines) are attracted to a one-dimensional manifold (thick solid line) and then relax towards the zero-dimensional manifold (equilibrium point). For the trajectory initialized with $[ES]_0 = [P]_0 = 0$ and $[S]_0 = [E]_0 = 1.0$, the corresponding discrete time instants are also marked for all cases in Fig. 3.1. The decrease in $\frac{k_{\text{cat}}}{k_{r1}}$ ratio results in faster attraction to the low dimensional manifolds.

Gorban and Shahzad [100] proposed $G = -\Sigma_{i=1}^{4}[X_i]\{\ln([X_i]/[X_i]^{eq}) - 1\}$ as a Lyapunov function for this mechanism. As discussed before, for the system of ODEs (3.6) the spectral quasi-equilibrium states, can be found by

solving the convex optimization problem (2.22). In this case the constraint matrix is one dimensional, and it is taken to be equal to the slowest left eigenvector at equilibrium, $[\boldsymbol{B}^d]_{1\times 4} = \boldsymbol{v}^{eq}_{slow}$, hence, $[\boldsymbol{B}]_{3\times 4} = [\boldsymbol{E}; \boldsymbol{B}^d]$.

For the chosen trajectory ($[ES]_0 = [P]_0 = 0$ and $[S]_0 = [E]_0 = 1.0$), the SQESs are compared with the detailed solution in Figs. 3.2, 3.3 and 3.4; the evolution of the eigenvalues, $\boldsymbol{\lambda}$ and the Lyapunov exponents [101],

$$\boldsymbol{\Lambda}(\boldsymbol{N}, \delta\boldsymbol{N}) = \lim_{T\to\infty}(1/T)\log|(D_{\boldsymbol{N}}\boldsymbol{f}^T)\delta\boldsymbol{N}|$$

computed using the algorithm of [102], are also presented along the trajectory. The eigenvalues can identify the timescale gap where the trajectory is close to the slow manifold while Lyapunov exponents are providing more accurate information about the spectral gap in nonlinear dynamics even far from slow manifolds [103].
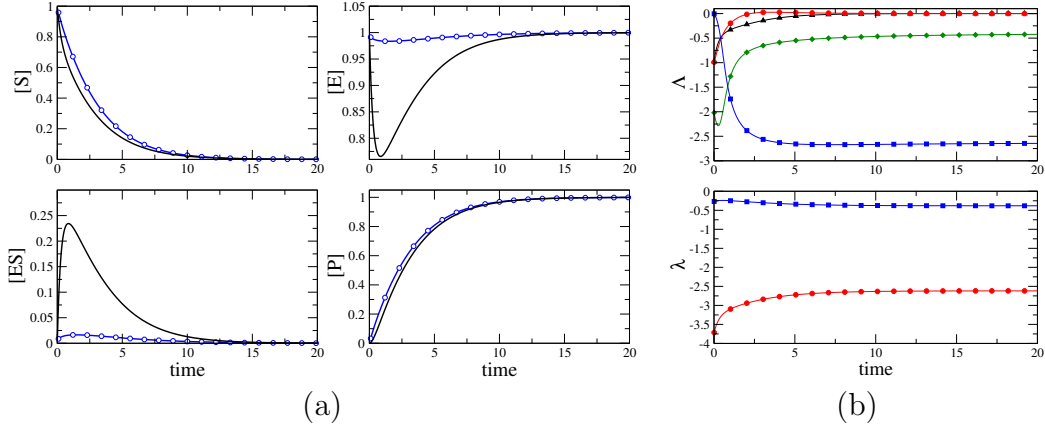
Figure 3.2: The sample semiorbit for $k_{1f} = k_{1r} = k_{cat} = 1.0$ and $k_{r2} = 10^{-5}$. (a) Comparison between the profiles of concentration of species deduced from the detailed (solid lines) and the reduced SQEM description (symbols); (b) evolution of the Lyapunov exponents and the eigenvalues of the system;

For the $k_{1f} = k_{1r} = k_{cat} = 1.0$ and $k_{r2} = 10^{-5}$ case, the constraint (slowest left eigenvector at equilibrium) is $[\boldsymbol{B}^d] = [0.8507, 0, 0.5257, 0]$ and as shown in Fig. 3.2(a) there is a good agreement between detailed and reduced systems for the time evolution of the substrate and product. Far away from equilibrium, the SQEM strongly under- or over-predicts the concentrations of [E] and [ES].

As mentioned before, the idea behind the quasi-equilibrium approximation is valid in the case of clear separation between slow and fast motions. It can be seen from Fig. 3.2(b) that the gap between the eigenvalues at equilibrium, $\lambda_f/\lambda_s \simeq (-2.618)/(-0.382) = 6.85$ is less than one order of magnitude.

In phase space (Fig. 3.1(a)), the selected trajectory meets the one-dimensional manifold at around $t = 2.0$. However, from the temporal evolution of the Lyapunov exponents, Fig. 3.2(b), the contraction rate of volumes in the whole phase space becoming constant after $t = 5.0$, implying attraction to the one-dimensional manifold for $t \geq 5.0$. The relatively small gaps between the Lyapunov exponents indicate that there is no dominant shrinkage rate of the phase space and the one-dimensional description is not a good assumption for $t \leq 5$.

The gap between slow and fast processes increases with decreasing ratio $\frac{k_{cat}}{k_{r1}}$, leading to better approximation of the detailed kinetics by the SQEM reduced model. For $\frac{k_{cat}}{k_{r1}} = 0.1$ and $\frac{k_{cat}}{k_{r1}} = 0.01$ the results are shown in Fig. 3.3 and Fig. 3.4, respectively.

In Fig. 3.3 the spectral gap at equilibrium and slow constraint are
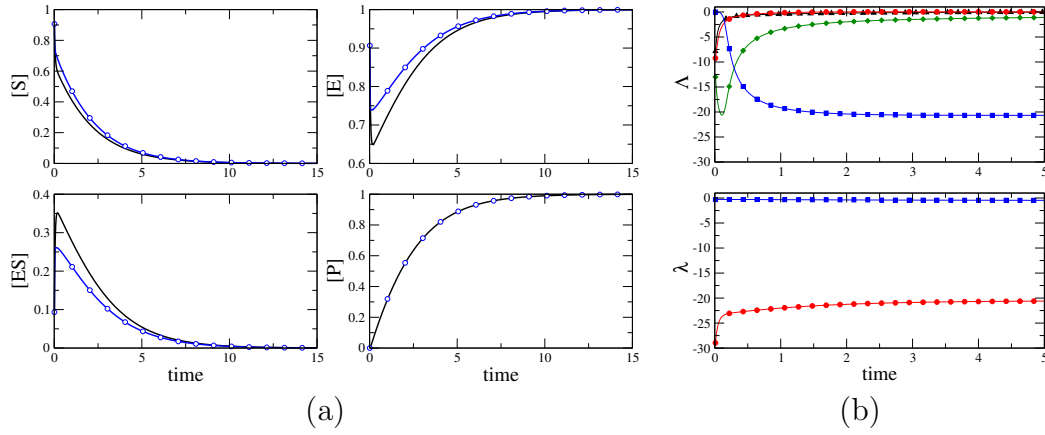
Figure 3.3: The sample semiorbit for $k_{1f} = k_{1r} = 10$, $k_{cat} = 1.0$ and $k_{r2} = 10^{-5}$. (a) Comparison between the profiles of concentration of species deduced from the detailed (solid lines) and the reduced SQEM description (symbols); (b) evolution of the Lyapunov exponents and the eigenvalues of the system;
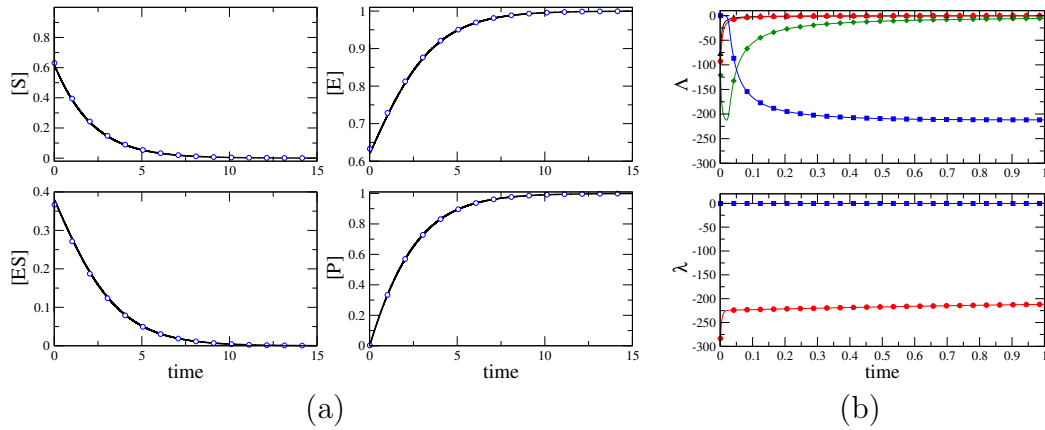
Figure 3.4: The sample semiorbit for $k_{1f} = k_{1r} = 100$, $k_{cat} = 1.0$ and $k_{r2} = 10^{-5}$. (a) Comparison between the profiles of concentration of species deduced from the detailed (solid lines) and the reduced SQEM description (symbols); (b) evolution of the Lyapunov exponents and the eigenvalues of the system;

$\lambda_f/\lambda_s \simeq 42.0762$ and $[\boldsymbol{B}^d] = [0.7246, 0, 0.6892, 0]$. The evolution obtained with the reduced description for the [E] and [ES] concentrations is in better agreement with the detailed evolution with respect to the $\frac{k_{cat}}{k_{r1}} = 1$ case, and

the SQEM trajectory approaches the detailed one much earlier. For $\frac{k_{\text{cat}}}{k_{r1}} =$ 0.01 (Fig. 3.4), the agreement between the detailed and reduced model for all species is excellent. The constraint is $[\boldsymbol{B}^d] = [0.7089, 0, 0.7053, 0]$ and the spectral gap at equilibrium is more than two orders of magnitude, $\lambda_f/\lambda_s \simeq 401.96$, implying the clear separation of timescales.

3.3   Results: Autoignition of homogeneous mixtures

In the following section the application of SQEM reduced model is demonstrated for the detailed combustion mechanisms of hydrogen, syngas and methane corresponding to 6-, 8- and 27-dimensional systems. Thermodynamic properties and reaction rates were evaluated using CHEMKIN [104] and the convex minimization problem (2.22) is solved using the CEQ code [81].

3.3.1   H$_2$/air mixture

The detailed kinetics scheme of hydrogen/air mixture includes $n_s = 9$ species and $n_r = 21$ reactions [17]. In the scope of RCCE applications for hydrogen combustion, the total number of moles (TM), the total number of radicals referred to active valence (AV), and free oxygen (FO) are linear constraints proposed in [67, 70] as an appropriate set of constraints in the scope of RCCE applications for hydrogen combustion (Table 2.1).

The evolution of temperature for a stoichiometric hydrogen/air mixture

at atmospheric pressure with initial temperature $T_0 = 1200$ K is plotted in Fig. 3.5. The detailed (solid line) solution is compared with SQEM (lines with symbols) and RCCE manifold (dashed, dotted and dot-dashed lines). It can be seen that with increasing dimension (number of constraints) the agreement between the reduced and detailed description improves, and that for the same dimension the SQEM provides a more accurate description.
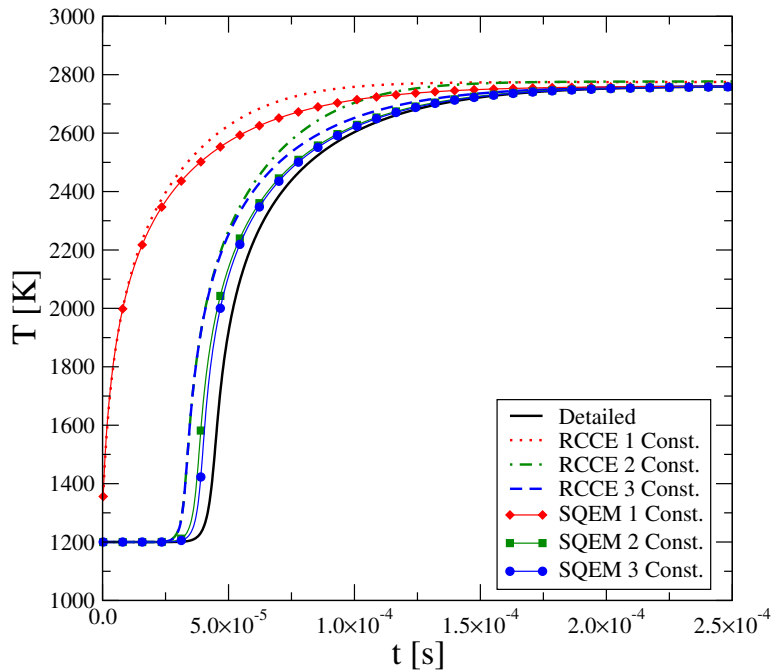
Figure 3.5: The temperature evolution for stoichiometric H_2/air auto-ignition under atmospheric pressure with unburnt temperature $T_0 = 1200$ K. Detailed solution is compared with RCCE and SQEM reduced models with different number of constraints.

For finding a better approximation of the ignition delay time, the initial composition of the constrained equilibrium state should approximate the actual initial composition [70]. Fig. 3.5 shows that the initial state is

not located near the one-dimensional quasi-equilibrium manifold which is constructed based on one constraint in RCCE (1 Const., TM) and SQEM (slowest left eigenvector at equilibrium).

The temporal evolution of species mass fractions using the three-dimensional reduced QEM models are plotted in Fig. 3.6. SQEM provides a more accurate description even for the low concentration species (hydroperoxy radical HO_2 and hydrogen peroxide H_2O_2).
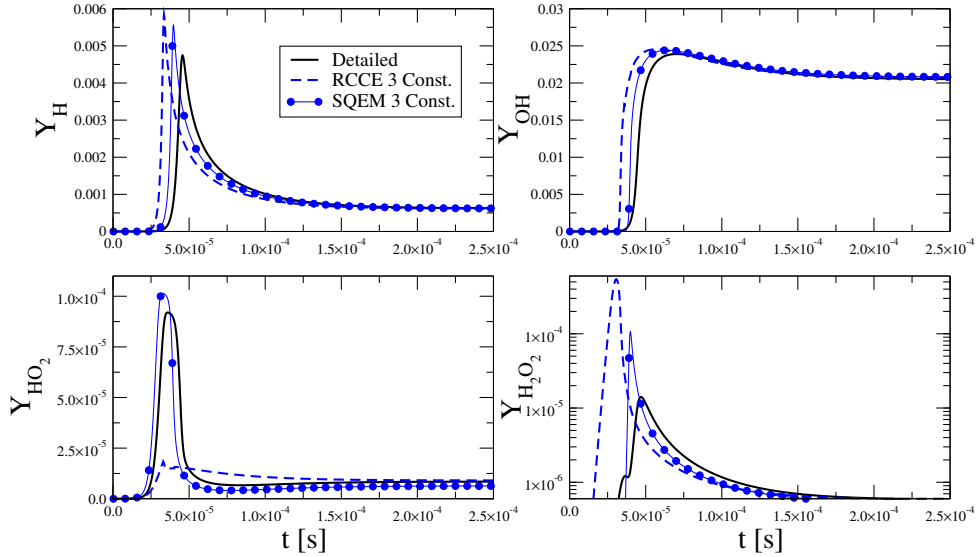
Figure 3.6: Time history of selected species mass fractions for stoichiometric H_2/air auto-ignition under atmospheric pressure with unburnt temperature $T_0 =$1200 K. Detailed solution is compared with three-dimensional RCCE and SQEM reduced models.

3.3.2 Syngas/air mixture

The $CO/H_2/O_2$ elementary scheme of Li et al. [17] was used for the chemistry description with 32 non-duplicate elementary reversible reactions and

12 chemical species. For a stoichiometric mixture of syngas/air in an adiabatic constant pressure reactor with $T_0 = 1200$ K, the temperature evolution captured from the detailed kinetics is compared with those found by SQEM reduced descriptions of different dimension. It is shown that for two $CO:H_2$ molar ratios $r_{CO/H_2} = 1/3$ and 3 (Fig. 3.7 (a) and (b)) the agreement of the SQEM with three constraints and the detailed mechanism for the ignition delay time and the temperature time history is excellent.
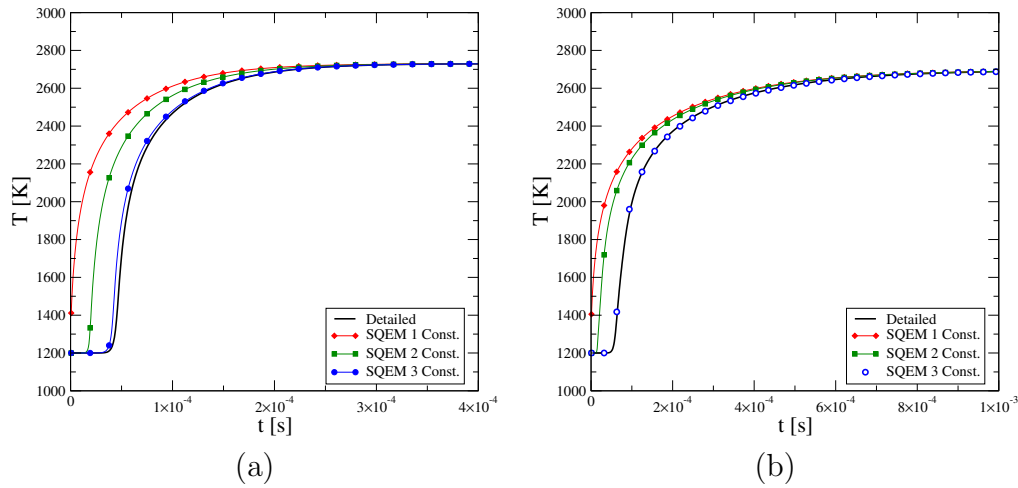
Figure 3.7: The temperature evolution for stoichiometric syngas/air autoignition under atmospheric pressure with unburnt temperature $T_0 =$1200 K. Detailed solution is compared with SQEM reduced models with different constraints for (a) $r_{CO/H_2} = 1/3$ and (b) $r_{CO/H_2} = 3$.

3.3.3 Methane/air mixture

The GRI 1.2 mechanism [105] is used to predict the oxidation rates of CH_4. The detailed mechanism includes 31 species and 175 elementary reactions with four elemental conservations (H, O, C and N); hence, the system is 27-dimensional. The temperature evolution for the stoichiometric mixture

with $T_0 = 1400$ K, $p = 1$ atm is plotted in Fig. 3.8 shows that SQEM with seven constraints can capture the temperature behavior perfectly meaning that the 27-dimensional system in this case can be represented with 7-dimensional reduced order model.
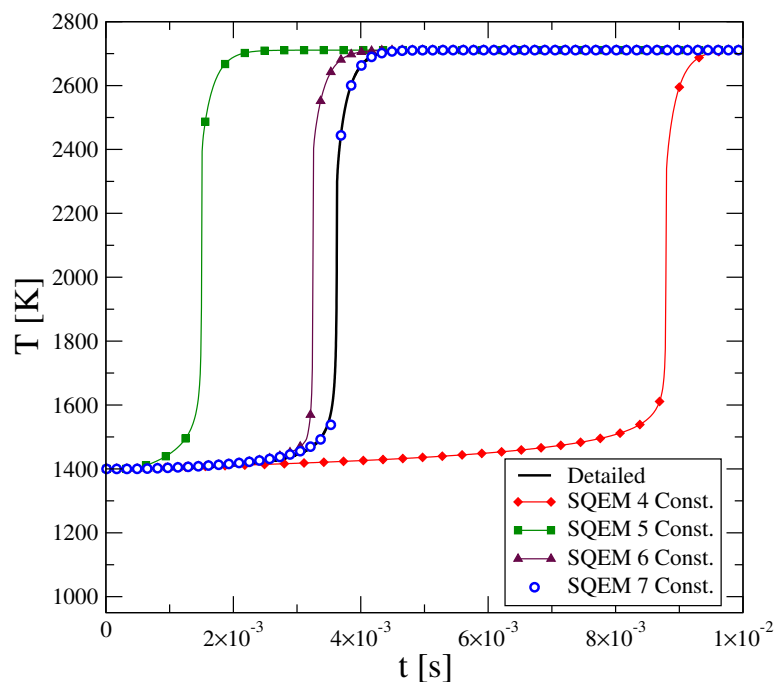
Figure 3.8: The temperature evolution for stoichiometric methane/air auto-ignition under atmospheric pressure with unburnt temperature $T_0 =1400$ K. Detailed solution is compared with SQEM reduced models with different constraints.

It should be pointed out that the discrepancy between the reduced and the detailed descriptions reduces non-monotonically with the dimension of the SQEM model. Similar observations were made in other classes of chemical kinetics model reduction methods based on species elimination techniques [106, 107].

Profiles of selected species found by SQEM six- and seven-dimensional reduced manifolds are compared with the detailed model in Fig. 3.9, exhibiting good agreements for the reduced model with seven constraints.
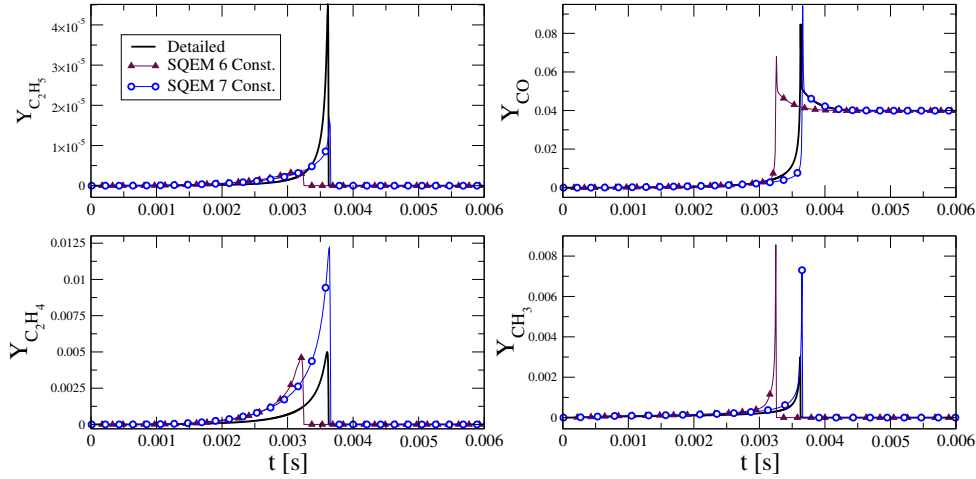
Figure 3.9: Time history of selected species mass fractions for stoichiometric methane/air auto-ignition under atmospheric pressure with unburnt temperature $T_0 = 1400$ K. Detailed solution is compared with SQEM reduced models with different constraints.

3.4 Conclusion

The spectral quasi-equilibrium manifolds based on the slow left eigenvectors at equilibrium can be used to obtain accurate reduced descriptions for combustion kinetics. The construction of the quasi-equilibrium states is based on the concave optimization of an entropy function under the constraints defined by the left eigenvectors on the number of moles of species. These states belong to the Spectral Quasi Equilibrium Manifold (SQEM), which shows better approximation of reduced model in comparison to RCCE-

manifold routinely used in the combustion community. SQEM offers a general mathematically-based procedure to define the constraints imposed on the species and it is automated for any comprehensive/skeletal mechanisms. The autoignition of hydrogen, syngas and methane shows very good agreement between the time history of the temperature and radicals deduced from reduced and detailed models.

Although the results of SQEM is promising by itself, it can be used for construction of slow invariant manifolds in the class of approaches in which an initial grid is iteratively relaxed towards SIM, such as Method of Invariant Grid [92, 93] and the algorithm proposed in Ref. [16].

Chapter 4

Entropy production analysis for

mechanism reduction [1]

4.1 Introduction

In this chapter we will present the method developed during our study categorized under skeletal reduction techniques.

Briefly, skeletal mechanisms can be generated by eliminating reactions and/or species [108, 109]. Elimination of unimportant reactions can be performed using, for example, sensitivity analysis [21], the importance index of CSP [110], Principal Component Analysis (PCA) [22] or optimization-based methods [12, 111]. Due to their nonlinear coupling, the direct elimination of species is more challenging. CSP [33,110,112–114], Directed Relation Graph (DRG) [27, 115–118], DRG with Error Propagation (DRGEP) [119, 120], DRG-Aided Sensitivity Analysis (DRGASA) [121, 122], Transport Flux-

---

[1]The content of the present chapter is published in Kooshkbaghi, M., Frouzakis, C. E., Boulouchos, K., & Karlin, I. V. (2014). Entropy production analysis for mechanism reduction. *Combustion and Flame, 161(6)*, 1507-1515.

Based DRG (TFBDRG) [123], Path Flux Analysis (PFA) [24,28] and necessity analysis [30] have been employed for species elimination. Species with similar thermal and transport properties and diffusivities can be lumped together to further reduce the size of the skeletal mechanism [124–126]. Selecting important species during the simulation (on the fly model reduction) is also possible as proposed for example by the Dynamic Adaptive Chemistry (DAC) reduction method [127,128]. The aforementioned methods can be combined with storage/retrieval approaches [129]. A more comprehensive discussion is available in chapter 1 and the references therein.

For large mechanisms, approaches which select species based on the slow/fast decomposition bear heavy computational cost because of the timescale analysis of the Jacobian matrix of the associated large system of ODEs. On the other hand, QSSA, PEA and sensitivity analysis require additionally mechanism-dependent knowledge. The methods which are based on the graph structure relation between species, sometimes need a careful a priori choice of the group of target species [127].

In the present study, the relative contribution of elementary reactions in the total entropy production is proposed as a criterion for the construction of accurate skeletal reaction mechanisms. The important reactions are identified based on their relative contribution to the total entropy production being larger than a user-specified threshold. Entropy production is the well known scalar function for reactive systems with some natural properties such as positivity. This criterion leads to a procedure that is easy to implement without any prior knowledge about the detailed mechanism. Skeletal

mechanisms of different sizes can be obtained by choosing the threshold based on the desired deviation from the result of the detailed mechanism.

A significant reduction in the number of species as well as the stiffness of the system is reported here for the case of a detailed scheme for n-heptane. The skeletal mechanisms are shown to provide very accurate results at a fraction of the computational cost in comparison to the detailed mechanism for various cases over a wide range of thermodynamic conditions. Compared to the other methods such as Directed Relation Graph (DRG) and Computational Singular Perturbation (CSP) [114, 116], the same level of reduction can be achieved with the much simpler entropy production analysis.

The chapter is organized as follows. In Sec. 4.2, the basic notion of the entropy production for chemical kinetics is briefly reviewed. The features and algorithm of the method for skeletal mechanism reduction are presented in Sec. 4.3. In Sec. 4.4, the algorithm is applied on a database generated using a detailed n-heptane mechanism and two skeletal mechanisms are compared. In the remaining part of Sec. 4.4 the ignition delay calculation, homogeneous engine model, perfectly stirred reactor and laminar premixed flame are used for the validation of the skeletal mechanism. Conclusions are drawn in Sec. 4.5. Instructions on the numerical procedure of the entropy production analysis are presented in the appendix A.

4.2 Entropy production for chemical kinetics

For the sake of completeness, the notion of the entropy production is briefly reviewed in this section following the formalism of [130]. For a detailed discussion of the entropy and entropy production concepts for chemical kinetics and other systems the reader is also referred to [59,71]. The changes in the entropy for a system at local equilibrium is expressed as

$$dS = d^{ex}S + d^{in}S \tag{4.1}$$

where superscripts 'in' and 'ex' denote the change of the system entropy due to interactions inside the domain and with its environment [130]. The change of the i-th species in the k-th reaction is related to the change in the extent of each reaction, ζ_k, as

$$\frac{dN_i}{\nu''_{ik} - \nu'_{ik}} = d\zeta_k, \quad i = 1, \cdots, n_s \quad k = 1, \cdots, n_r \tag{4.2}$$

where the extent of reaction is related to the reaction rate by

$$\frac{d\zeta_k}{dt} = V(q_{f_k} - q_{r_k}) \tag{4.3}$$

The fundamental equation of chemical thermodynamics in terms of the internal energy reads

$$dU = TdS - pdV + \sum_{i=1}^{n_s} \mu_i dN_i \tag{4.4}$$

where μ_i is the chemical potential of the i-th species

$$\mu_i = \left(\frac{\partial U}{\partial N_i}\right)_{S,V,N_{l\neq i}}, \quad i = 1, \cdots, n_s \tag{4.5}$$

The de Donder affinity [131] of reaction k is defined as

$$\alpha_k = -\Sigma_{i=1}^{n_s}(\nu_{ik}'' - \nu_{ik}')\mu_i, \quad k = 1, \cdots, n_r \tag{4.6}$$

In the absence of deviations from the principle of detailed balance [71], α_k may be expressed as

$$\alpha_k = R_c T \ln\left(\frac{q_{f_k}}{q_{r_k}}\right) \tag{4.7}$$

The change in the number of moles of each species can be decomposed into the change due to chemical reactions, $d^{in}N_i$, and exchange of matter with the system exterior, $d^{ex}N_i$ [132].

$$dN_i = d^{in}N_i + d^{ex}N_i, \quad i = 1, \cdots, n_s \tag{4.8}$$

For open systems, the entropy exchange with the exterior is of the form

$$d^{ex}S = \frac{dU + pdV}{T} - \frac{\sum_{i=1}^{n_s}\mu_i d^{ex}N_i}{T} \tag{4.9}$$

while the entropy change due to the change in mole numbers with respect to chemical reactions reads

$$d^{in}S = -\frac{\sum_{i=1}^{n_s}\mu_i d^{in}N_i}{T} \tag{4.10}$$

For a closed system, $d^{ex}N = 0$ so that $dN = d^{in}N$ and the entropy production due to a chemical reaction is,

$$\frac{d^{in}S}{dt} = -\frac{1}{T}\sum_{i=1}^{n_s}\mu_i\frac{dN_i}{dt} \tag{4.11}$$

where $\frac{dN_i}{dt}$ can be written in terms of the extent of reactions using (4.2)

$$\frac{dN_i}{dt} = \sum_{k=1}^{n_r}(\nu''_{ik} - \nu'_{ik})\frac{d\zeta_k}{dt} \tag{4.12}$$

Hence, entropy production is

$$\frac{d^{in}S}{dt} = -\frac{1}{T}\sum_{i=1}^{n_s}\mu_i\sum_{k=1}^{n_r}\frac{d\zeta_k}{dt}(\nu''_{ik} - \nu'_{ik}) \tag{4.13}$$

or by the affinity definition (4.6),

$$\frac{d^{in}S}{dt} = \frac{1}{T}\sum_{k=1}^{n_r}\alpha_k\frac{d\zeta_k}{dt} \tag{4.14}$$

Using (4.3) and (4.7), the total entropy production per unit volume becomes

$$\frac{d^{in}S}{dt} = R_c\sum_{k=1}^{n_r}(q_{f_k} - q_{r_k})\ln\left(\frac{q_{f_k}}{q_{r_k}}\right) \geq 0 \tag{4.15}$$

The entropy production (4.15) is a positive semi-definite function which vanishes at equilibrium. The relative contribution of each reaction to the total entropy production at time t, $r_k(t)$ is finally defined as

$$r_k(t) = \left(\frac{d^{in}S}{dt}\right)^{-1}\left[R_c(q_{f_k} - q_{r_k})\ln\left(\frac{q_{f_k}}{q_{r_k}}\right)\right] \tag{4.16}$$

From equation (4.16) it is clear that for the reactions at equilibrium $r_k(t) = 0$.

4.3 Skeletal reduction using entropy production analysis

In this chapter, the relative contribution of each reaction to the total entropy production is considered as a measure of its importance. The steps for finding the subset of the reactions that at the time t of interest forms the skeletal mechanism are summarized below:

1. Identify the *most-contributing reactions*, i.e. the reactions which contribute at least ε to the total entropy production

$$r_k(t) \geq \varepsilon \tag{4.17}$$

2. Identify the *important species*, i.e. the species participating in the most-contributing reactions.

3. Generate the skeletal mechanism. The simplified mechanism at time t is generated by eliminating the non-important species from the detailed description using a slightly modified version of MECHMOD 3.42 [133].

Note that each important species participate in *at least one* most-contributing reaction. Following step 3, the skeletal mechanism contains not only the most contributing reactions, but all elementary reactions which

include important species on both sides as well. Further reduction of the number of reactions (with the same amount of species) would necessities further analysis such as reaction path or atomic flux [24] to quantify the contribution of each reaction in the total production or consumption rate of each species.

The local analysis of the entropy production can be applied at different time instants during the temporal evolution of the system state. The analysis can be extended to a database of trajectories computed for a range of pressures, initial temperatures and compositions to construct a global skeletal mechanism. The most-contributing reactions are considered as the reactions which at least once have a significant contribution in the entropy production of the whole database. The final skeletal mechanism is valid within the range of conditions represented by the sample data. The algorithm of the present simple procedure is provided in the appendix A using CHEMKIN's notation.

Finally, it should be pointed out that the term q_{f_k}/q_{r_k} in the logarithm of (4.15) must be strictly positive. This condition is violated in two cases:

(a) irreversible reactions where the backward reaction rate is zero ($q_{r_k} = 0$);

(b) when low negative concentrations result from numerical issues ($q_{f_k} < 0$ and/or $q_{r_k} < 0$).

In case (a) the q_{r_k}, and in the case (b) q_{f_k} and/or q_{r_k} should be set to be a small (chemically insignificant) positive number (e.g. 10^{-50} in our study). The problem of partially irreversible limit in chemical thermodynamics is

addressed in the recent study [134].

4.4   Skeletal mechanism for n-heptane

The kinetics of n-heptane is of interest not only in its own right as representative of the kinetics of higher hydrocarbons displaying the Negative Temperature Coefficient (NTC) regime and multistage ignition, but also as one of the components of the Primary Reference Fuel (PRF) used for octane rating of internal combustion engines [135]. The comprehensive mechanism for n-heptane consisting of 561 species and 2539 reactions (LLNL mechanism version 2, [136]) was developed to study oxidation for pressures in the range $1 \leq p \leq 42$ atm, initial temperatures between 550 to 1700 K, equivalence ratio φ from 0.3 to 1.5, and nitrogen-argon dilution from 70 to 99 percent [4]. The detailed mechanism which will be referred to as D561 below has been used for the development of reduced schemes by various approaches [114, 116, 117, 126, 137].

The local entropy production analysis is performed at the four time instants during the isobaric and isenthalpic auto-ignition of a stoichiometric mixture at initial temperature and pressure $T_0 = 650$ K, $p = 1$ atm marked in Fig. 4.1 to identify the reactions contributing at least $\varepsilon = 0.05$ to the total entropy production. The analysis reveals that initially ($t = 0$ s) the important reactions are the initiation reaction of oxygen attacking the fuel
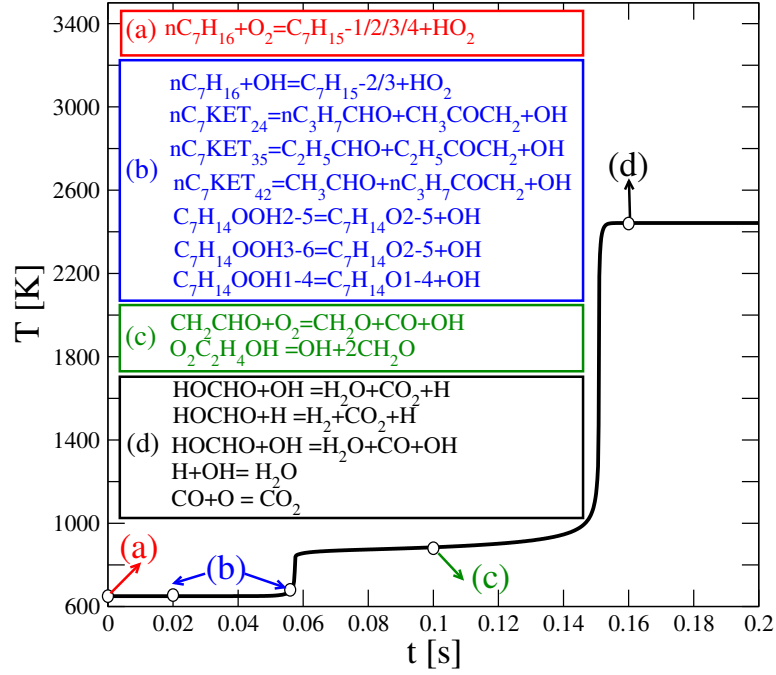
Figure 4.1: Time history of temperature computed using the detailed mechanism and the major elementary reactions during different stages ($T_0 = 650\,K$, $p = 1\,atm$ and $\varphi = 1$).

to produce HO_2 and the heptyl radical isomers

$$n C_7 H_{16} + O_2 \rightleftharpoons C_7 H_{15}{-}3 + HO_2$$

$$n C_7 H_{16} + O_2 \rightleftharpoons C_7 H_{15}{-}2 + HO_2$$

$$n C_7 H_{16} + O_2 \rightleftharpoons C_7 H_{15}{-}4 + HO_2$$

$$n C_7 H_{16} + O_2 \rightleftharpoons C_7 H_{15}{-}1 + HO_2$$
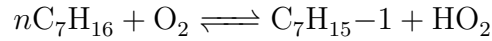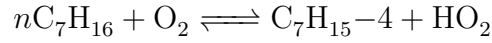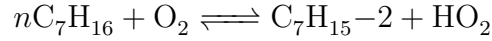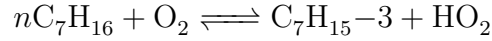
During the first pre-ignition period ($t = 0.02$ and 0.056 s), reactions with

OH radicals abstracting H from the fuel

$$nC_7H_{16} + OH \rightleftharpoons C_7H_{15}-2 + H_2O$$

$$nC_7H_{16} + OH \rightleftharpoons C_7H_{15}-3 + H_2O$$

thermal decomposition

$$C_7H_{14}OOH_2-5 \rightleftharpoons C_7H_{14}O2-5 + OH$$

$$C_7H_{14}OOH_3-6 \rightleftharpoons C_7H_{14}O2-5 + OH$$

$$C_7H_{14}OOH_1-4 \rightleftharpoons C_7H_{14}O1-4 + OH$$
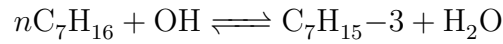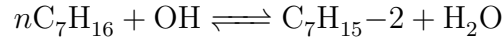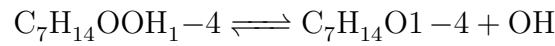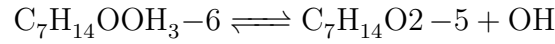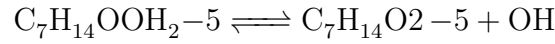
and ketohydroperoxides decomposition

$$nC_7ket_{24} \longrightarrow nC_3H_7CHO + CH_3COCH_2 + OH$$

$$nC_7ket_{35} \longrightarrow C_2H_5CHO + C_2H_5COCH_2 + OH$$

contribute significantly to the entropy production. The most-contributing reactions during the period before the second ignition ($t = 0.1$ s) are the ones producing formaldehyde (CH_2O) and carbon monoxide (CO)

$$CH_2CHO + O_2 \longrightarrow CH_2O + CO + OH$$

$$O_2C_2H_4OH \longrightarrow OH + 2\,CH_2O$$
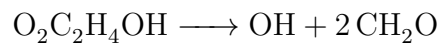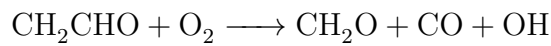
The analysis of post-ignition at $t = 0.16$ s shows that the most-contributing

reactions are those producing the main products (CO_2, CO and H_2O)

$$HOCHO + OH \longrightarrow H_2O + CO_2 + H$$

$$HOCHO + H \longrightarrow H_2 + CO_2 + H$$

$$HOCHO + OH \longrightarrow H_2O + CO + OH$$
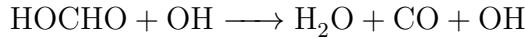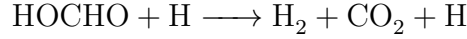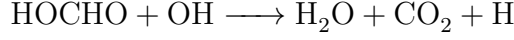
The distribution of entropy production among reactions for different times are summarized in Fig. 4.2. It is worth to pointing out that the important
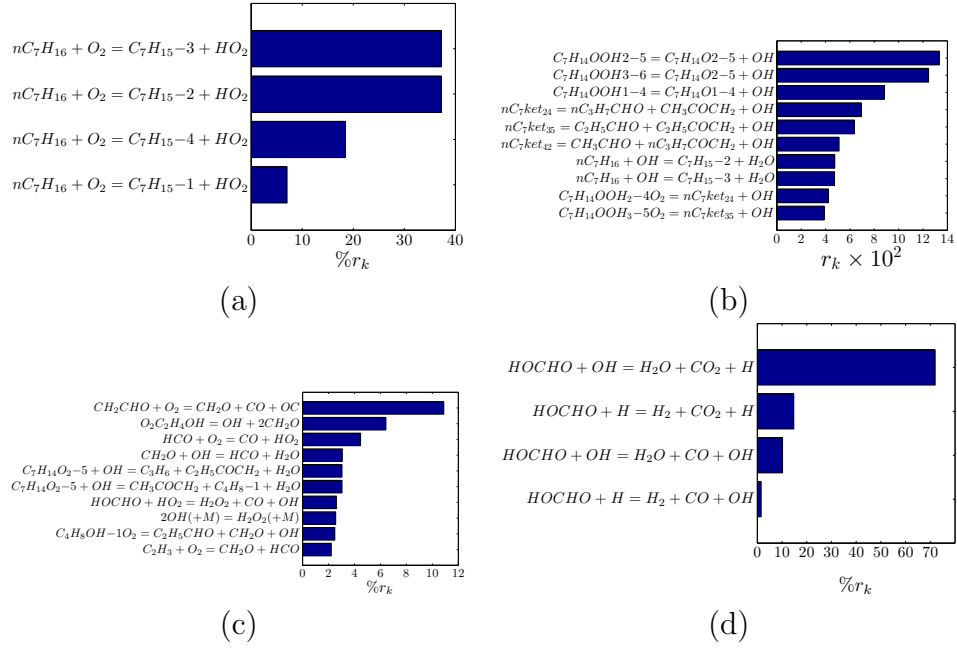
Figure 4.2: Entropy production distributions among reactions using the detailed mechanism ($T_0 = 650K$, $p = 1$ atm and $\varphi = 1$); (a) $t = 0$ s, (b) $t = 0.03$ s, (c) $t = 0.1$ s, (d) $t = 0.16$ s.

reactions, products and oxidation path found here on the basis of the entropy production analysis are in agreement with the results of the kinetic description of n-heptane oxidation [4] and the CSP analysis [114].

Entropy production analysis was then performed on a solution database for auto-ignition in the range of pressures 1, 5, 10, 20 atm, initial temperatures in the range $650 \leq T_0 \leq 1400$ K resolved with a step of 50 K, equivalence ratios $\varphi =$ 0.5, 0.8, 1.0, 1.2, 1.5 and different threshold values ε. The dependence of the error in the ignition delay time and the number of species in the skeletal mechanism on the value of ε are plotted in Fig. 4.3 for $p = 1$ atm, $T_0 = 650$ K and $\varphi = 1.0$. The non-monotonicity of the error curve has also been observed in other species elimination techniques based on analysis of reactive states [28, 106].
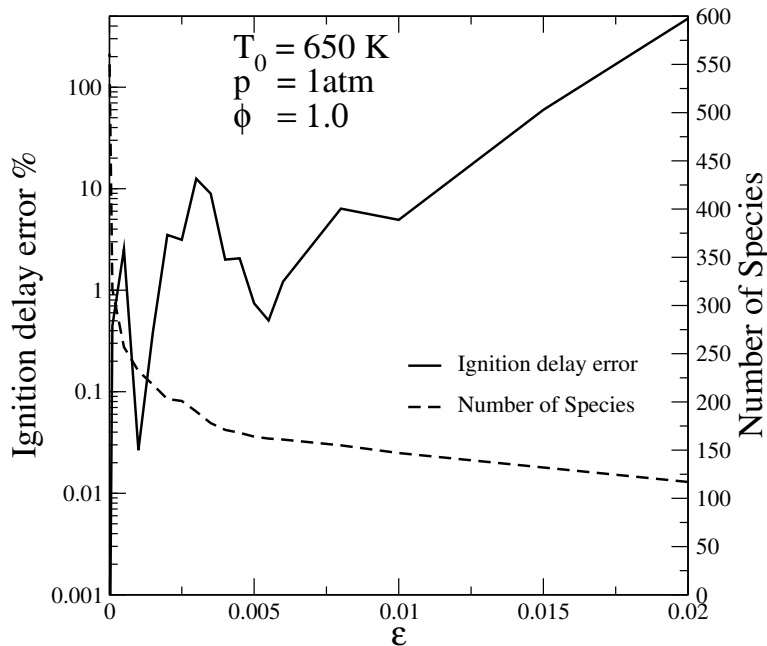
Figure 4.3: Number of species in the skeletal mechanism and relative error in the ignition delay time as a function of the threshold.

Two skeletal mechanisms with 161 species in 688 reactions and 203 species in 879 reactions obtained with $\varepsilon = 0.006$ and 0.002 and henceforth

referred to as R161 and R203, respectively, were selected for validation. It should be noted that smaller schemes can be readily constructed, albeit at the cost of narrower range of applicability and/or lower accuracy. Similar species can also be lumped together as proposed in [117, 126] to further reduce the size of the mechanism.

The size of the mechanism obtained by the entropy production analysis is comparable with other reducing strategies. With the same quality of reduction, skeletal mechanisms including 188 species and 842 reactions was obtained by DRG [116], and 177 species and 768 reactions or 185 species and 786 reactions by CSP [114].

4.4.1   Auto-ignition of homogeneous mixtures

Ignition delay times in the constant pressure and enthalpy reactor computed using the skeletal and detailed mechanisms are compared in Fig. 4.4. Both skeletal mechanisms reproduce the ignition delay well over a wide range of pressures, equivalence ratios and temperatures including the NTC region. As expected, better agreement is obtained at high pressures and temperatures and the error for R161 is higher than that of R203.

Species elimination with the help of entropy production leads not only to an ODE system of reduced dimensionality but also with lower stiffness. The evolution of the fastest timescale, τ_{fast}, defined by the inverse of the most negative eigenvalue of the Jacobian matrix for the D561, R203 and R161 schemes is plotted in Fig. 4.5, together with the time history of temperature. The fast timescale is monotonically decreasing towards equilibrium,
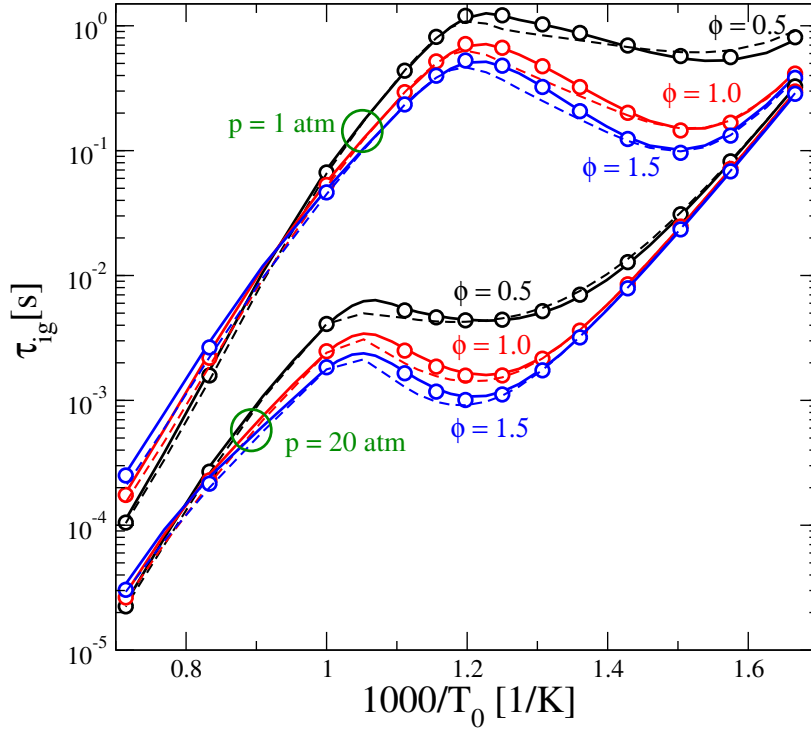
Figure 4.4: Ignition delay times computed with the different mechanisms (D561: solid line, R203: circles, R161: dashed line).

while there are sharp drops during the two ignition stages. The difference between the timescales of the detailed and skeletal mechanisms are several orders of magnitude which in combination with the reduced number of variables results in a significant reduction in computational time even for homogeneous autoignition computations. CPU times for the calculation of 1 s of the ignition process for three initial temperature are summarized in Table 4.1 using the stiff integrator DVODE [84]. The CPU calculation times reveals that the speed up for R203 and R161 compared with D561 is around 10.3 and 16, respectively. Similar order of timescales for n-heptane was also reported in [137]. It should be noted that the unrealistically fast time scales of the order of 10^{-15} s may well be an artifact of the way the detailed mech-
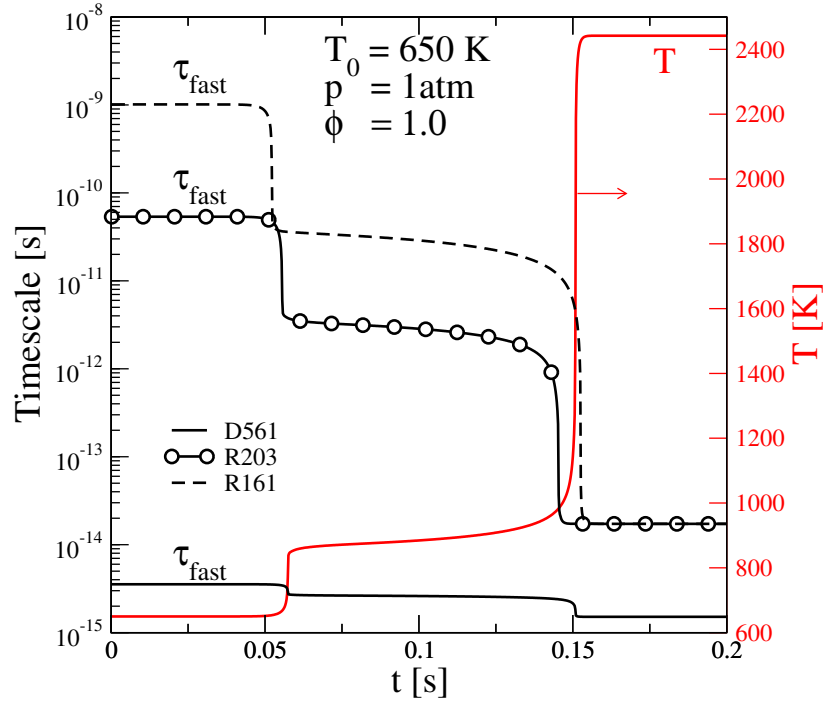
Figure 4.5: Temporal evolution of the temperature and the fastest timescale of the homogeneous autoigintion system for the skeletal (R203: circles with solid line, R161: dashed line) and detailed mechanism (solid line).

Table 4.1: CPU times (seconds) for the integration of the isobaric and isenthalpic reactor till 1 second ($\varphi = 1, p = 1$ atm).

	$T_0 = 600$ K	$T_0 = 650$ K	$T_0 = 700$ K	$T_0 = 750$ K
D561	111.865	97.322	98.672	88.494
R203	10.796	10.043	9.068	8.483
R161	6.618	6.499	5.958	5.684

anisms for such complex fuels are generated (automatic generation based on the so-called reaction classes [4]).

The corresponding curves of the total entropy production per volume are compared in Fig. 4.6. The peaks in the entropy production correspond to the ignition stages; the entropy production history of the detailed solu-

tion is well reproduced by both R203 and R161. At equilibrium the entropy reaches its maximum and dS/dt tends to zero (Fig. 4.6) albeit at a decreasing rate (Eq. 4.15). In the presence of irreversible reactions and negative
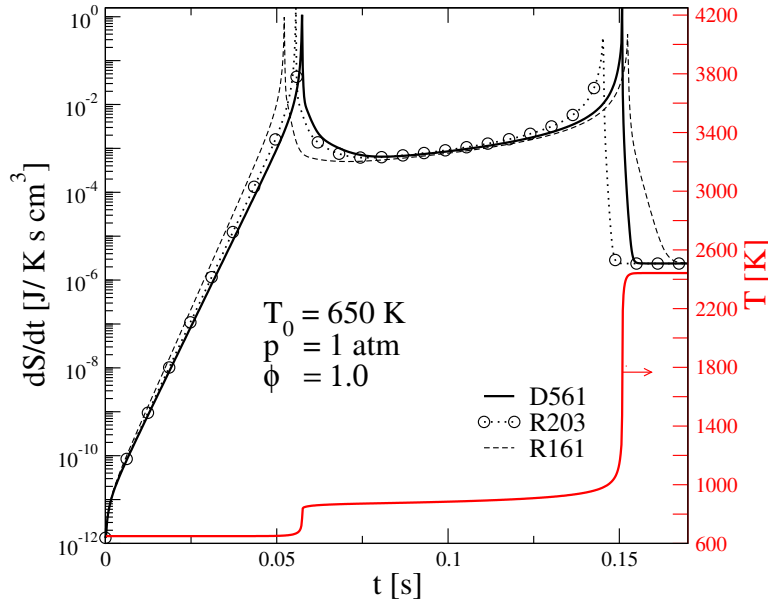
Figure 4.6: Time history of the entropy production (D561: solid line, R203: circles, R161: dashed line).

concentration resulting from numerical issues (as is the case here), the value of dS/dt at long times is affected by the value chosen for the regularization of zero (or negative) reaction rates (see section 4.3).

4.4.2 Single-zone engine model

In the absence of spatial inhomogeneities, a single-zone model can be used to simulate a reciprocating engine with adiabatic boundary conditions [138]. The governing equations for the temporal evolution of the species mass
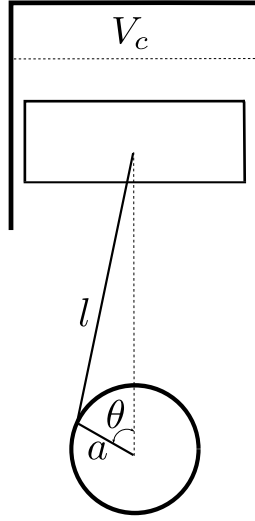
Figure 4.7: Schematic picture of single-zone engine model with dimensions.

fractions, Y_i, temperature and pressure read

$$
\begin{aligned}
\frac{dY_i}{dt} &= \frac{\dot{\omega}_i W_i}{\rho} \\
\frac{dT}{dt} &= \frac{1}{c_v}\left(-p\frac{d(1/\rho)}{dt} - \frac{\sum_i e_i \dot{\omega}_i W_i)}{\rho}\right) \\
p &= \frac{R_c T \rho}{\overline{W}}
\end{aligned}
\tag{4.18}
$$

where, ρ, $\overline{W}$ and c_v are the density, mean molecular weight and mean specific heat at constant volume of the mixture, and R_c the ideal gas constant. Thermodynamic properties, production rates, $\dot{\omega}_i$, and specific internal energy, e_i, of the ith species are computed, using the CHEMKIN library [104]. The change of density in time is the function of the cylinder volume and the total mass of the reacting mixture. The change of volume, $V(t)$, can be

related to the crank angle, θ [138]

$$\frac{V(t)}{V_c} = 1 + \frac{1}{2}(r_c - 1)f(\theta) \qquad (4.19)$$

with

$$f(\theta) = l/a + 1 - cos(\theta(t)) - \sqrt{(l/a)^2 - sin(\theta(t))} \qquad (4.20)$$

where, V_c is the clearance volume (minimum cylinder volume), l/a is the
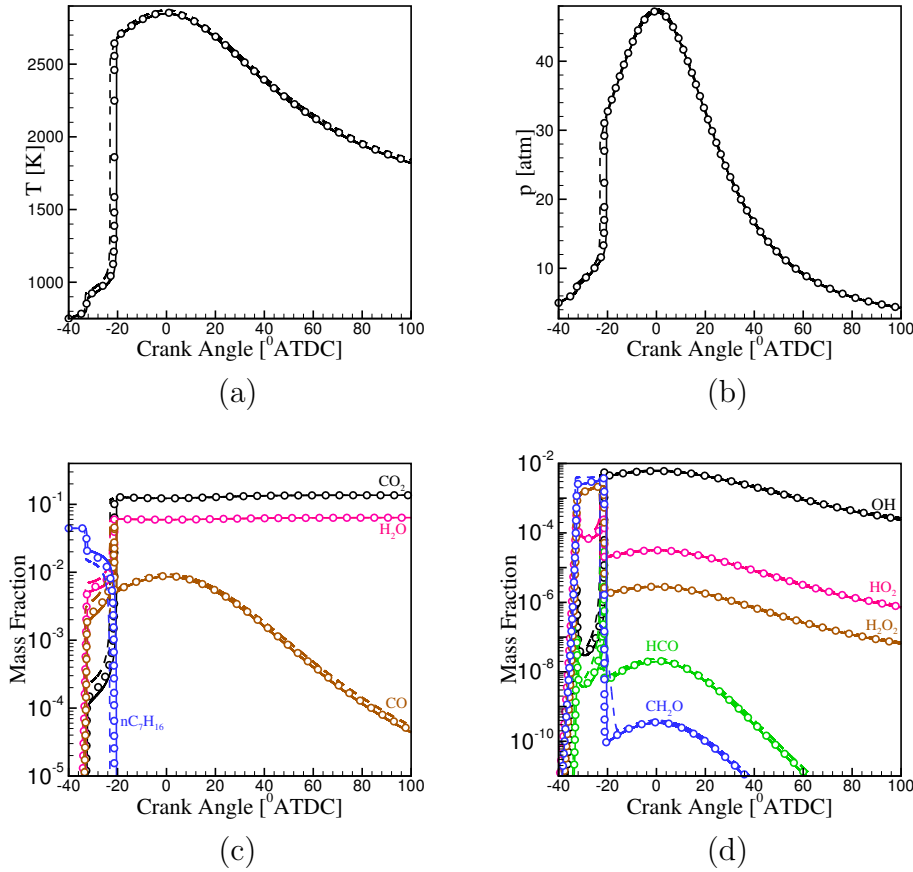
Figure 4.8: Temperature (a), pressure (b) and selected species concentration (c,d) profiles for the single-zone engine model. The lean fresh mixture ($\varphi = 0.8$) is injected at -40 ^{0}ATDC with $p_0 = 5$ atm and $T_0 = 750$ K (D561: solid line, R203: circles, R161: dashed line).

ratio of the connecting rod length to the crank radius and r_c is the compression ratio (see Fig. 4.7). The simulation are carried out for an engine with $V_c = 125$ ml, $l/a = 3$ and $r_c = 10$. The initial temperature and pressure for the lean mixture ($\varphi = 0.8$) at $-40\,^\circ\text{ATDC}$ (after top dead center) are 750 K and 5 atm, respectively. The pressure and temperature traces for 700 rpm are compared in Fig. 4.8(a) and (b): the differences between the results are of the same order as for the ignition delay. The profiles for selected species in Fig. 4.8(c) and (d) show excellent agreement for the major species and radicals even at very low concentrations. It should be noted that the skeletal mechanisms are constructed using data in the range $1 \leq p \leq 20$ atm, but in this case the pressure is increasing up to 47 atm. As mentioned in section 4.4.1, the agreement between the skeletal and detailed models are generally better at high pressures.

4.4.3 Premixed flame

The accuracy of the skeletal mechanisms generated using data for a homogeneous system were finally validated in an atmospheric 1-D laminar premixed flame with an unburned mixture temperature $T_u = 650$ K using the PRE-MIX code of CHEMKIN [87]. The laminar flame speed, S_L, is reproduced to within a maximum difference in the laminar flame speed for both R161 and R203 with respect to D561 that is less than 2 cm/s (Fig. 4.9(a)). The computed flame temperatures T_f are in excellent agreement (Fig. 4.9(b)). The flame structure is also accurately captured as shown in Fig. 4.10 for the stoichiometric mixture. The computational time with the skeletal mecha-
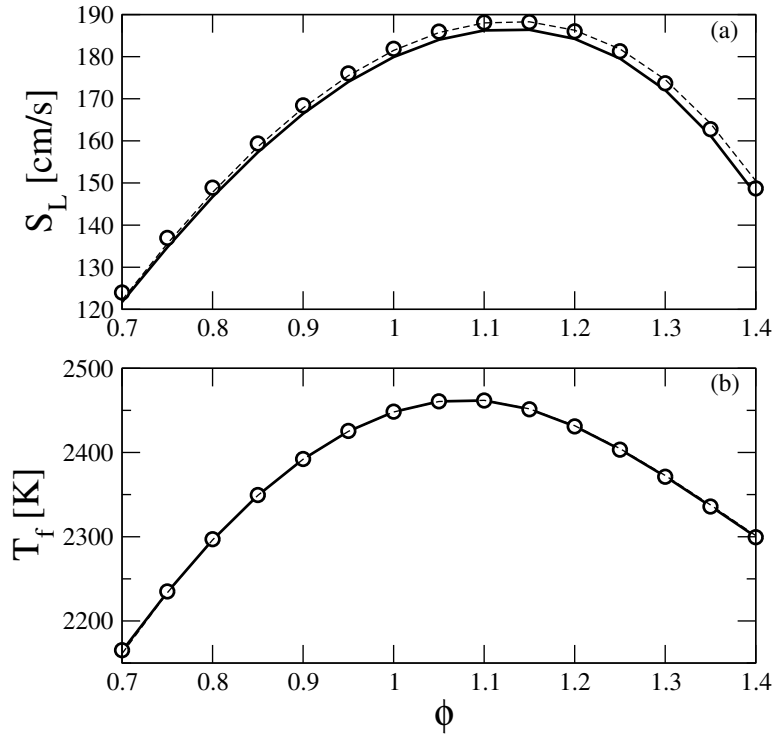
Figure 4.9: (a) Laminar flame speed S_L and (b) flame temperature T_f ($p = 1$ atm, unburned mixture temperature $T_u = 650$ K; D561: solid line, R203: circles, R161: dashed line).

nisms is at least one order of magnitude lower since the significant reduction in the number of species drastically reduces the computational cost for the evaluation of the right hand side and the Jacobian.

It should be stressed that Eq. (4.15) describes only the contribution of the reaction to the total entropy production. However, the premixed flame application demonstrates the validity of the skeletal mechanism generated using homogeneous reactor results. In a laminar flame the total entropy generation including not only chemical reactions but also, contribution of viscosity, heat conduction and mass diffusion. It has been shown however that the major process for entropy production is entropy generation due to
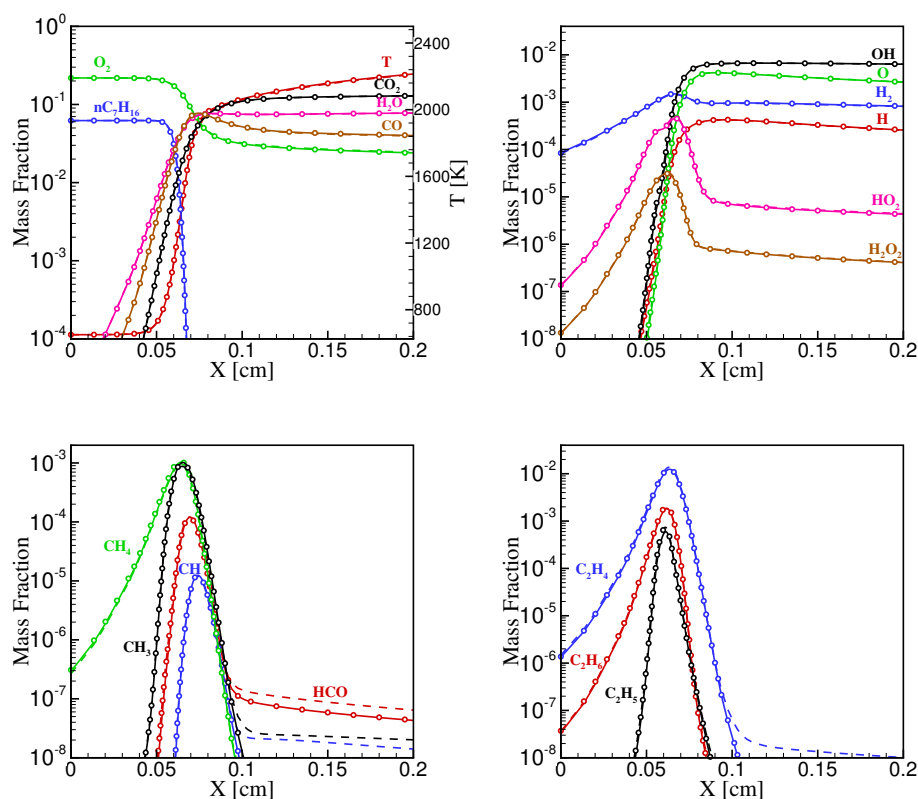
Figure 4.10: Temperature and selected species profiles of the premixed laminar flame ($p = 1$ atm, $T_u = 650$ K and $\varphi = 1$; D561: solid line, R203: circles, R161: dashed line).

the chemical reactions [139].

4.5 Conclusions

In this work, we have proposed and validated the entropy production analysis for the skeletal reduction of detailed mechanisms. Important reactions are identified based on their relative contribution to the total entropy production above a user-specified threshold. Application to the detailed LLNL2 mechanism for n-heptane with 561 species resulted in skeletal mechanisms

with 203 and 161 species. The same comprehensive mechanism has been used for skeletal reduction with different approaches. For $600 \leq T \leq 1800$ K, $1 \leq p \leq 40$ atm and $0.5 \leq \varphi \leq 1.5$, 188 species by DRG, and for $700 \leq T \leq 1100$ K, $6.5 \leq p \leq 40$ atm and $0.5 \leq \varphi \leq 2.0$, 177 and 185 species by CSP are available in the literature with comparable accuracy with the skeletal mechanisms found by entropy production analysis. The skeletal mechanisms exhibit good agreement not only for the homogeneous auto-igniting system and a single-zone engine model, but also for the spatially varying laminar premixed flames where diffusion plays an important role. In addition to the lower number of species, the skeletal mechanisms are less stiff than the detailed mechanism and computational implementations show significant speedup.

The proposed approach can be easily applied on large detailed mechanisms of realistic fuels to produce skeletal schemes with promising ratio of reduction (e.g. 71% reduction for R161). The physical basis of the entropy production analysis and the simplicity of the algorithm (see the appendix A) warrants the investigation of its potential for the efficient adaptive (on-the-fly) chemistry reduction.

Chapter 5

---

n-heptane/air complex dynamics

1

5.1 Introduction

The Perfectly Stirred Reactor (PSR) or Continuous Stirred Tank Reactor (CSTR) is commonly used to study complex chemical kinetics and combustion dynamics. In practice, such reactors can be realized by intense mixing using gas reactant jets in a jet-stirred arrangement [140]. Efficient mixing provides homogeneous conditions so that the reactor state at the exit is the same as inside and strongly simplifies its numerical modeling.

Since the rigorous analysis of Bilous and Amundson in 1955 [141] and the more comprehensive numerical study of Aris and Amundson [142], the reactor dynamics and stability for the single-step irreversible exothermic reaction R→ P have been investigated extensively, revealing interesting dynam-

---

ics, including multiple equilibria and hysteresis loops, super- and subcritical Hopf bifurcations, and complex oscillations (see, for example, [143–145]).

The dependence of the reactor state (indicated for example by the reactor temperature T) on τ, the residence time in the reactor, typically displays an S-shaped curve, connecting the weakly- and strongly-burning steady state branches via an unstable steady state branch between the ignition and extinction points, which define the sudden transitions from one stable state to another [146]. The lower branch of the bifurcation diagram that shows the possible long-term states drawn schematically in Fig. 5.1 starts from the chemically frozen state at very short residence time and remains weakly-reacting up to the residence time of ignition τ_{ign}, where the system state jumps to the strongly-burning branch. Starting from a state on the latter branch, the gradual decrease of τ will eventually lead the reactor back to the weakly-reacting state at τ_{ext}, the residence time of extinction. Steady state multiplicity exists for $\tau_{ext} \leq \tau \leq \tau_{ign}$, and the reactor operation becomes sensitive to external perturbations.

More complete pictures of the qualitative features of PSRs and phase portraits for various scenarios of bifurcation diagram have been obtained analytically and numerically for single-step reactions and lumped variables [147–149]. PSRs have also been investigated via Lyapunov's direct method [150], parametric sensitivity [151] as well as from the control and stabilization point of view (e.g. [152]). A discussion of earlier theoretical and experimental studies of ignition and cool flames in CSTRs can be found in the review of Griffiths and Scott [153], the book [145] and the references therein.
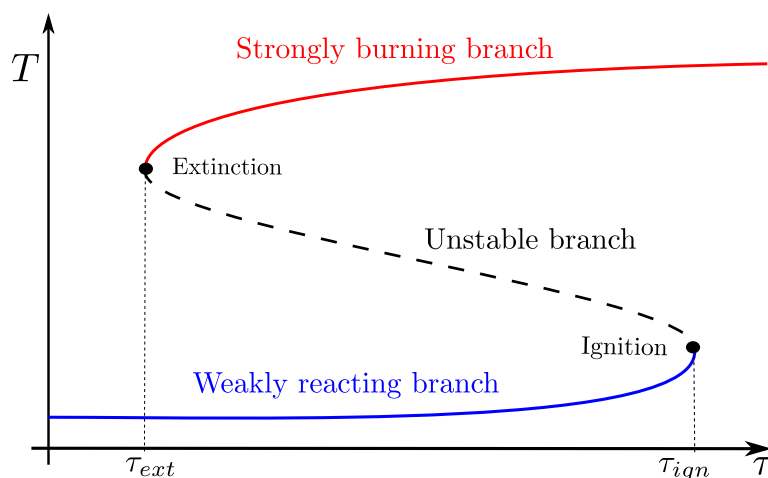
Figure 5.1: Typical S-shaped bifurcation diagram of a PSR temperature with respect to the residence time.

The ignition and extinction conditions are used for the validation and rate constant tuning of detailed and reduced mechanisms by comparison with experimental data (see, for example, [8]).

Although the dynamic behavior of PSRs using generic single- or few-steps reactions has been systematically analyzed in the literature, few studies have considered detailed reaction mechanisms. Numerical investigations of hydrogen combustion in isothermal PSRs [154–156] revealed complex dynamics which in addition to ignitions and extinctions included oscillations and birhythmicity (coexistence of two stable limit cycles for the same operating conditions). Sensitivity and principal component analysis at the bifurcation points were used to construct minimal reaction mechanisms that can predict state multiplicity [155]. Recent investigations of ignition/extinction behavior of more complex fuels like dimethyl ether [157,158] and n-heptane [159] in PSRs focused on the detection of important features with respect to the variation of a single parameter (the residence time) and

its effect on the type of extinction (sudden jump to the weakly-burning or extinguished state or dynamic extinction via oscillations of increasing amplitude) [158].

The complexity of the reaction mechanism in terms of the number of species and reactions increases dramatically with the size of the fuel molecule [160], and even for ideal homogeneous reactors like the PSR the computational cost becomes high, particularly when a large number of parameters determines the behavior. Thanks to the availability of efficient numerical continuation packages, the dynamic system analysis of single- or few-steps global reactions can be expanded to detailed mechanisms including hundreds of species and thousands of elementary reactions. The efficient scanning of the dynamics with respect to multiple operating parameters can identify the critical conditions leading to the transition between different reactor states and provide essential information not only to enhance our understanding of the phenomenology of combustion chemistry, but also for the design of experiments for probing different types of kinetics and for mechanism validation purposes.

In this chapter, we employ a skeletal mechanism of n-heptane constructed using the relative contribution of elementary reactions to the total entropy production [107] presented in chapter 4.

The bifurcation diagram summarizing the possible dynamics as well as the transitions leading from one state to another can be generated by finding the long-time state for the system of equations describing the dynamics for different values of the controlling parameter(s). In a brute force manner,

this can be achieved by numerical integration of the transient equations modeling the temporal evolution of the concentration and temperature in the reactor (see Sec. 5.2) to scan the parameter space for different initial conditions. However, this approach can only identify stable steady or oscillatory states.

The dynamics in a PSR is determined by five parameters: the residence time τ, inlet temperature T_0, pressure p, equivalence ratio φ and heat loss per unit volume $\dot{Q}_{loss}$, and the brute force method becomes impractical. Arc-length continuation methods [161] offer an accurate and more efficient way to track changes in the long-term behavior by starting from a particular solution and following it as one or more parameters are varied. The local stability can be determined by the eigenvalues of the Jacobian matrix obtained from the linearization of the governing equations around the desired state: eigenvalues with negative (positive) real parts define stable (unstable) states. In this work the AUTO-07p package [162,163] is employed to systematically follow the transitions in the observed behavior, first with respect to independent variations of τ and $\dot{Q}_{loss}$ for fixed values of the remaining parameters (one-parameter continuations), and then for the simultaneous variation of τ and T_0 (two-parameter continuation). The effect of equivalence ratio and pressure is assessed by computing the two-parameter diagrams for different values of φ and p to partially construct three-parameter diagrams. The observed dynamics include steady and oscillatory strongly-burning states and cool flames, multistability over extended ranges of operating conditions and higher co-dimension bifurcations.

As it was stated in chapter 4, entropy production analysis can also provide useful information about elementary reactions responsible for bringing the system state to equilibrium. In this chapter it is complemented by indices proposed in the context of the Computational Singular Perturbation (CSP) method to analyze the kinetics at the bifurcation points. The CSP analysis is performed on the mode with time scale corresponding to the positive or the least negative eigenvalue of the Jacobian matrix at the state of interest. The corresponding eigenvector, a first-order approximation to the CSP mode, is used to identify the most important reactions at extinction, ignition or oscillatory combustion with the help of the amplitude [39] and time scale participation [34] indices. More detailed CSP-based analyses of autoignition and the multi-stage ignition of *n*-heptane can be found in [164–166].

The work presented in this chapter is along the lines of the work of Lu and co-workers who studied combustion dynamics in PSRs for *n*-heptane [159], methane [157] and DME [157, 158]. One-parameter continuations with respect to the residence time were performed in these works focusing on ignition and extinction, and Chemical Explosive Mode Analysis (CEMA), a variant of the CSP method [167], was employed to analyze the kinetics.

The chapter is organized as follows: Following the presentation of the PSR governing equations in Sec. 5.2 and a brief discussion of numerical continuation in Sec. 5.3, the skeletal mechanism that was generated using entropy production analysis is presented in Sec. 5.4. The CSP analysis tools used are briefly reviewed in Sec. 5.5 before turning to the results of

numerical calculations both from the chemical kinetics and the dynamical system points of view in Sec. 5.6.

5.2 Governing equations

The production/consumption rate of the i-th species $\dot{\omega}_i$ is the summation of the rates of all reactions involving the species i

$$\dot{\omega}_i = \sum_{k=1}^{n_r} \nu_{ik} q_k \tag{5.1}$$

where $\nu_{ik} = \nu_{ik}'' - \nu_{ik}'$ is the net stoichiometric coefficient.

The temporal evolution of Y_i, the mass fraction of species i, and temperature T in a perfectly stirred reactor is described by a system of ordinary differential equations (ODEs)

$$\begin{aligned}
\frac{dY_i}{dt} &= \frac{1}{\tau}(Y_i^0 - Y_i) + \frac{\dot{\omega}_i W_i}{\rho} && i = 1, \cdots, n_s \\
\frac{dT}{dt} &= \frac{1}{\bar{c}_p \tau} \sum_{i=1}^{n_s} (h_i^0 - h_i) Y_i^0 - \frac{1}{\rho \bar{c}_p} \sum_{i=1}^{n_s} h_i W_i \dot{\omega}_i - \frac{\dot{Q}_{loss}}{\rho \bar{c}_p}
\end{aligned} \tag{5.2}$$

where Y_i^0 and h_i^0 are the mass fraction and total enthalpy of species i at the inflow, W_i and h_i the molecular weight and total enthalpy of species i, $\bar{c}_p$ and ρ the mixture heat capacity under constant pressure and density, and $\dot{Q}_{loss}$ the heat loss per unit volume. With the equivalence ratio φ defining the inlet composition Y_i^0, the system state is described by the $n_s + 1$ dimensional vector $\boldsymbol{z} = [Y_i, T]$, $i = 1, \cdots, n_s$ for specified values of the components of the five-dimensional parameter vector $\boldsymbol{\Gamma} = [\tau, \varphi, T_0, p, \dot{Q}_{loss}]$.

Starting from an initial condition $\boldsymbol{z} = \boldsymbol{z}(t = 0)$, the initial value problem (5.2) can be integrated for specified values of the parameters using the stiff ordinary differential equation solver DVODE [84] to compute the temporal evolution of the reactor state. The chemical source term and the thermodynamic properties are computed using CHEMKIN [104]. At long times the system evolves towards either a steady (equilibrium) or an oscillatory state (limit cycle or periodic orbit). In general, bounded solutions of systems of autonomous ODEs can also converge at long times to more complex attractors, like tori (quasi-periodic orbits) or strange attractors (chaotic orbits) (for example, see [168, 169]).

5.3 Numerical bifurcation analysis

Time integration can be used to explore the dynamics in a brute-force way for different combinations of parameters and initial conditions. In the general case, slight changes of the parameters result in small changes of the long-term dynamics, and the dynamical system displays structural stability. However, at critical parameter values small variations can lead to bifurcations where the change in the long-term dynamics can be dramatic. The corresponding values or the zero-, one- or multi-dimensional loci of the critical parameters define the bifurcations points, curves, or surfaces which separate the parameter space into regions characterized by similar long-term dynamics.

The system (5.2) can be written in the generic vector form

$$\frac{d\boldsymbol{z}}{dt} = \boldsymbol{f}(\boldsymbol{z}; \boldsymbol{\Gamma}) \tag{5.3}$$

Here, $\boldsymbol{z} \in \mathbb{R}^{n_s+1}$ is the system state, $\boldsymbol{\Gamma} \in \mathbb{R}^{n_\gamma}$ the vector of operating parameters, and the source term $\boldsymbol{f} : \mathbb{R}^{n_s+n_\gamma+1} \rightarrow \mathbb{R}^{n_s+1}$ is a smooth vector function satisfying the Lipschitz conditions. The brute-force approach is neither efficient in probing the dynamics nor accurate in determining the bifurcation points, particularly for high-dimensional phase and parameter spaces. The aim of numerical bifurcation analysis is to compute accurately and efficiently the long-term solutions of the corresponding set of the parameter-dependent nonlinear algebraic equations

$$\boldsymbol{f}(\boldsymbol{z}; \boldsymbol{\Gamma}) = 0 \tag{5.4}$$

defining the steady state of the system as some of the n_γ parameters of $\boldsymbol{\Gamma}$ are varied to compute the solution branches $\boldsymbol{z}(\boldsymbol{\Gamma})$.

For the sake of completeness, the basic notions and dynamic features observed in this study are summarized. For a more comprehensive discussion the reader is referred to [169]. For fixed parameter values, the phase portrait is the collection of solution trajectories of Eq. (5.3) in phase space, the $(n_s + 1)$-dimensional space in which all possible system states can be represented. At given parameter values $\boldsymbol{\Gamma^*}$ a fixed point is the steady state $\boldsymbol{z}^*$ satisfying $\boldsymbol{f}(\boldsymbol{z}^*; \boldsymbol{\Gamma^*}) = 0$. At long times, the system state may also evolve on a limit cycle, a closed trajectory in phase space that describes oscillatory

behavior. Together with fixed points they are the most commonly observed types of limit sets. If the qualitative structure of the phase portrait changes at $\boldsymbol{\Gamma} = \boldsymbol{\Gamma}^*$ then a bifurcation occurs, and $(\boldsymbol{z}^*; \boldsymbol{\Gamma}^*)$ defines the bifurcation point. The bifurcation diagram is the plot of some function of the state variable $\boldsymbol{z}$ at the limit set as a function of one or more components of the controlling parameters $\boldsymbol{\Gamma}$.

The *local* stability of a state can be characterized by eigenvalues and eigenvectors of the Jacobian matrix of the source term of (5.3), $\boldsymbol{J} = \frac{\partial \boldsymbol{f}}{\partial \boldsymbol{z}}$ [161, 169]. As the solution branch $\boldsymbol{\Gamma}$ is followed during variation of a single parameter, the eigenvalues follow trajectories when the real part is plotted vs the imaginary part on the complex plane, and bifurcations occur when the eigenvalue acquires a zero real part. In the generic case, when a real eigenvalue crosses zero at $(\boldsymbol{z}_{TP}; \boldsymbol{\Gamma}_{TP})$, two fixed points collide and disappear and the $(\boldsymbol{z}_{TP}; \boldsymbol{\Gamma}_{TP})$ is a turning point bifurcation. When a complex pair of eigenvalues crosses the imaginary axis at $(\boldsymbol{z}_{HB}; \boldsymbol{\Gamma}_{HB})$, a stable state loses stability and in the generic case a limit cycle is born. It can be shown that these co-dimension one bifurcation points (i.e. obtained by varying a single parameter) follow curves when a second parameter is varied simultaneously which can meet or cross at co-dimension two points. These higher co-dimension bifurcations play the role of organizing centers of lower-order bifurcations [169]. At a cusp bifurcation two turning point curves meet tangentially and the parameter space is divided into regions having different number of steady states. At a Bogdanov-Takens bifurcation, the linearization at the fixed point has a pair of real zero eigenvalue and satisfies some

114

technical non-degeneracy conditions [169]. At a double Hopf or Hopf-Hopf point the Jacobian has two pairs of purely imaginary eigenvalues.

The package AUTO-07p [162, 163] is used for the continuation and bifurcation analysis of the system of equations (5.2). In the combustion community, AUTO has been used to study the dynamics of the Belousov-Zhabotinsky reaction [170] and for hydrogen/air mixtures in PSRs [154,156]. In order to perform a comprehensive study of n-heptane in a PSR, AUTO-07p was coupled with the CHEMKIN library [104] so that complex reaction mechanisms can be readily accommodated.

Dynamical system analysis for high hydrocarbons is less common and the recent studies have mostly focused on the effect of varying the residence time on the reactor temperature [157–159]; the details of the employed continuation approach were not provided.

5.4 Validation of skeletal mechanism for n-heptane/air mixture for complex dynamics

A skeletal mechanism R161 which was validated for a wide range of thermodynamic conditions for auto-ignition in a constant pressure laminar premixed flames in chapter 4 ([107]) is considered.

Careful inspection of the results of time integration in a transient PSR revealed that 13 intermediate species that participate in important reactions appear only as reactants in irreversible reactions in the detailed mechanism. Since they cannot be produced, their concentration remains identically zero

and they can be safely removed to produce a skeletal n-heptane mechanism with 149 species in 669 reactions, referred to R149.

Continuation with respect to the residence time for a stoichiometric mixture of n-heptane and air with $T_0 = 650$ K and $p = 1$, 5 and 20 atm is shown in Fig. 5.2. Although not marked in the figure, the skeletal mechanism is able to capture accurately not only the turning but also the Hopf bifurcation points (table 5.1), which will be discussed in Sec. 5.6. It can

Table 5.1: Comparison of the bifurcation points computed with the detailed (D561) and the skeletal (R149) mechanisms; TP_i and HB_1 are as marked in Fig. 5.3 (adiabatic PSR at $T_0 = 650$ K, $\varphi = 1$).

	p [atm]	TP_1 $(\tau[s], T[K])$	TP_2 $(\tau[s], T[K])$	TP_3 $(\tau[s], T[K])$	HB_1 $(\tau[s], T[K])$
D561	1	$(2.32 \times 10^{-5}, 1735.4)$	$(1.02, 790.2)$	$(1.22 \times 10^{-3}, 706.5)$	$(1.04 \times 10^{-2}, 741.9)$
	5	$(6.35 \times 10^{-6}, 1846.1)$	$(6.38 \times 10^{-2}, 840.3)$	$(4.75 \times 10^{-4}, 749.6)$	$(3.13 \times 10^{-3}, 789.0)$
	20	$(2.78 \times 10^{-6}, 1981.4)$	$(7.24 \times 10^{-3}, 889.0)$	$(2.37 \times 10^{-4}, 789.9)$	$(9.21 \times 10^{-4}, 833.8)$
D149	1	$(2.33 \times 10^{-5}, 1739.2)$	$(1.08, 807.3)$	$(8.41 \times 10^{-4}, 717.3)$	$(6.98 \times 10^{-3}, 756.5)$
	5	$(6.39 \times 10^{-6}, 1849.5)$	$(7.34 \times 10^{-2}, 859.5)$	$(3.76 \times 10^{-4}, 760.1)$	$(2.29 \times 10^{-3}, 803.2)$
	20	$(2.81 \times 10^{-6}, 1983.8)$	$(8.93 \times 10^{-3}, 908.4)$	$(2.24 \times 10^{-4}, 800.3)$	$(7.09 \times 10^{-4}, 844.7)$

therefore be concluded that the skeletal mechanism provides an accurate description of the kinetics and retains high fidelity to the complex non-linear dynamics of n-heptane oxidation in comparison to the detailed mechanism.

5.5   CSP analysis

The processes contributing to the dominant time scale at the bifurcation points are investigated in Sec. 5.6 via algorithmic tools provided by the Computational Singular Perturbation.
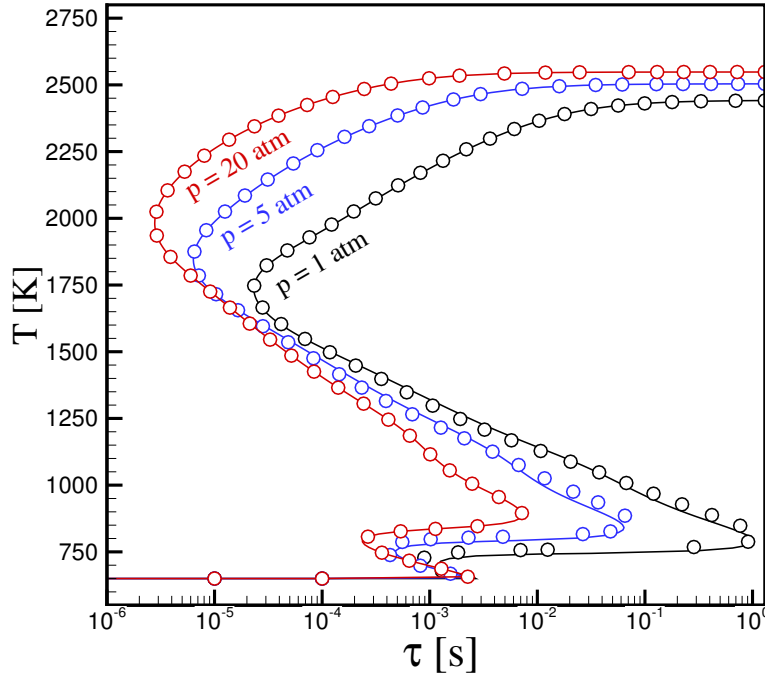
Figure 5.2: Comparison of the dependence of reactor temperature on the residence time for an adiabatic PSR at $T_0 = 650$ K, $\varphi = 1.0$ and various pressures using the detailed (solid lines) and skeletal (open circles) reaction mechanisms.

The system of equations (5.2) for an adiabatic PSR can be rewritten as

$$\frac{d\boldsymbol{z}}{dt} = \boldsymbol{g}(\boldsymbol{z}) = \boldsymbol{P}(\boldsymbol{z}) + \boldsymbol{L}(\boldsymbol{z}) \tag{5.5}$$

by decomposing the right hand side in terms of the chemical source term $\boldsymbol{P}(\boldsymbol{z})$

$$\boldsymbol{P} = \left[\frac{W_1 \dot{\omega}_1}{\rho}, \cdots \frac{W_{n_s} \dot{\omega}_{n_s}}{\rho}, -\frac{\sum_{i=1}^{n_s} W_i \dot{\omega}_i h_i}{\rho \bar{c}_p} \right]^{\mathrm{T}} \tag{5.6}$$

and the flow term $\boldsymbol{L}(\boldsymbol{z})$

$$\boldsymbol{L} = \left[\frac{Y_1^0 - Y_1}{\tau}, \cdots, \frac{Y_{n_s}^0 - Y_{n_s}}{\tau}, \frac{\sum_{i=1}^{n_s} Y_i^0 (h_i^0 - h_i)}{\bar{c}_p \tau} \right]^{\mathrm{T}} \tag{5.7}$$

117

The source term in equation (5.5) can be written as a matrix-vector product

$$\boldsymbol{g}(\boldsymbol{z}) = \boldsymbol{S}\boldsymbol{R} \tag{5.8}$$

where $\boldsymbol{S}$ is the $(n_s + 1) \times (2n_r + 1)$-dimensional generalized stoichiometric matrix

$$\boldsymbol{S} = \begin{bmatrix} \frac{W_1 \nu_{11}}{\rho} & \cdots & \frac{W_1 \nu_{1n_r}}{\rho} & \frac{-W_1 \nu_{11}}{\rho} & \cdots & \frac{-W_1 \nu_{1n_r}}{\rho} & \frac{Y_1^0 - Y_1}{\tau} \\ \frac{W_2 \nu_{21}}{\rho} & \cdots & \frac{W_2 \nu_{2n_r}}{\rho} & \frac{-W_2 \nu_{21}}{\rho} & \cdots & \frac{-W_2 \nu_{2n_r}}{\rho} & \frac{Y_2^0 - Y_2}{\tau} \\ \vdots & \vdots & \vdots & \vdots & \vdots & \vdots & \vdots \\ \frac{W_{n_s} \nu_{n_s 1}}{\rho} & \cdots & \frac{W_{n_s} \nu_{n_s n_r}}{\rho} & \frac{-W_{n_s} \nu_{n_s 1}}{\rho} & \cdots & \frac{-W_{n_s} \nu_{n_s n_r}}{\rho} & \frac{Y_{n_s}^0 - Y_{n_s}}{\tau} \\ \frac{-\Sigma_{i=1}^{n_s} h_i W_i \nu_{i1}}{\rho \bar{c}_p} & \cdots & \frac{-\Sigma_{i=1}^{n_s} h_i W_i \nu_{in_r}}{\rho \bar{c}_p} & \frac{\Sigma_{i=1}^{n_s} h_i W_i \nu_{i1}}{\rho \bar{c}_p} & \cdots & \frac{\Sigma_{i=1}^{n_s} h_i W_i \nu_{in_r}}{\rho \bar{c}_p} & \frac{\Sigma_{i=1}^{n_s} (h_i^0 - h_i) Y_i^0}{\bar{c}_p \tau} \end{bmatrix} \tag{5.9}$$

and $\boldsymbol{R} = [q_1^f, \cdots, q_{n_r}^f, q_1^r, \cdots, q_{n_r}^r, 1]^{\mathrm{T}}$ is the $(2n_r + 1)$-dimensional vector of the generalized rates of progress.

Consider a spectrum of time scales, τ_i, where the first F scales are much faster than the rest and there is a large gap between the F and $F+1$ time scales

$$\tau_1 < \cdots < \tau_F \ll \tau_{F+1} < \cdots < \tau_{n_s+1} \tag{5.10}$$

CSP [39] offers an algorithm to decompose the dynamics into iteratively refined modes, which span the fast and slow subspaces. Recasting Eq (5.8) in terms of the CSP modes, one can write

$$\boldsymbol{g} = \boldsymbol{g}_{fast} + \boldsymbol{g}_{slow} = \sum_{i=1}^{F} \boldsymbol{a}_i^{fast} m_{fast}^i + \sum_{i=F+1}^{n_s+1} \boldsymbol{a}_i^{slow} m_{slow}^i \tag{5.11}$$

where $\boldsymbol{a}_i$ is the $(n_s + 1)$-dimensional CSP column basis vector for the i-

th mode with amplitude $m^i = \boldsymbol{b}^i \cdot \boldsymbol{g}$. The complementary vector space element $\boldsymbol{b}^i$ is the CSP row basis vector satisfying orthogonality condition (written in Kronecker form) $\boldsymbol{b}^i \cdot \boldsymbol{a}_j = \delta_j^i$. Typically the F fastest time scales are dissipative, the corresponding CSP modes quickly become exhausted and the system state evolves on the slow subspace, which can then be approximated by

$$m_{fast}^i \approx 0 \quad i = 1, \cdots, F \tag{5.12}$$

The relaxation on the slow subspace is then governed by

$$\frac{d\boldsymbol{z}}{dt} \approx \boldsymbol{g}_{slow} \tag{5.13}$$

Local information for the system time scales can be obtained from $\boldsymbol{J_g}$, the Jacobian of $\boldsymbol{g}$. For real eigenvalues (complex pairs are treated as described in [112]), the CSP i-th mode can be distinguished with a time scale approximated by $\tau \approx |\lambda_i|^{-1}$, the i-th eigenvalue of $\boldsymbol{J_g}$ [171]. To leading order CSP vectors can be approximated by the right and left eigenvectors, i.e. $\boldsymbol{a}_i = \boldsymbol{v}_i$ and $\boldsymbol{b}^i = \tilde{\boldsymbol{v}}_i^{\mathrm{T}}$ [171], as they defined in chapter 2.

The decomposition approach presented above, leads to the introduction of different diagnostic tools to quantify the contribution of species and reactions or other processes to the CSP mode of interest. The i-th CSP mode can be characterized based on the sign of $Re(\lambda_i)$, the real part of the eigenvalue of $\boldsymbol{J_g}$. The CSP mode related to the positive or less negative eigenvalue plays the main role in limiting phenomena like ignition and extinction [157–159, 172–174].

The contribution of process k to the amplitude of the i-th CSP mode can be computed with the help of the *amplitude participation index* [39, 159, 164, 166]

$$\text{API}_k^i = \frac{(\tilde{\boldsymbol{v}_i}^{\text{T}} \cdot \boldsymbol{S_k}) R^k}{\sum_{k'=1}^{2n_r+1} |(\tilde{\boldsymbol{v}_i}^{\text{T}} \cdot \boldsymbol{S}_{k'}) R^{k'}|} \tag{5.14}$$

where $k = 1, \cdots n_r$ and $k = n_r + 1, \cdots, 2n_r$ correspond to the contribution of the forward and reverse reaction rates and $k = 2n_r + 1$ to the contribution of flow term. The API values are normalized to $[0, 1]$ and complex conjugate pairs of modes can be transformed into a pair of real modes as described in [112, 164].

The Jacobian matrix $\boldsymbol{J_g}$ can be decomposed based on the contribution of the processes,

$$\boldsymbol{J_g} = \sum_{k=1}^{2n_r+1} \boldsymbol{c}_k \tag{5.15}$$

where the $\boldsymbol{c}_k = \nabla(\boldsymbol{S}_k R^k)$ is the $(n_s + 1) \times (n_s + 1)$-dimensional gradient of the vector $\boldsymbol{S}_k R^k$. The i-th eigenvalue of $\boldsymbol{J_g}$ can then be written as,

$$\lambda_i = \tilde{\boldsymbol{v}}_i^{\text{T}} \cdot \boldsymbol{c}_1 \boldsymbol{v}_i + \cdots + \tilde{\boldsymbol{v}}_i^{\text{T}} \cdot \boldsymbol{c}_{2n_r+1} \boldsymbol{v}_i \tag{5.16}$$

and the normalized contribution of process k to the value of the i-th eigenvalue (i-th time scale) defines the *timescale participation index* [34, 158, 171, 175],

$$\text{TPI}_k^i = \frac{\tilde{\boldsymbol{v}}_i^{\text{T}} \cdot \boldsymbol{c_k} \boldsymbol{v}_i}{\sum_{k'=1}^{2n_r+1} |\tilde{\boldsymbol{v}}_i^{\text{T}} \cdot \boldsymbol{c}_{k'} \boldsymbol{v}_i|} \tag{5.17}$$

The analytic Jacobian matrix used in the CSP analysis is obtained by applying the automatic differentiation tool Tapenade [176] on the source code of

the transient PSR, and the eigenvalues and the left and right eigenvectors of the Jacobian were computed using LAPACK routines [177]. In the following, we will only analyze the mode corresponding to the leading eigenvalue, i.e. the one with positive or least negative real part, to identify the dominant process and reactions for ignition, extinction and oscillatory behavior.

In addition to the time scale analysis, entropy production, plays an important role in characterizing the reversibility of the system [178].

Chemical affinity, Gibbs free energy and entropy production are closely related [130,131]. The reactions which contribute more in the production of entropy are responsible for relaxing the system from the initial state towards the maximum entropy state (equilibrium) and can be ranked accordingly (see for example [179] for a combustion application). In this work, entropy production analysis will be applied at bifurcation points to identify the reactions which are responsible for combustion irreversibility.

5.6 Continuation and bifurcation analysis

In this section, the effect of the variation of the system parameters on the dynamics of n-heptane/air mixtures in adiabatic and non-adiabatic perfectly stirred reactors are investigated using AUTO-07p [163].
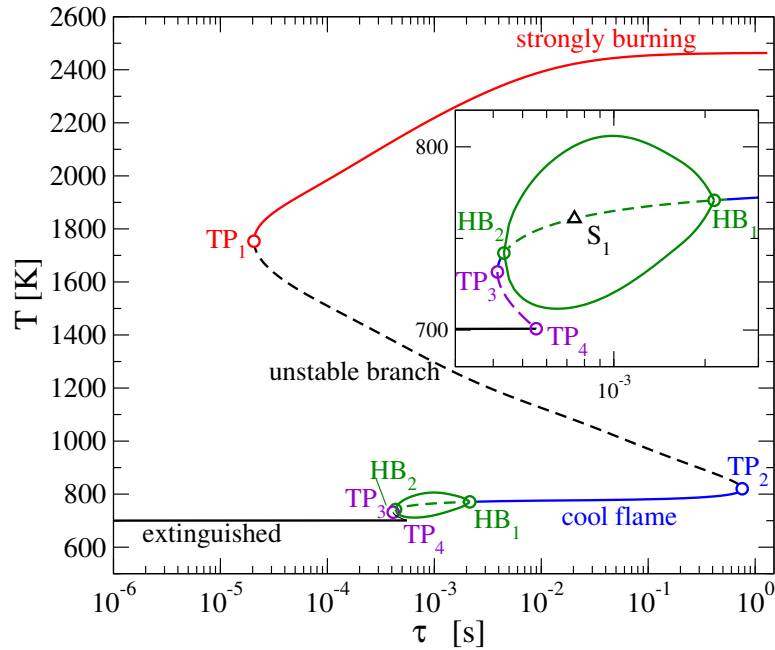
(a)
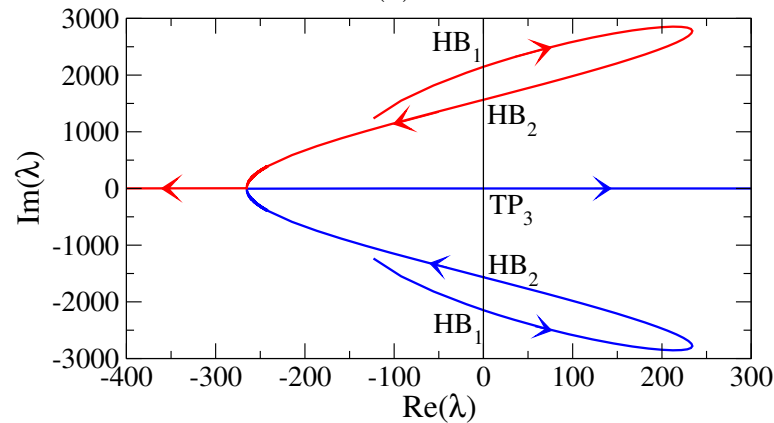
(b)

Figure 5.3: (a) Reactor temperature as a function of residence time for a stoichiometric *n*-heptane/air mixture ($p = 1$ atm, $T_0 = 700$ K) in an adiabatic PSR. Solid (dashed) lines indicate stable (unstable) states, while the solid curves between HB_1 and HB_2 of the expanded inset show the maximum and minimum reactor temperatures during the oscillations. (b) Trajectories of the leading eigenvalues along the cool flame branch for $\tau < 6 \times 10^{-3}$s.

5.6.1 One parameter continuations

5.6.1.1 Adiabatic reactor: effect of residence time

The bifurcation diagram for the combustion of a stoichiometric mixture in an adiabatic PSR at atmospheric pressure and inlet temperature $T_0 = 700$ K plotted in Fig. 5.3(a) displays five branches. In addition to the commonly observed strongly-burning state, the unburned or weakly-burning states and the connecting unstable branch shown in Fig. 5.1, the cool flame and a short unstable branch connecting it to the extinguished reactor state are found. The cool flame behavior is associated with a small increase of the reactor temperature ($732 \leq T \leq 820$ K) and is characteristic of higher hydrocarbons displaying multi-stage ignitions and the Negative Temperature Coefficient (NTC) regime [180]. The branches are separated by the four turning points TP_i and the analysis reveals two additional Hopf bifurcation points HB_i leading to oscillatory dynamics as discussed below. Similar results are reported in [159] for a $\varphi = 0.5$ mixture at $p = 10$ atm. The first turning point at $\tau_{TP_1} = 0.0206$ ms ($T_{TP_1} = 1753.5$ K) marks the extinction limit of the strongly-burning state as can be verified by time integration of the transient equations (5.2) starting from an initial condition at TP_1 with the initial reactor temperature reduced by 1 K: the response shows a fast drop of the reactor temperature to that of the inflowing mixture (Fig. 5.4(a)). The most contributing reactions to the total entropy production as well as the important reactions identified by time scale analysis of the CSP mode with positive eigenvalue are provided in Figs. 5.4(b), 5.4(c) and 5.4(d). At TP_1, the leading eigenvalue is zero. To avoid numerical difficulties with the
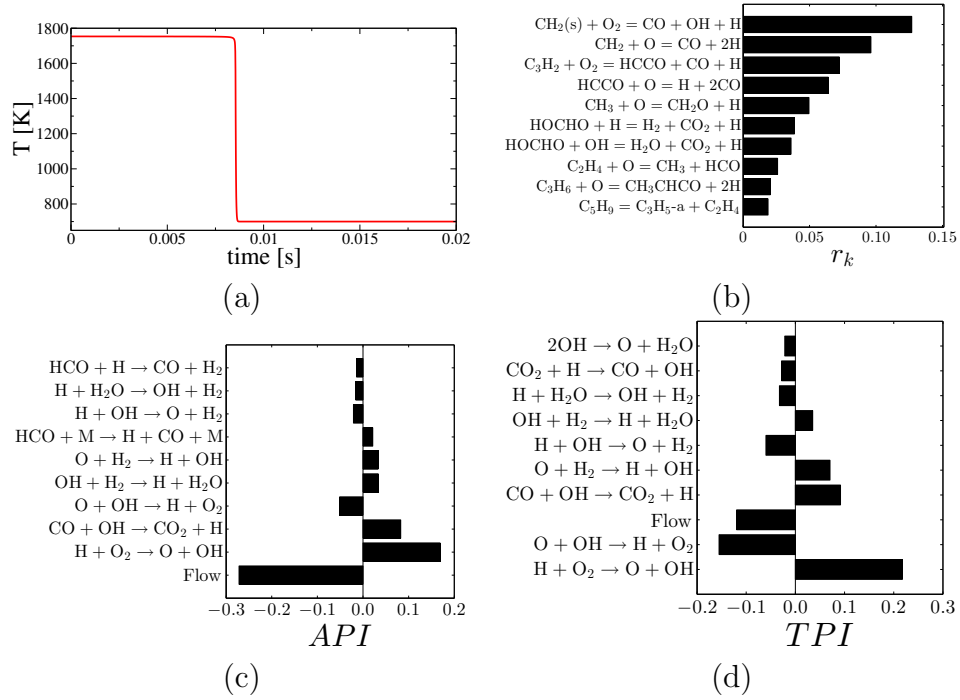
Figure 5.4: Extinction of the strongly-burning state at TP_1 (T= 1753.5 K, $\tau = 0.0206$ ms): (a) Temperature evolution in the transient PSR after reduction of the reactor temperature by 1 K, (b) Most contributing reactions in the total entropy production, (c) amplitude participation indices, (d) timescale participation indices ($p = 1$ atm, $T_0 = 700$ K).

infinite time scale, the CSP analysis was performed slightly to the right of the bifurcation point on the unstable branch. Although the leading eigenvalue changes rapidly around TP_1 the ordering of the reactions and the indices were found to be insensitive to the chosen point.

The APIs reveals that extinction is controlled by the competition between the flow (negative index as expected from the transition to the extinguished branch by an increase in the flow rate, i.e. decrease in the residence time) and the elementary reactions responsible for the main chain branching step at high temperatures, $H+O_2 \rightarrow O+OH$, and the main heat releasing

reaction, $CO + OH \rightarrow CO_2 + H$ (positive indices indicating that an increase in the rates of these reactions will favor the strongly-burning state). The dominant time scale at the chosen point ($\tau_1 = 1/\lambda_1 = 6.97 \times 10^{-4}$ s) is determined by the main chain branching reaction (positively in the radical-producing direction, negatively in the reverse direction) and negatively by the colder inflow. The main heat releasing step together with the secondary chain branching step $O + H_2 \rightarrow H + OH$ have a positive contribution. Entropy production and thus irreversibility is dominated by reactions including small molecules.
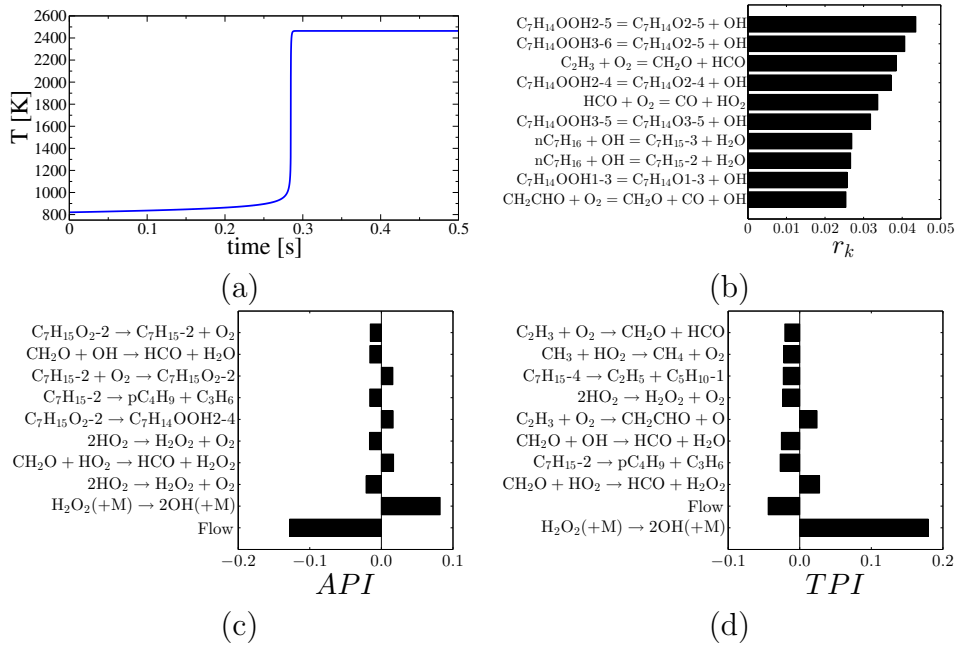
Figure 5.5: Ignition of the cool flame at TP_2 (T= 820.3 K, $\tau = 0.7571$ s): (a) Temperature evolution in the transient PSR after increasing the reactor temperature by 1 K, (b) Most contributing reactions in the total entropy production, (c) amplitude participation indices, (d) timescale participation indices ($p = 1$ atm, $T_0 = 700$ K).

The second turning point at $\tau_{TP_2} = 0.7571$ s ($T_{TP_2} = 820.3$ K) marks

the ignition conditions towards the strongly-burning state. Indeed, a 1 K increase of the initial reactor temperature from the conditions at TP$_2$ results in a jump to the strongly-burning state (Fig. 5.5(a)). Entropy production analysis reveals that reactions responsible for the breakup of heavy molecules are most important with respect to irreversibility (Fig. 5.5(b)). CSP analysis performed slightly to the left of TP_2 on the unstable branch (Figs. 5.5(c) and (d)) shows the clearly dominant role of the reaction H$_2$O$_2$ $\rightarrow$2OH, the main branching step at low temperature [181], both in the amplitude and in the time scale (τ_1 = 6.09 s) of the leading eigenmode. Flow has again a negative contribution. Similar findings are reported in [164,165] for autoignition of stoichiometric *n*-heptane/air mixtures in a constant volume batch reactor at 850 K and 13.5 bar.

Along the cool flame branch, the segment connecting the two supercritical Hopf bifurcation points HB$_1$ and HB$_2$ (dashed line in the inset of Fig. 5.3(a), with the solid lines marking the oscillation amplitude) defines the range of residence times for which the *n*-heptane cool flames exhibit oscillatory behavior. The trajectories of the complex pair of eigenvalues on the complex plain (imaginary part plotted against the real part) as τ is decreased from τ = 6 ms along the cool flame branch of Fig. 5.3(b) show the two crossings of the real axis at the Hopf bifurcation points HB$_1$ and HB$_2$, their meeting at τ = 4.13 ms to become real, and their subsequent trajectories along the real axis. One of them crosses to positive values at τ_{TP_3}.

The time history of the state initialized at point S$_1$ (τ = 0.7412 ms,

$T = 760.84$ K, Fig. 5.3(a)) shows the evolution to a limit cycle with a frequency of about 240 Hz (Fig. 5.6(a)). At the unstable steady state S_1, the kinetics are determined by the set of reactions shown in Figs. 5.6(b), (c) and (d). Reactions containing heavy molecules are most-contributing in the total entropy production. The APIs show that the dominant reactions are the dehydrogenation of n-heptane by hydroxyl radicals to produce different isomers of the heptyl radical C_7H_{15} and initiate the formation of the radical pool, while the flow term has the main negative contribution. In addition, ketohydroperoxide molecules are formed from isomerization of peroxy-alkylhydroperoxide radicals. The real part of the dominant eigenvalue at S_1 is positive. The TPI shows that the slowest timescale of the unstable state at S_1 ($\tau_1 = 4.51 \times 10^{-3}$ s) is due to the reactions $CH_2O+OH \rightarrow HCO+H_2O$ and $HO_2+OH \rightarrow H_2O$. At this point, flow has a contribution only on API, which is positively affected by the H abstraction reactions by the hydroxyl radical. As shown in [182] for a simple glycolysis model, CSP analysis can be used to identify the processes controlling the oscillatory behavior. For the high-dimensional n-heptane combustion, such a study is significantly more complicated and beyond the scope of this work.

The steady cool flame becomes stable for a narrow interval when $\tau < \tau_{HB_2}$, and eventually disappears for a shorter residence time at the third turning point TP$_3$ ($\tau = 0.413$ ms, $T = 731.72$ K, Fig. 5.3(a)). As shown in Fig. 5.7(a), a reactor initialized at a temperature slightly lower than T_{TP_3} evolves towards the inlet temperature; TP$_3$ corresponds to the first stage ignition point of n-heptane/air mixtures. The explosive mode amplitude

(a)

(b)

(c)

(d)
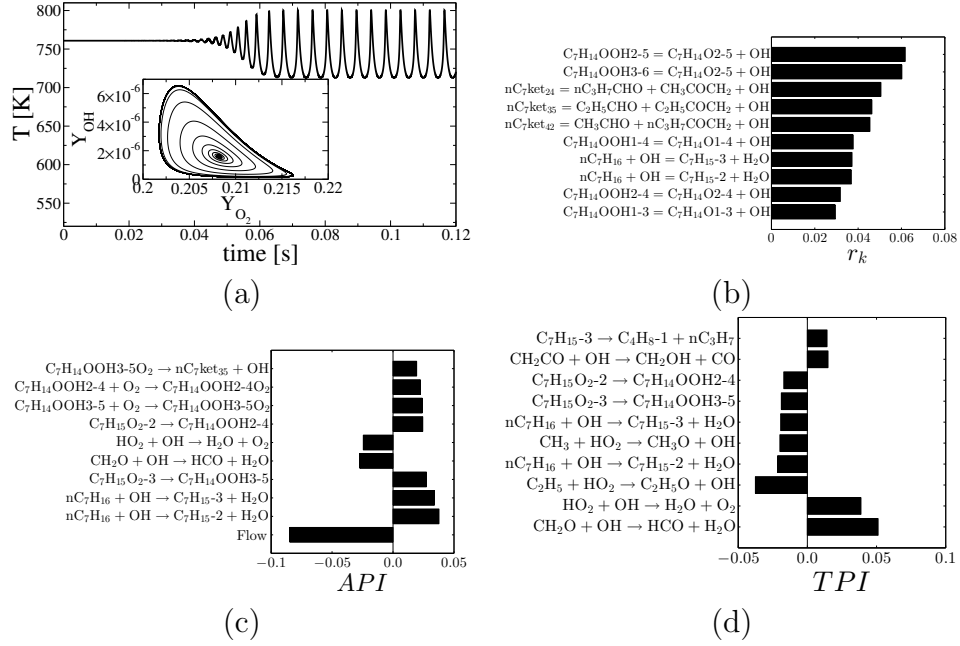
Figure 5.6: Oscillatory dynamics at the sample point S_1 ($\tau = 0.7412$ ms, T= 760.84 K): (a) Temperature evolution in the transient PSR together with a projection of a sample trajectory on the (Y_{OH}, Y_{O_2}) phase plane, (b) most contributing reactions in the total entropy production, (c) amplitude participation indices, (d) timescale participation indices ($p = 1$ atm, $T_0 = 700$ K).

is very sensitive to the residence time, while chemistry is dominated by isomerization (internal H-atom abstraction) and dehydrogenation reactions via OH and O_2 (Figs. 5.7(c) and (d)). For low temperature ignition of n-heptane, the same class of reactions are found to dominate the oxidation path in [137]. All along the cool flame branch, entropy is produced by reactions involving large molecules.

Finally, another unstable branch connects the cool flame to the extinguished reactor state at the fourth turning point TP_4 at $\tau = 0.56$ ms and $T = 700.0013$ K (expanded inset in Fig. 5.3(a)).
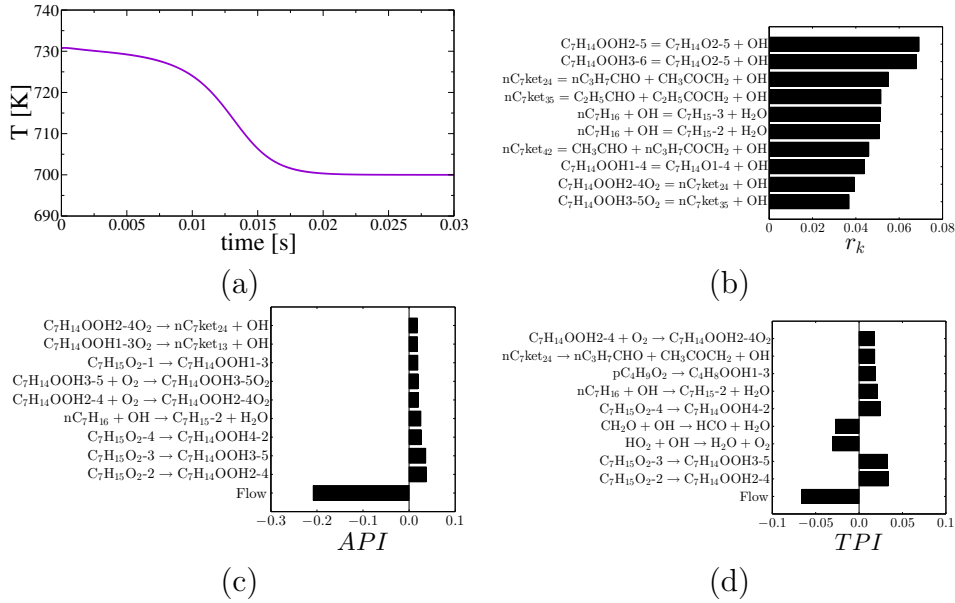
Figure 5.7: Cool flame extinction limit TP$_3$ (T= 731.72 K, τ = 0.413 ms): (a) Temperature evolution in the transient PSR after decreasing the reactor temperature by 1 K, (b) most contributing reactions in the total entropy production, (c) amplitude participation indices, (d) time scale participation indices ($p = 1$ atm, $T_0 = 700$ K).

5.6.1.2 Adiabatic reactor: effect of equivalence ratio

According to Fig. 5.3(a), the stoichiometric mixture in a PSR with $\tau = 1$ ms can support three steady states with reactor temperatures equal to 2219 K (stable, strongly-burning), 1296 K (unstable intermediate state) and 765 K (unstable cool flame), and one stable oscillatory state around the cool flame. The effect of the variation of φ on the reactor temperature is shown in Fig. 5.8. Three branches can again be seen, but the bifurcation diagram in this case displays an isola containing the stable strongly-burning state and the unstable branch within the flammability range $0.325 \leq \varphi \leq 2.582$, which is not connected to the cool flame branch. The maximum temperature of the strongly-burning state occurs slightly on the rich side of the fuel

equivalence ratio φ, as expected from the off-stoichiometric peak of the adiabatic flame temperature for hydrocarbon/air mixtures [146]. The isola is clearly separated from the cool flame branch which extends over the whole range of φ with temperatures $T_0 \leq T \leq 793.8$ K. Since for $\varphi \geq 2.582$ the cool flame is the only steady reactor state, its kinetics can be isolated and effectively studied. The changes in the bifurcation diagram that lead
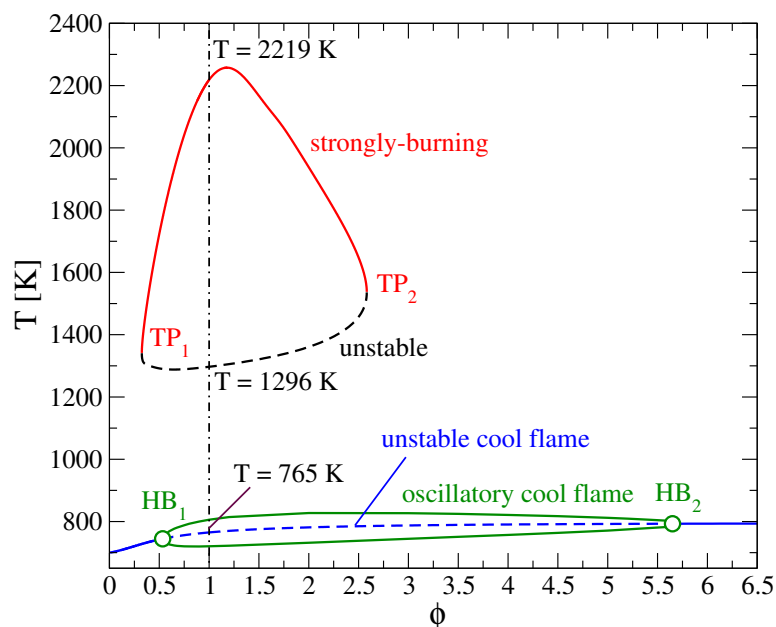
Figure 5.8: Dependence of the reactor temperature on equivalence ratio for the adiabatic PSR at $p = 1$ atm, $T_0 = 700$ K and $\tau = 1$ ms. Solid (dashed) lines indicate stable (unstable) steady states.

to the formation of the isola as the residence time is varied are shown in Fig. 5.9. The isola exist for $\tau \leq 0.1$ s (Fig. 5.9(c)), but disappear for $\tau = 0.2$ s (Fig. 5.9(b)) after the unstable and the cool flame branch merge at some intermediate residence time. For $\tau = 1$ s the bistability region shrinks to $0.172 \leq \varphi \leq 0.775$, and at long enough residence times the $T - \varphi$

diagram will assume the familiar shape of the adiabatic flame temperature vs. equivalence ratio curve [146]. At low residence times the size of the isola, and with it the flammability range, decrease and at sufficiently low τ the cool flame branch disappears (reactor temperature equal to T_0, Fig. 5.9(f)).
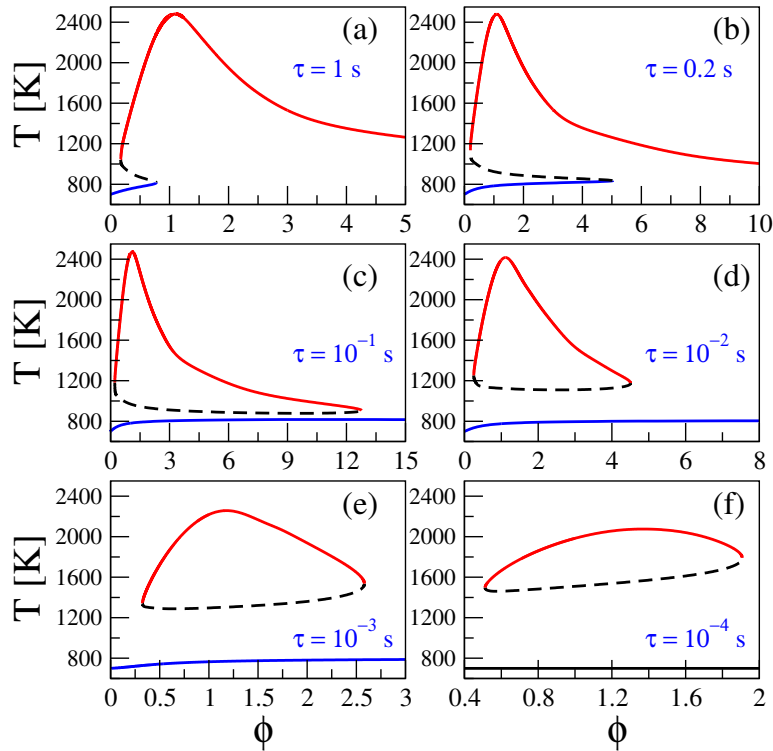
Figure 5.9: The dependence of temperature reactor on the equivalence ratio in the adiabatic PSR with $T_0 = 700$ K and $p = 1$ atm at (a) $\tau = 1$ s, (b) $\tau = 0.2$ s, (c) $\tau = 10^{-1}$s, (d) $\tau = 10^{-2}$s, (e) $\tau = 10^{-3}$s, (f) $\tau = 10^{-4}$s.

5.6.1.3 Effect of heat loss

The dependence of the reactor temperature on heat loss for the stoichiometric mixture at atmospheric pressure and for $\tau = 1$ s and $T_0 = 700$ K is depicted in Fig. 5.10. At these conditions, the adiabatic ($\dot{Q}_{loss} = 0$) reactor can only operate at the strongly-burning state ($T = 2463$ K), but as the

heat loss increases the reactor temperature decreases and hysteretic behavior is observed. Two turning points mark the conditions where no strongly-burning state (TP$_1$, $\dot{Q}_{loss} = 0.67$ kJ/s·m^3) or cool flame (TP$_2$, $\dot{Q}_{loss} = 0.02$ kJ/s·m^3) can be supported in the reactor, while the existence of the Hopf bifurcation point HB ($\dot{Q}_{loss} = 0.614$ kJ/s·m^3, $T = 1201.3$ K) before TP$_1$ indicates that the strong flame extinguishes dynamically. The solid curves emanating from HB in the inset of Fig. 5.10 and marking the oscillation amplitude show that the limit cycle exists for $\dot{Q}_{loss_{HB}} \leq \dot{Q}_{loss} < 0.6459$ kJ/s·m^3 and indicate that it is destroyed in a global bifurcation which is difficult to locate in such a high-dimensional phase space.
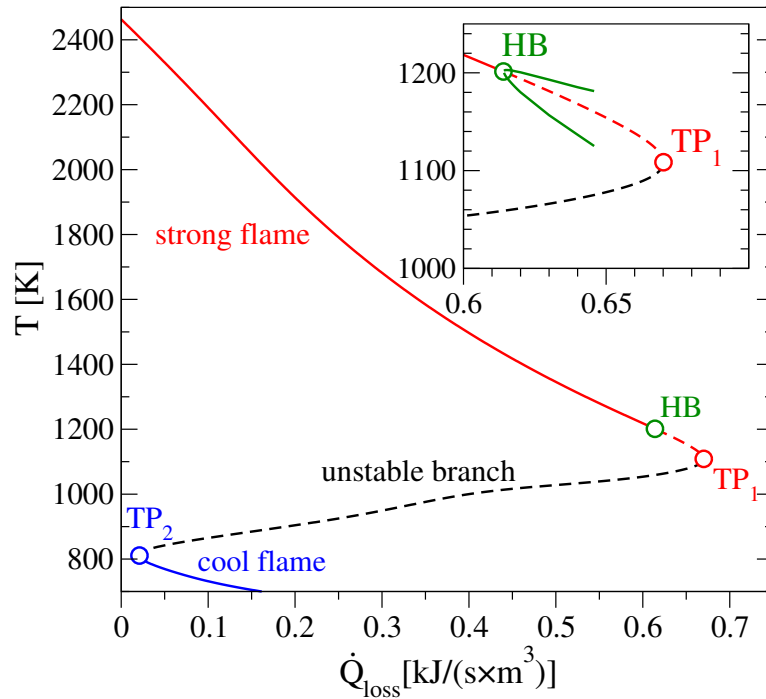
Figure 5.10: The dependence of temperature reactor on heat loss in the PSR ($\varphi = 1.0, T_0 = 700$ K, $p = 1$ atm and $\tau = 1$ s). Solid (dashed) lines indicate stable (unstable) branches.

The long-term behavior along the unstable branch connecting the HB point to the TP_1 point in Fig. 5.10 becomes very sensitive to the initial condition. Fig. 5.11 shows that for $\dot{Q}_{loss} = 0.646$ kJ/(s×m³) starting from two initial conditions taken along the dashed line connecting HB to TP_1 in Fig. 5.10 and slightly perturbing the reactor temperature, either a multi-period limit cycle ($T = 1140$ K, Fig. 5.11(a)) or extinction ($T = 1137.8$ K, Fig. 5.11(b)) can be observed.
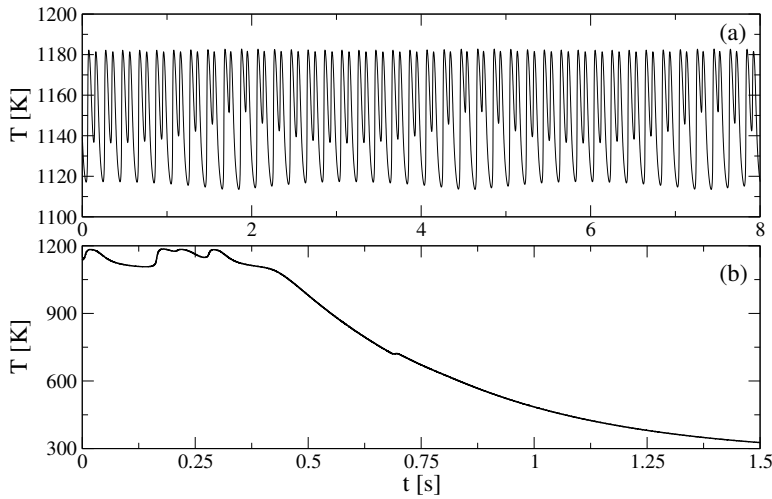
Figure 5.11: Temporal evolution of the reactor temperature for non-adiabatic PSR with $\dot{Q}_{loss} = 0.646$ kJ/(s×m³) ($p = 1$ atm, $T_0 = 700$ K, $\varphi = 1$, $\tau = 1$ s). Different initial conditions results in (a) multi-period transient solution for initial $T = 1140$ K, or (b) dynamic extinction for $T = 1137.8$ K.

Isolas also exist in the non-adiabatic case as shown in Fig. 5.12 for $\dot{Q}_{loss} = 0.1\frac{kJ}{s×m^3}$. Hopf bifurcation points are found along the unstable (inset inside the isola) and the cool flame branch (inset at lower left corner). The oscillations for $\tau_{HB_1} \leq \tau \leq \tau_{TP_2}$ have amplitudes of about 10 K and the period increases with increasing residence time (Fig. 5.12(b)-(c), periods

of 0.12 and 0.17 s, respectively). Close to the turning point, the reactor operation is characterized by long intervals (close to 70 s) of slow increase of the temperature followed by oscillations with a period of approximately 0.3 s (Fig. 5.12(d)), indicating that the limit cycle disappears at a global bifurcation involving the nearby saddle point [169].
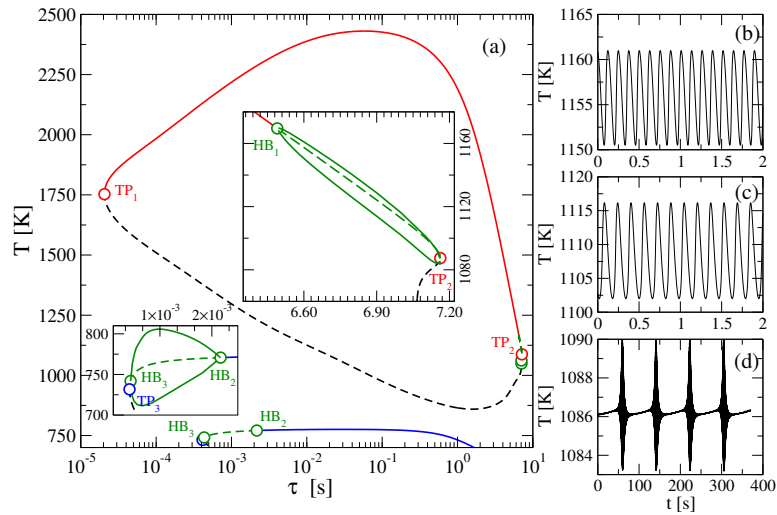
Figure 5.12: (a) Dependence of reactor temperature on residence time for non-adiabatic PSR with $\dot{Q}_{loss} = 0.1$ kJ/(s×m^3) ($p = 1$ atm, $T_0 = 700$ K, $\varphi = 1$); time history of reactor temperature for (b) $\tau = 6.6$ s, (c) $\tau = 7.0$, (d) $\tau = 7.1605$. Solid (dashed) lines indicate stable (unstable) branches.

5.6.2   Multi-parameter continuation

Continuation of the turning and Hopf bifurcation points while simultaneously varying two parameters results in bifurcation curves which delineate regions on parameter planes with similar dynamics. For the 150-dimensional system considered here, the two-parameter continuation with AUTO-07p requires careful choice of the numerical parameters and the bifurcation dia-

gram had to be constructed in a piecewise manner.

5.6.2.1 Adiabatic reactor: effect of residence time and inlet mixture temperature

We now consider the effect of the simultaneous variation of the residence time and the inlet temperature on the four turning and the two Hopf bifurcation points of Fig. 5.3(a). The results are plotted in Fig. 5.13(a) together
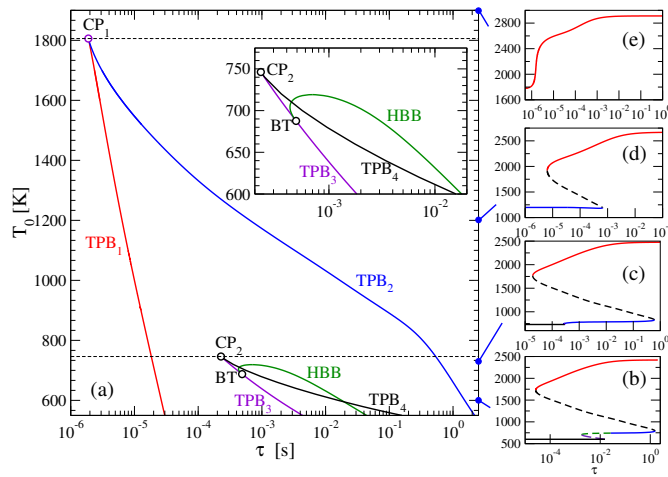
Figure 5.13: (a) Two-parameter (T_0–τ) continuation of the turning and Hopf bifurcation points of the adiabatic PSR at $p = 1$ atm and $\varphi = 1$; one-parameter bifurcation diagrams (b) for for $T_0 = 600$ K, (c) for for $T_0 = 730$ K, (d) for for $T_0 = 1200$ K, (e) for for $T_0 = 1900$ K. Colors are the same as in Fig. 5.3(a).

with one-parameter diagrams at selected T_0 (Figs. 5.13(b)-(e); Fig. 5.3 should also be consulted for the notation). The turning point branches for the cool flame ignition (TPB$_2$) and the strong state extinction (TPB$_1$) meet tangentially at the cusp point CP$_1$ for an impractically short residence time $(\tau, T_0) = (1.9 \times 10^{-6}\text{s}, 1805.9\text{K})$, and the parameter ranges between them define the regime of multistability. To the left of the TPB$_1$ bifurcation

135

curve and for inlet temperature lower than the T_{CP_1} the residence time is so low that the reactor cannot be ignited at any inlet mixture temperature. Similarly, the turning point branches for the cool (TPB$_3$) and the extinguished reactor (TPB$_4$) states meet tangentially at the second cusp point CP$_2$ ($\tau = 2.3 \times 10^{-4}$ s and $T_0 = 746.5$ K), and the parameter range between them defines the conditions for the coexistence of the two states.

For inlet temperatures higher than $T_{CP_1} = 1805.9$ K, the reactor can only operate at the strongly-burning state, irrespective of the residence time (Fig. 5.13(e)). In the range of parameters between the bifurcation curves TPB$_1$ and TPB$_2$ and the two horizontal dashed lines passing though the CP$_1$ and CP$_2$, two steady (weakly- and strongly-burning states) and one unstable steady state will be observed (Fig. 5.13(d)).

In the range between TPB$_1$ and TPB$_2$ and below the lower dashed line, the dynamics become more complex, involving up to seven possible limit sets: three steady and stable (unreacted mixture, cool and strongly-burning state), three unstable steady states, and oscillatory cool flames. At inlet temperature $T_0 = 550$ K, the lower limit for which the detailed mechanism is valid [4], one Hopf bifurcation point always exists for a residence time between the second (TPB$_2$) and the third (TPB$_3$) turning points (i.e., along the cool flame branch), as it can be seen in Fig. 5.13(b) for $T_0 = 600$ K. It turns out that the second Hopf point emerges from the saddle-node TPB$_3$ locus at $\tau = 0.4898$ s, $T_0 = 687.58$ K. The HBB and TPB$_3$ curves meet tangentially at a Bogdanov-Takens (BT) bifurcation point of co-dimension two where the steady state has a double-zero eigenvalue [169]. As the value

of inlet temperature is further increased, the turning point and the second Hopf point, move apart and two Hopf points begin to move closer together until finally HB_1 and HB_2 coalesce at the double Hopf bifurcation point $(\tau, T_0) = (7 \times 10^{-4}\text{s}, 719.1\text{K})$, another bifurcation point of co-dimension two, where two pairs of complex conjugate eigenvalues change their signs simultaneously at a double Hopf bifurcation point. For $719.1 < T_0 < T_{CP_2}$ K, the whole cool flame branch is steady, as can be seen in Fig. 5.13(c).

As mentioned, high co-dimension points act as organizing centers for the dynamics (see [169] for the details on the expected behavior around such points). However, for high-dimensional systems like the one considered here it is difficult to show the expected behavior, which includes global bifurcations. Figure 5.14(a) shows only the transient behavior of a PSR initialized at a residence time slightly lower than BT. The reactor state starts to oscillate with increasing amplitude. Due to the low residence time compared to BT point, the cool flame cannot sustain itself, it extinguishes suddenly and the reactor temperature returns to the inlet value.

The entropy production and the CSP analysis of the mode with positive eigenvalue at the conditions of the BT point are provided in Figs. 5.14(b), (c) and (d).

Some of the dynamics mentioned above occurs in narrow ranges of inlet temperatures and sometimes for very short residence times and would therefore be difficult to observe experimentally. Nevertheless, two-parameter diagrams like Fig. 5.13 provide invaluable information for understanding the combustion dynamics and to guide experiments in PSRs to parameter
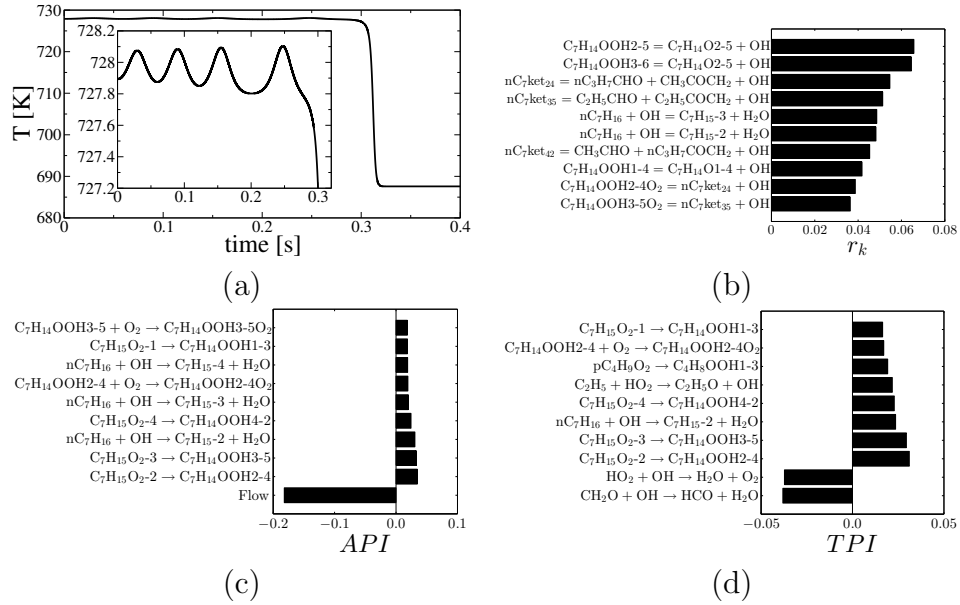
Figure 5.14: The analysis of Bogdanov-Takens bifurcation point, BT ($T_0 = 687.58$ K, T $= 727.89$ K, $\tau = 0.4898$ ms): (a) Temperature evolution in the transient PSR after small perturbation in reactor temperature, (b) Most contributing reactions in the total entropy production, (c) Amplitude participation indices, (d) Time scale participation indices ($p = 1$ atm and $\varphi = 1$).

regions where the kinetics at different regimes can be effectively probed. Continuation with respect to additional parameters can help to identify parameter ranges that are more amenable to experimental investigation.

5.6.2.2 Adiabatic reactor: effect of pressure and equivalence ratio on the $\tau - T_0$ bifurcation diagram

The effect of pressure and equivalence ratio on the $\tau - T_0$ bifurcation diagram can be studied by computing the curves for different values of p and φ.

At higher pressure the observed bifurcations do not change, but the branches of the critical curves shift to lower residence times rendering the
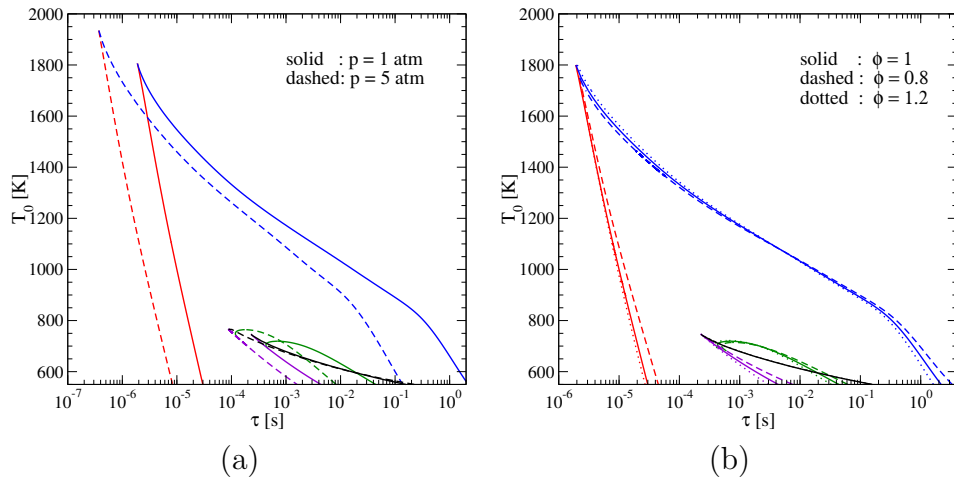
Figure 5.15: Effect of (a) pressure and (b) equivalence ratio on the $\tau - T_0$ two-parameter continuation diagrams (adiabatic PSR working at stoichiometric conditions).

strongly-burning state more dominant (Fig. 5.15(a)). The range of inlet temperatures leading to cool flame oscillations widens, but the reduction in the range of τ make their experimental investigation more difficult. The inlet composition is found to have only a minor effect on the dynamics for $\varphi = 0.8, 1.0$, and 1.2 (Fig. 5.15(b)). Figure 5.15 can be considered as a projection of the three-parameter bifurcation diagram on the two-parameter space $\tau - T_0$. By repeating the analysis for different pressures or equivalence ratios, a three-parameter diagram can be constructed.

5.7 Conclusions

The complex dynamics and bifurcations of high hydrocarbons like n-heptane in perfectly stirred reactors can be systematically investigated using a combination of time integration of the transient PSR equations and single- and

multi-parameter continuation and stability analysis with AUTO-07p [163]. The study is carried out with a skeletal mechanism with 149 species and 669 elementary reactions constructed by applying the proposed entropy production analysis method (chapter 4 and [107]) on the detailed LLNL2 scheme [136] (561 species and 2539 reactions). Ignition delay time and flame speed over an extended range of conditions and the bifurcation points in the PSR computed with the skeletal mechanism are in very good agreement with the results computed with the detailed mechanism.

The reactor stability was investigated with respect to the residence time τ, inlet temperature T_0, pressure p, inlet mixture equivalence ratio φ and heat loss $\dot{Q}_{loss}$. Multiple turning and Hopf bifurcation points were found in the continuation with respect to τ defining the bifurcation values and showing that up to six limit sets can coexist for the same operating conditions, both physically-realizable (steady and stable: extinguished reactor, cool flames and strongly-burning state, or unsteady: cool flame oscillations) as well as unphysical (unstable steady states along the branches connecting either the turning points defining the conditions for ignition and extinction or Hopf bifurcation point leading to the oscillatory dynamics). The kinetics at the bifurcation points were analyzed with the help of the importance and amplitude indices of Computational Singular Perturbation to identify the important reactions for the explosive mode corresponding to the eigenvalue with positive or least negative real part and entropy production analysis which points to the reactions contributing most to irreversibility. Continuation with respect to equivalence ratio revealed isolas, and their appearance

was studied by varying the residence time. With respect to heat loss, a Z-shaped curve was obtained, and the extinction of the strongly-burning reactor was found to be dynamic (oscillatory extinction). Time integration indicated that global bifurcations also play an important role in the dynamics.

Two-parameter continuation with respect to τ and T_0 revealed the range of conditions of the different steady and oscillatory states. Co-dimension two bifurcation point (cusp, Bogdanov-Takens and double Hopf) were found, but the high-dimensionality of the system complicates their detailed investigation. The effect of pressure and equivalence ratio on the two-parameter diagram was also studied. Increasing pressure for a stoichiometric mixture in an adiabatic PSR was found to shift the critical curves to lower residence time, but the bifurcations between different states was unaffected. Equivalence ratio variations in an atmospheric pressure adiabatic PSR have only a minor effect.

To the best of the authors' knowledge this is the first comprehensive and systematic study of the combustion dynamics of a high hydrocarbon in perfectly stirred reactors. However, the complexity resulting from both the high dimensionality of the dynamical system and the large number of parameters hinder the exploration of all possible behaviors. A lot remains to be done, particularly in terms of exploring different combinations of parameters, locating and tracking global bifurcations, and analyzing the wealth of the generated information to probe and understand the reaction kinetics determining the critical conditions.

The numerically predicted ranges of different dynamics can guide experimental investigations to interesting conditions, which will provide data for the validation or iterative refinement of detailed reaction mechanisms.

Chapter 6

Non-Perturbative Hydrodynamic Limits: A case study [1]

6.1 Introduction

The derivation of hydrodynamic equations from the Boltzmann kinetic equation is the classical problem of statistical mechanics. The best known technique, the Chapman-Enskog (CE) method [54], is a perturbation method based on a small parameter (Knudsen number). While the formal derivation of the Navier-Stokes equation from the Boltzmann equation by this method is a textbook example of the success of statistical physics, many problems related to the hydrodynamic limit of the kinetic equations remain unsolved [51]. The CE perturbation expansion fails as the post-Navier-Stokes hydrodynamic equations (e.g. Burnett's equations) are unstable [183]. Moreover, even at the Navier-Stokes level, the rate of dissipa-

---

[1]The content of the present chapter is published in Karlin, I. V., Chikatamarla, S. S., & Kooshkbaghi, M. (2014). Non-perturbative hydrodynamic limits: A case study. *Physica A: Statistical Mechanics and its Applications, 403*, 189-194.

tion (by viscosity, thermal conductivity or diffusion) is unbounded which contradicts the finiteness of relaxation times in the kinetic picture. Finally, as pointed out by many authors (e.g. [184]), the smallness parameter of the problem is not a fixed quantity (unlike, for example, the fine structure constant in quantum electrodynamics) but can be always scaled out.

All this points at the inability of the CE method to tackle the above problem, and non-perturbative approaches are sought. To that end, minimal kinetic theories such as Grad's finite-moment systems have been studied in detail [53, 56], including the *exact* summation of the entire CE series. Some results obtained along these lines are surprising. For example, Slemrod [184] noted that exact summation of the CE expansion results in hydrodynamic equations of Korteweg's type (that is, containing the capillarity-type contribution) rather than a (modified) Navier-Stokes equation. However, results for the kinetic equations, that is, for infinite moment systems remained almost entirely unexplored due to lack of analytical non-perturbative techniques.

In this chapter, we introduce a novel analytic approach to extract non-perturbatively the hydrodynamic component out of the kinetic equations. We consider in detail a model kinetic equation, and derive an exact invariance equation which is in striking resemblance with the Schwinger-Dyson equation of non-perturbative field theories. Based on the exact solution to the invariance equation, we build up a systematic non-perturbative extension procedure and show its relation to the conventional Chapman-Enskog method. The present approach can be used beyond the model kinetic equa-

tion considered below, and we outline some further steps towards the non-perturbative hydrodynamic limit.

6.2 Non-perturbative derivation of hydrodynamic manifold

We consider the one-dimensional kinetic equation for the distribution function $f(x, v, t)$:

$$\partial_t f = -v\partial_x f - \tau^{-1}\left(f - f^{\text{eq}}\right), \tag{6.1}$$

where the local equilibrium has the form

$$f^{\text{eq}} = n(x, t)\left(2\pi k_B T/m\right)^{-1/2} e^{-\frac{mv^2}{2k_B T}}, \tag{6.2}$$

with $n(x, t)$ the locally conserved density,

$$n = \int_{-\infty}^{\infty} f(v, x, t)dv. \tag{6.3}$$

and ∂_t, ∂_x denote differentiation with respect to time and spatial direction. The conventional CE analysis of (6.1) is to introduce a small parameter ε: $\tau \to \varepsilon\tau$, and to expand, $f = f^{(0)} + \varepsilon f^{(1)} + \ldots$, in order to produce a closure to the balance equation, $\partial_t n = -\partial_x j$, where $j = \int_{-\infty}^{\infty} vf dv$ is the density flux. One easily computes the first two terms of the CE closure, $\omega_{\text{CE}}^{(2)} = \varepsilon D\partial_x^2$ (first approximation; this is the conventional diffusion); $\omega_{\text{CE}}^{(4)} = \varepsilon D\partial_x^2 + \varepsilon^2 D^2 \partial_x^4$ (second approximation), where $D = \tau k_B T/m$ is the diffusion coefficient. The problem with such a perturbation approach is readily seen even in

the present case: After an appropriate rescaling in time and space, the mode's relaxation rate $\hat{\omega}(k)$, where k is the wave vector, is (a) unbounded as $k \to \infty$ in the first approximation, and (b) unstable for $k > 1$ in the second approximation (Fig. 6.1). Thus, even for the simplest kinetic equation (6.1),
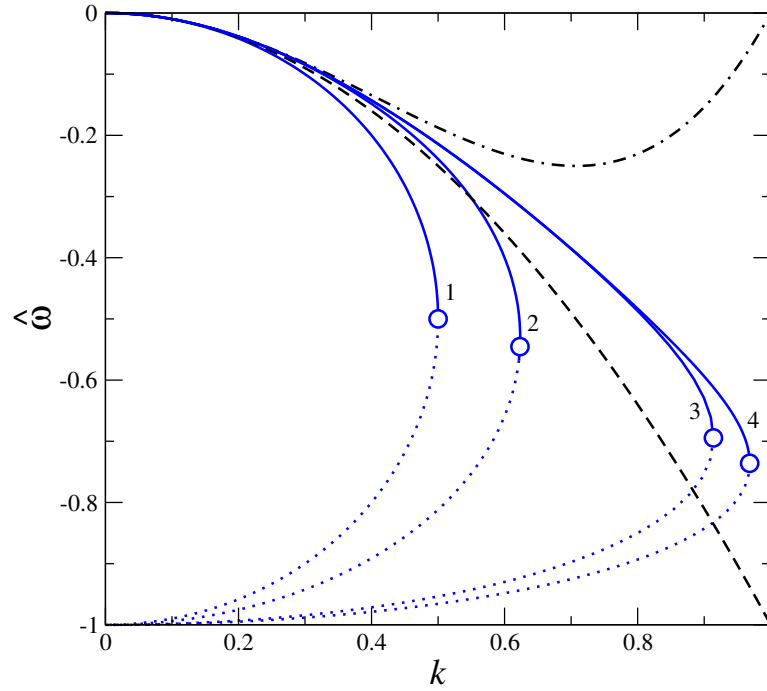
Figure 6.1: Hydrodynamic limit of Eq. (6.1). Dashed line: First CE approximation, $\hat{\omega}_{\mathrm{CE}}^{(2)} = -k^2$ (unbounded as $k \to \infty$); Dot-dashed line: Burnett-type approximation, $\hat{\omega}_{\mathrm{CE}}^{(4)} = -k^2 + k^4$ (unstable for $k > 1$); Solid and dotted Lines: Continuation by the sequence (6.30). Curves 1, 2, 3 and 4 correspond to the hydrodynamic branch $\hat{\omega}_{\mathrm{H}}^{(2n)}$ for $n = 1, 2, 20, 25$, respectively. Interception by a partner kinetic mode $\hat{\omega}_{\mathrm{P}}^{(2n)}$ (dots) at $k = k_{\mathrm{c}}^{(2n)}$ is indicated by open circles.

application of the perturbative CE expansion inherits the essential problems as in the case of the Boltzmann equation. Our goal here is to develop a non-perturbative method to study the hydrodynamic limit of (6.1).

In the sequel we set $k_B T/m = 1$, $\tau = 1$. Moments of the distribution functions can be written as

$$M_l(x, t) = \int_{-\infty}^{\infty} v^l f(v, x, t) dv. \tag{6.4}$$

Equation (6.1) is equivalent to an infinite-moment system,

$$\partial_t M_l = -\partial_x M_{l+1} - M_l + M_l^{\text{eq}}. \tag{6.5}$$

Instead of the infinite set of moments (6.4), it proves convenient to consider the generating function $Z(\lambda, x, t)$ (Fourier transform in the velocity variable),

$$Z = \int_{-\infty}^{\infty} e^{-i\lambda v} f(v, x, t) dv. \tag{6.6}$$

Let us denote $Z^{\pm}$ the real and imaginary parts of $Z = Z^+ + iZ^-$; Since moments (6.4) are real-valued, for even and odd moments we have, respectively,

$$M_{2n} = (-1)^n \left(\partial_\lambda^{2n} Z^+ \right)_{\lambda=0},$$
$$M_{2n+1} = (-1)^{n+1} \left(\partial_\lambda^{2n+1} Z^- \right)_{\lambda=0}.$$

In terms of the generating function, Eq. (6.1) is represented as a coupled system for Z^+ and Z^-,

$$\begin{aligned}
\partial_t Z^+ &= \partial_x \partial_\lambda Z^- - Z^+ + Z^{\text{eq}}, \\
\partial_t Z^- &= -\partial_x \partial_\lambda Z^+ - Z^-,
\end{aligned} \tag{6.7}$$

where $Z^{\text{eq}} = n(x, t)\varphi^{\text{eq}}$, and $\varphi^{\text{eq}} = e^{-\frac{\lambda^2}{2}}$. Finally, applying the Fourier transform in space, equations (6.7) become

$$\partial_t \hat{Z}^+ = ik\partial_\lambda \hat{Z}^- - \hat{Z}^+ + \hat{n}\varphi^{\text{eq}}, \tag{6.8}$$

$$\partial_t \hat{Z}^- = -ik\partial_\lambda \hat{Z}^+ - \hat{Z}^-, \tag{6.9}$$

where $\hat{Z}^\pm(\lambda, k, t) = \int_{-\infty}^{\infty} e^{-ikx} Z^\pm(\lambda, x, t)dx$ depend on the wave vector k.

Equations (6.8,6.9) are the starting point for the non-perturbative analysis. In the hydrodynamic limit, all moments depend on space and time only through their dependence on the locally-conserved field (density). To this end, the most general and yet unknown relation for the generating functions $\hat{Z}^\pm$ can be written as

$$\hat{Z}^+ = \hat{\Theta}^+(\lambda, k^2)\hat{n}(k, t), \tag{6.10}$$

$$\hat{Z}^- = ik\hat{\Theta}^-(\lambda, k^2)\hat{n}(k, t), \tag{6.11}$$

where $\hat{\Theta}^\pm$ are the functions in question, satisfying the consistency conditions, $\hat{\Theta}^+(0, k^2) = 1$, $\hat{\Theta}^-(0, k^2) = 0$. Knowing $\hat{\Theta}^-$, the balance equation becomes, $\partial_t \hat{n} = -k^2 \hat{G}\hat{n}$, where

$$\hat{G} = (\partial_\lambda \hat{\Theta}^-)_{\lambda=0}, \tag{6.12}$$

is the extended diffusion coefficient (EDC).

Let us now formulate the most general condition for $\hat{\Theta}^\pm$. The time-derivative of the generating function can be computed in two ways. On the

one hand, it is computed by chain rule and using the balance equation:

$$\partial_t^{\mathrm{macro}} \hat{Z}^+ = \frac{\partial \hat{Z}^+}{\partial \hat{n}} \partial_t \hat{n} = (-k^2 \hat{G} \hat{\Theta}^+) \hat{n}, \tag{6.13}$$

$$\partial_t^{\mathrm{macro}} \hat{Z}^- = \frac{\partial \hat{Z}^-}{\partial \hat{n}} \partial_t \hat{n} = ik(-k^2 \hat{G} \hat{\Theta}^-) \hat{n}. \tag{6.14}$$

This is the macroscopic time derivative, or the derivative of the yet unknown closed generating function due to the (also yet unknown) closed balance equation. On the other hand, the microscopic time derivative is given by the right hand side of (6.8,6.9):

$$\partial_t^{\mathrm{micro}} \hat{Z}^+ = (-k^2 \partial_\lambda \hat{\Theta}^- - \hat{\Theta}^+ + \varphi^{\mathrm{eq}}) \hat{n}, \tag{6.15}$$

$$\partial_t^{\mathrm{micro}} \hat{Z}^- = ik(-\partial_\lambda \hat{\Theta}^+ - \hat{\Theta}^-) \hat{n}. \tag{6.16}$$

The dynamic invariance condition [56] requires that the micro- and the macroscopic derivatives of the generating function should give the same result, independently of $\hat{n}$:

$$\partial_t^{\mathrm{micro}} \hat{Z}^\pm = \partial_t^{\mathrm{macro}} \hat{Z}^\pm. \tag{6.17}$$

Thus, the invariance condition for the generating function is a system of two first-order equations,

$$-k^2 \hat{G} \hat{\Theta}^+ + k^2 \partial_\lambda \hat{\Theta}^- + \hat{\Theta}^+ - \varphi^{\mathrm{eq}} = 0, \tag{6.18}$$

$$-k^2 \hat{G} \hat{\Theta}^- + \partial_\lambda \hat{\Theta}^+ + \hat{\Theta}^- = 0, \tag{6.19}$$

subject to the initial conditions, $\hat{\Theta}^+(0, k^2) = 1$, $\hat{\Theta}^-(0, k^2) = 0$. It can be readily checked that the invariance equation generates the CE solution when functions $\hat{\Theta}^\pm$ are expanded into Taylor series around $k^2 = 0$. Our goal is, however, to solve the invariance equation avoiding any expansion of this kind. We proceed with a few transformations: (i) Differentiate (6.18) with respect to λ and eliminate $\partial_\lambda \hat{\Theta}^+$ to get the second-order equation for $\hat{\Theta}^-$:

$$k^2 \partial_\lambda^2 \hat{\Theta}^- - (1 - k^2 \hat{G})^2 \hat{\Theta}^- - \partial_\lambda \varphi^{\mathrm{eq}} = 0; \qquad (6.20)$$

(ii) Differentiate equation (6.20) one more time; use transformed variable, $\partial_\lambda \hat{\Theta}^- = \hat{\Sigma} e^{-\lambda^2/2}$, and note that $\hat{G} = (\hat{\Sigma})_{\lambda=0}$. Thus, the invariance equation for the generating function becomes,

$$(k^2 \hat{G} - 1)^2 \hat{\Sigma} + (1 - \lambda^2)(k^2 \hat{\Sigma} - 1) = k^2 (\partial_\lambda^2 \hat{\Sigma} - 2\lambda \partial_\lambda \hat{\Sigma}). \qquad (6.21)$$

The invariance equation (6.21) is crucial. We note that, although not form-identical, equation (6.21) can be regarded as an analog of the basic equation of the non-perturbative approach in quantum field theories, the Schwinger-Dyson equation (SDE) [185, 186]. Indeed, SDE is a relationship between the one-particle Green's function $\hat{G}$ and the mass operator $\hat{\Sigma}$. Standard derivation of SDE proceeds along the lines similar to the above, considering the generating function of many-particle Green's functions. In the present context, the "mass operator" $\hat{\Sigma}$ in (6.21) provides the coupling to all higher-order moments, and self-consistently defines the EDC $\hat{G}$. For the present analysis of (6.21), it is convenient to introduce the frequency function $\hat{\Omega} =$

$-k^2\hat{\Sigma}$, so that $\hat{\omega} = -k^2\hat{G} = (\hat{\Omega})_{\lambda=0}$:

$$(\hat{\omega} + 1)^2\hat{\Omega} + k^2(1 - \lambda^2)(\hat{\Omega} + 1) = k^2(\partial_\lambda^2\hat{\Omega} - 2\lambda\partial_\lambda\hat{\Omega}). \qquad (6.22)$$

Solution to the ODE (6.22) with the initial conditions, $(\hat{\Omega})_{\lambda=0} = \hat{\omega}$, $(\partial_\lambda\hat{\Omega})_{\lambda=0} = 0$, is found in closed form,

$$\hat{\Omega} = (\hat{\omega} + 1)e^{\frac{\lambda^2}{2}}\cosh(\lambda\beta) - 1 +$$
$$\frac{\sqrt{2\pi}}{4}\beta e^{\frac{\lambda^2+\beta^2}{2}}\left[2\cosh(\lambda\beta)\mathrm{erf}\left(\frac{\beta}{\sqrt{2}}\right) + e^{-\lambda\beta}\mathrm{erf}\left(\frac{\lambda-\beta}{\sqrt{2}}\right) - e^{\lambda\beta}\mathrm{erf}\left(\frac{\lambda+\beta}{\sqrt{2}}\right)\right],$$
$$(6.23)$$

where $\beta = \sqrt{(\hat{\omega} + 1)^2/k^2}$, and erf is the error function. The function $\hat{\Omega}(\lambda, \hat{\omega}, k^2)$ (6.23) describes all invariant manifolds of the kinetic equation: for every fixed k, it is a parametric set of functions (of λ) parameterized by the frequency $\hat{\omega}$. The *hydrodynamic manifold* is generated by a specific dependence $\hat{\omega}_{\mathrm{H}}(k)$ which continues the corresponding solution at $k = 0$ to $k > 0$. We note that the condition $(\hat{\Omega})_{\lambda=0} = \hat{\omega}$ results in the identity, $\hat{\omega} = \hat{\omega}$, rather than in an equation for $\hat{\omega}_{\mathrm{H}}$. Therefore, a special procedure is needed for deriving the function $\hat{\omega}_{\mathrm{H}}$. As we shall see below, the analyticity of $\hat{\Omega}$ implies that the hydrodynamic manifold indeed extends to $k > 0$.

It is instructive to write the solution (6.23) in terms of a series,

$$\hat{\Omega} = \hat{\omega} + \sum_{n=1}^{\infty}\frac{\lambda^{2n}\hat{\omega}_{2n}(\hat{\omega}, k^2)}{(2n)!(k^{2n})}, \qquad (6.24)$$

where the coefficients $\hat{\omega}_{2n}$ have the following form:

$$\hat{\omega}_{2n} = (\hat{\omega} + 1)[\hat{\omega}(\hat{\omega} + 1)^{2n-1} + (2n - 1)!!(k^{2n}) + \hat{p}_{2n}]. \tag{6.25}$$

Here $\hat{p}_{2n}(\hat{\omega}, k^2)$ is a polynomial in $\hat{\omega}$ and k^2 of the order $k^{2(n-1)}$, and $(2n - 1)!! = 1 \cdot 3 \cdot 5 \ldots (2n-1)$. The first few coefficients have the following explicit form:

$$\hat{\omega}_2 = (\hat{\omega} + 1)[\hat{\omega}(\hat{\omega} + 1) + k^2],$$

$$\hat{\omega}_4 = (\hat{\omega} + 1)[\hat{\omega}(\hat{\omega} + 1)^3 + 3k^4 + k^2(\hat{\omega} + 1)(1 + 6\hat{\omega})].$$

We note in passing that the coefficients $\hat{\omega}_{2n}$ (6.25) can be derived directly from the invariance equation (6.22), without solving it explicitly. Accordingly, the continuation procedure described below can also be used in other cases where analytic solutions to the corresponding invariance equations are difficult to obtain. Coefficients (6.25) imply the two limits:

$$\hat{\omega}_{2n} \to \hat{\omega}(\hat{\omega} + 1)^{2n}, \ k \to 0, \tag{6.26}$$

$$\hat{\omega}_{2n} \to (\hat{\omega} + 1)(2n - 1)!!(k^{2n}), \ k \to \infty. \tag{6.27}$$

Consequently, we have, at $k \to 0$:

$$\hat{\Omega}_0 \sim \hat{\omega} \cosh[\lambda(\hat{\omega} + 1)/k]. \tag{6.28}$$

Requirement of finiteness of the above expression at $k = 0$ selects two values

for ω: $\hat{\omega}_H = 0$, and $\hat{\omega}_K = -1$. The former is the seed of the hydrodynamic branch, while the latter is the (infinitely degenerated) eigenvalue of the relaxation term of (6.1). On the other hand, in the opposite limit $k \to \infty$ (6.27), the function $\hat{\Omega}$ remains analytic,

$$\hat{\Omega}_\infty = \lim_{k\to\infty} \hat{\Omega} = (1 + \hat{\omega})e^{\lambda^2/2} - 1. \tag{6.29}$$

Now, since at any $k \neq 0$ function (6.23) is an analytic function of λ, the series (6.23) is convergent; hence, $\hat{\omega}_{2n}(\hat{\omega}, k^2)/((2n)!k^{2n}) \to 0$ as $n \to \infty$. This observation implies the following practical recipe for the continuation for finite k: Let us consider a sequence of algebraic equations,

$$\hat{\omega}_{2n}(\hat{\omega}, k^2) = 0, \ n = 1, \ 2, \ \ldots \tag{6.30}$$

At $k = 0$, for every n, equation (6.30) seeds one (hydrodynamic) branch at $\hat{\omega}_H = 0$ and $2n$ degenerated kinetic branches at $\hat{\omega}_K = -1$. The solution $\hat{\omega}_H^{(2n)}(k)$ with the asymptotics $\hat{\omega}_H^{(2n)}(0) = 0$ is the extension of the hydrodynamic branch at the nth order of the said procedure. In other words, instead of the CE expansion in terms of k^2 we consider a sequence of finite-dimensional algebraic problems of increasing order (6.30) based on the convergence of the series (6.24). We term this a *pullout* procedure for the reason clarified in Fig. 6.1: At each step n, the hydrodynamic branch $\hat{\omega}_H^{(2n)}$ is pulled out till the critical value $k_c^{(2n)}$. At $k_c^{(2n)}$, the hydrodynamic branch is intercepted by one of the kinetic branches (partner kinetic mode $\hat{\omega}_P^{(2n)}$ with the asymptotics, $\hat{\omega}_P^{(2n)} \to -1$ as $k \to 0$). After the intercep-

tion, the pair of real-valued solutions $\{\hat{\omega}_{\mathrm{H}}^{(2n)}, \hat{\omega}_{\mathrm{P}}^{(2n)}\}$ continue as the pair of complex-conjugate roots of (6.30). This effect of interception is well known from previous exact summations of the CE expansion of the diffusion-type modes for finite-moment systems [56]. The pullout procedure thus furnishes a non-perturbative extension of the hydrodynamics with monotonically increasing accuracy for finite k. At any step of the procedure (6.30) the result is bounded, and the interception point $k_{\mathrm{c}}^{(2n)}$ increases monotonically. In table 6.1, the matching of the polynomial expansion to order k^{14} for the sequence of pullouts $\hat{\omega}_{\mathrm{H}}^{(2n)}$ is verified against the CE expansion.

	a_2	a_4	a_6	a_8	a_{10}	a_{12}	a_{14}
$\hat{\omega}_{\mathrm{H}}^{(2)}$	-1	-1	-2	-5	-14	-42	-132
$\hat{\omega}_{\mathrm{H}}^{(4)}$	-1	1	-4	3	16	-122	312
$\hat{\omega}_{\mathrm{H}}^{(6)}$	-1	1	-4	27	-248	2110	-17352
$\hat{\omega}_{\mathrm{H}}^{(8)}$	-1	1	-4	27	-248	2830	-38232
$\hat{\omega}_{\mathrm{CE}}$	-1	1	-4	27	-248	2830	-38232

Table 6.1: Expansion of the hydrodynamic mode $\hat{\omega}_{\mathrm{H}} = \sum_{n=1}^{\infty} a_{2n} k^{2n}$ by the sequence (6.30). Coefficients in boxes match the CE expansion $\hat{\omega}_{\mathrm{CE}}$.

However, the present procedure demonstrates a much better and controlled convergence. It is evident from Fig. 6.1 that the hydrodynamic branch is pulled out smoothly so that the result of the highest order of approximation shown in Fig. 6.1 can be regarded exact up to $k \approx 0.8$.

Using the data of Fig. 6.1, in Fig. 6.2 we present the deviation of the CE expansion at various orders of approximation in terms of k^2. While the CE expansion indeed systematically improves the accuracy at very small k, this comes at a price of increased deviation at larger k. By contrast, the
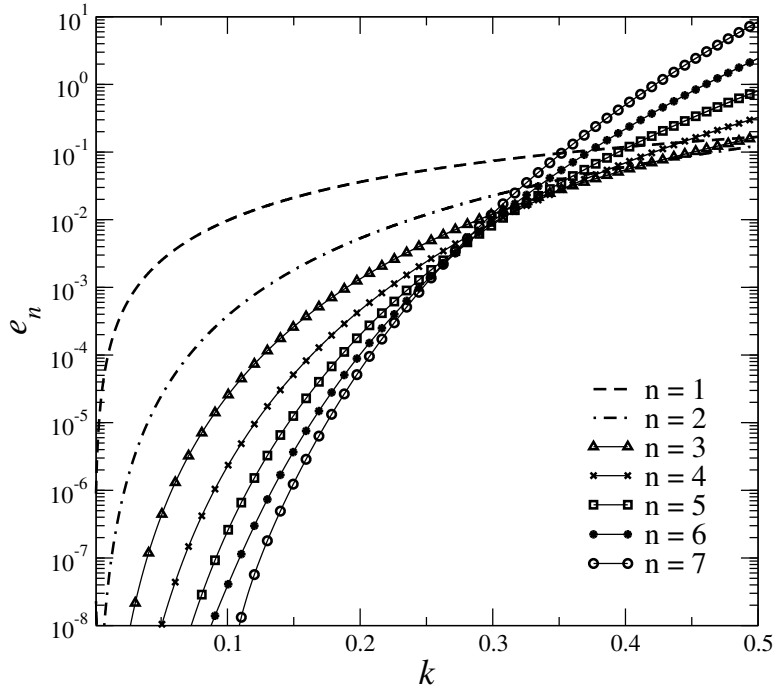
Figure 6.2: Deviation of the CE approximations $\hat{\omega}_{\text{CE}}^{(2n)}$ for $n = 1, \ldots, 7$ from the exact solution, $e_n = \left| (\hat{\omega}_{\text{H}}^{(50)} - \hat{\omega}_{\text{CE}}^{(2n)})/\hat{\omega}_{\text{H}}^{(50)} \right|$.

pullout procedure is, in fact, a non-perturbative (that is, a non-polynomial in k) method which approximates the infinite-dimensional problem (the infinite moment system) with a sequence of finite-dimensional problems (6.30) of increasing order; at each step the available piece of the hydrodynamic manifold is bounded and well controlled.

6.3 Conclusion

We conclude this chapter with a discussion. Above, we have considered the kinetic equation (6.1) the conventional hydrodynamic limit of which is considered to be the diffusion equation, while its standard perturbative

analysis inherits the main problems. We have derived the invariance equation, as the analog of the Schwinger-Dyson equation in the present context. The exact solution to the invariance equation found above is, to the best of our knowledge, the first of its kind for infinite-dimensional kinetic systems. Based on the analyticity of the exact solution we have introduced a new procedure of continuation of the hydrodynamic mode and have shown its consistency with the standard Chapman-Enskog expansion. The change of the perspective on the derivation of hydrodynamics, by switching from a perturbative gradient expansion (expansion in terms of wave vector k) to a sequence of finite-order, non-perturbative in gradients problems keeps the extension of the hydrodynamics under control. Another connection to the SDE was mentioned in [187, 188] in the context of lattice Boltzmann simulation of turbulent flows. Findings of this work lay out the way to study the reduced description for other systems. In particular, related linearized kinetic models such as the Bhatnagar-Gross-Krook kinetic equations can be considered straightforwardly along the above lines, also in three dimensions since the general tensorial structure of the generating function is known in that case [56]. For the linearized Boltzmann equation, the resulting invariance equation contains then the linearized Boltzmann operator, and the pullout procedure will amount to solving linear integral equations of familiar type [54]. Finally, for the non-linear case, approximate hydrodynamic manifolds arising in the pullout procedure can be obtained along the lines of non-linear finite-moment systems [56].

Chapter 7

Conclusions and future work

7.1 Summary

The aim of this dissertation was to further explore existing approaches and propose new ones for the construction of reduced models of chemical and physical kinetics. The reduced models include low-dimensional manifolds and skeletal mechanisms for combustion of typical fuels and the hydrodynamic manifold of the Boltzmann equation. The application of reduced models shows a reduction in computational cost by reduction of the size of the system and by attenuation of the stiffness of the governing equations. Constructing low-dimensional models can also help in understanding the hierarchical interaction between macroscopic and microscopic dynamics of relaxation of kinetic systems.

First, we fostered the use of the classical approach: constructing a low-dimensional manifold for a system of ODEs enjoying disparity in timescales (chapters 2 and 3). This approach is well studied in the dynamical systems literature and slow invariant manifolds have been proposed as low-order

157

models mimicking the original dynamics of the system. In the combustion community, historically the approach has been used for chemical kinetics involving small number of species and reactions. During the early 90s, timescale-based methods such as Computational Singular Perturbation (CSP) and Intrinsic Low Dimensional Manifold (ILDM) successfully constructed low-dimensional manifolds for more complex chemical networks for hydrogen/air and syngas/air combustion.

Other approaches like the Method of Invariant Grid (MIG) are based on the refinement of an initial guess towards the Slow Invariant Manifold (SIM). In chapter 2, MIG was employed with the refinement process being controlled by successive relaxation and redistribution of the grid. The method was applied on the hydrogen/air detailed mechanism involving 9 species participating in 21 elementary reactions. Two- and three-dimensional slow manifolds were constructed using a Rate-Controlled Constrained Equilibrium (RCCE) manifold as the initial guess and the accuracy were compared with the detailed model in autoignition and planar premixed flame simulations.

Relaxation towards the equilibrium can be explained through the concept of entropy. Hence, methods such as the quasi-equilibrium manifold have been proposed for the construction of low dimensional manifolds. The union of states in the phase space where the entropy is constrained due to slow varying processes. The better the choice of the constraints, the better is the approximation of the low-dimensional description. In chapter 3, we have imposed constraints on the mole numbers based on the slow left eigen-

vectors at equilibrium. Spectral Quasi-Equilibrium Manifolds (SQEMs) found from this method of different dimensions can be readily constructed and manifolds of up to seven dimensions were constructed and validated for methane/air combustion. The RCCE manifold is a well-known Quasi-Equilibrium Manifold (QEM) where the choice of the minimal number of constraints requires information about the class of fast/slow reactions in the detailed kinetic description.

Some of the features of the aforementioned approaches can be summarized as follows:

- *How can we construct low-dimensional manifolds for a system of ODEs?*

  The global Relaxation Redistribution Method (gRRM) in chapter 2 offers an approach to answer this question. The spectral quasi equilibrium manifold proposed in Chapter 3 offers another approach for manifold construction. The benefits of SQEM are (i) the construction is localized in phase space, and (ii) high-dimensional manifolds can be constructed. The drawbacks are (i) the entropy function of the underlying dynamical system should be known, (ii) the convex optimization problem may not straightforward to solve b the available optimization numerical packages (iii) the SQEM inherently is not invariant by construction.

- *How much of a phase space can be covered by the slow manifolds?*

  The equilibrium point is a zero-dimensional slow manifold and the

dimension of the SIM increases as we move away from it. There is no general recipe to answer how large the SIM of a fixed dimension should be at a certain point in phase space. Usually, the relaxation of chemical kinetics includes generating and exhausting fast and slow modes, resulting in changes in the spectral gap and the dynamics evolves in a nested hierarchy of slow manifolds. If the low-dimensional slow manifolds are constructed near equilibrium, an approximation should be made for the states farther away. In chapter 2 the initial grid was constructed based on the RCCE method which is well known in combustion. The relaxation and redistribution is then applied and the converged solution is (i) the SIM of the system with the same dimension as for the RCCE manifold, and (ii) a proper extension of the slow manifold to cover the rest of the admissible space.

- *What are the difficulties of constructing and using the slow manifolds in chemical kinetics?*

First, the construction by itself can be problematic. The structure of the slow manifold can be complex, involving foldings or discontinuities. SQEM and RCCE are thermodynamic manifolds which are known to be "good" manifolds in the sense that they are not folded, multivalued, discontinuous, non-realizable or non-smooth [18]. By forcing the gRRM manifold to pass through the fixed boundaries of the RCCE manifold the author argues that in the absence of ill-behavior in the dynamics itself (e.g. non-smooth systems), the converged manifold is also good.

Second, the computed slow manifolds are usually stored as tables for use in simulations. Tables with a large number of parameterizing variables require efficient ways for storage and retrieval of information and accurate interpolation. In order to avoid these complexities it is recommended to construct up to three-dimensional manifolds. As shown in chapter 3 for methane, the phase space is 27-dimensional and for capturing the autoignition delay one should have at least a six-dimensional manifold. Imposing a restriction on the dimension of the slow manifold can lead to poor quality reduced models. It should be mentioned that in chemical kinetics and specifically for autoignition, neglecting the fast processes can cause significant error in the ignition delay times using the reduced description. The author would like to comment that low-dimensional slow manifolds are restricted to relatively small skeletal mechanisms such as hydrogen combustion presented in chapter 2. However, the discussion about the geometrical picture of relaxation of combustion systems near equilibrium is still valuable.

Third, the parameterization of the manifold is also crucial. In the general case, the parameterizing variables are linear combinations of the original variables. In the RCCE method linear combinations of species mole number is used as the slow varying variable, and the coefficients are deduced from chemical knowledge of the reaction network. In the SQEM method, we proposed a general way to find these coefficients, by assuming that the slow left eigenvectors at equilibrium dictate the

constraints on the mole numbers. There are more advanced methods to find the slow intrinsic variables from data, which can be linear or nonlinear functions of the original variables (e.g. [189,190]). However, implementing the new system of variables in multi-dimensional reactive flow solvers needs significant case-specific changes in numerical codes, and additional assumptions (such as assumptions on diffusion coefficients to simplify the governing equations).

Finally, if the initial state does not lie on the manifold, the state should be projected on the manifolds. Projection by itself can lead to changes in the temporal evolution of the system, specially in autoignition problems where a small amount of radicals can alter the behavior dramatically. It is common in the combustion literature to perform the integration in time starting from the state on the manifold to show the quality of SIM and to eliminate the error of projection. In addition, in the presence of diffusion terms, the states leave the manifolds and need to be projected back on the manifold.

Chapter 4 of this thesis proposed a novel and very simple method to identify the redundant reactions/species in detailed reactions. The most-contributing elementary reactions to the total entropy production are selected, and species participating in those reactions are recognized as important. The method was applied on a high-dimensional system of n-heptane/air mechanism including 561 species and 2539 elementary reactions. Among all the skeletal mechanisms found by different threshold values, two with 203 species (R203) and 161 species (R161) are selected. The skeletal

mechanisms show excellent agreement with detailed kinetics in the adiabatic constant pressure autoignition, the single-zone engine model and the planar premixed flame in a wide range of the thermodynamic and the mixture conditions. The reduction in size (71% in R161 case) and stiffness are encouraging.

By careful inspection in R161 skeletal mechanism we found some of the species have zero production rate due to elimination of unimportant reactions. Therefore, we reduce the size of R161 to 149 species (R149). In chapter 5, we examined the fidelity of the R149 mechanism in the PSR setup where complex dynamics can be observed. The arc-length continuation method was used to construct one- and two-parameter bifurcation diagrams. The continuation in residence time shows a typical "S-curve" diagram with one extra branch for the cool-flame behavior of the fuel. Four turning and one Hopf bifurcation points are found for an adiabatic PSR operating at $T_0 = 650$ K $\varphi = 1$, $p = 1$, 5 and 20 atm. The comparison between D561 and R149 shows that the bifurcation points are well captured and R149 can be used for detailed analysis of the complex dynamics. The one-parameter continuation with respect to equivalence ratio and heat losses shows different features in bifurcation diagrams, including isolas, cool- and strong-flame oscillation and possible global bifurcations. Due to the lower complexity of the skeletal mechanism, continuation in two parameters could also be carried out, showing cusp, Bogdanov-Takens and double Hopf bifurcations. To the best of the author's knowledge, continuation in such a large-scale dynamical system has not been addressed in the combus-

tion kinetics literature before, and some of the complex dynamics have been shown for the first time for heavy hydrocarbons. In addition to dynamical system analysis, the interesting points in bifurcation diagrams are investigated from the kinetic point of view to identify the reactions leading to the observed behavior. The diagnostic tools introduced by the Computational Singular Perturbation method were used to identify the contribution of elementary reactions and flow in ignition, extinction and oscillation of the flame.

Chapter 6 is dedicated to a classical problem in physical kinetics: the hydrodynamic limit of the Boltzmann equation. The classical approach to study the problem is a perturbation-based method (Chapman-Enskog) for which the expansion is unstable. Non-perturbative analytical techniques were used for the derivation of the hydrodynamic manifolds from the kinetic equations. The new approach is analogous to the Schwinger-Dyson equation of quantum field theories, and its derivation is demonstrated by the construction of the exact diffusion manifold for a model kinetic equation.

7.2   Directions for future work

Suggestions for further research along the work presented in this thesis are summarized below:

- Application of the entropy production analysis to construct the skeletal mechanisms for practical fuels:

   The entropy production analysis which was introduced in chapter 4 is

straightforward and easy to implement for constructing skeletal mechanism for complex fuels. For example, the detailed chemical kinetic reaction mechanisms of Westbrook et. al. for n-alkanes larger than n-heptane includes $n_s = 2115$ species and $n_r = 8157$ reactions [7]. The entropy production analysis was performed on the isenthalpic, isobaric autoignition of n-decane (n-$C_{10}H_{22}$) for a specific condition ($\varphi = 1$, $T_0 = 700$ K and $p = 20$ atm). The skeletal mechanism involves only $n_s = 281$ species and $n_r = 995$ reactions, and the comparison of the evolution of the temperature shows excellent agreement between the detailed and skeletal mechanisms (see Fig. 7.1). Both simulations were carried out for $t = 0.012$ s of autoignition problem on a single 2.7 GHz processor, showing that the skeletal mechanism is approximately 387 times faster than the comprehensive one (84 minutes for the detailed versus 13 seconds for the skeletal mechanism using the same stiff integrator).

- Further reduction of the skeletal mechanisms:

  Although the reduction in the number of species and stiffness is promising using the entropy production analysis, for heavy hydrocarbons the size of the skeletal mechanism is still large and multi-dimensional simulations are practically impossible. The size of the skeletal mechanism can be reduced further by using more complex methods for eliminating or lumping species. The CSP code which was developed (chapter 5) can be used to generate possible smaller skeletal mechanisms or to identify the QSS species.
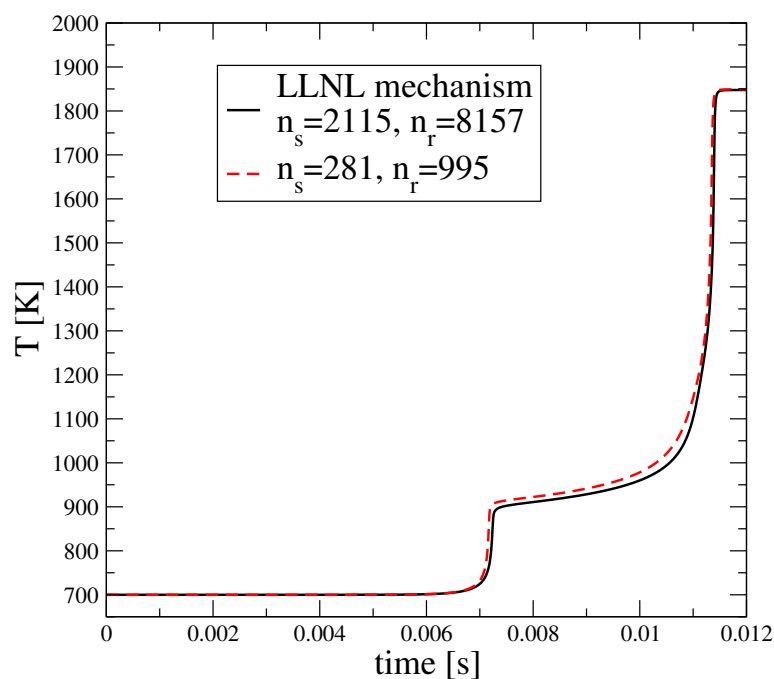
Figure 7.1: Comparison between the time evolution of the temperature deduced from comprehensive mechanism (solid line) and the skeletal mechanism (dashed line) for n-decane autoignition ($p = 20$ atm, $T_0 = 700$ K and $\varphi = 1$).

- Can the concept of SIM be used in a different way?

  The geometry of relaxation in chemical kinetics problems is an interesting topic, but as discussed the application of tabulated manifolds in multi-dimensional simulations is limited. One can think how to extract useful information about the physics of the reactive flow simulation from slow and fast variables. The author want to comment that, if the SIM of the system is known, maybe one can find the approach to construct skeletal or few-steps global mechanism which mimics the dynamics of the slow manifold

  In addition, there are different methods in dynamical system literature

for constructing the SIM which can be introduced for the combustion community.

- Direct Numerical Simulations using skeletal mechanisms

The stability of hydrocarbon laminar/turbulent premixed flames is the subject of ongoing studies. The low-Mach number solver based on the spectral element code NEK5000 [191] was used to study hydrodynamic and thermodiffusive instabilities of laminar planar premixed hydrogen flames (e.g. [192, 193]). In order to study instabilities of methane flames under laminar and turbulent conditions, the entropy production analysis was performed on a database generated from the laminar planar premixed methane-air flame for $T_0 = 300$ K, $p = 1$ atm and $\varphi = 0.9$. The detailed methane mechanism (excluding nitrogen chemistry) consists of $n_s = 35$ species and $n_r = 217$ reactions (D35) [5]. The skeletal mechanism (R20) includes $n_s = 20$ species and $n_r = 98$ reactions, and the laminar flame speed S_L and flame thickness δ_f errors compared to the detailed one are less than 2% (see table 7.1).

Table 7.1: methane/air premixed flame simulation

Mechanism	S_L (cm/s)	δ_f (cm)
D35	33.472	0.046539
R20	33.114	0.047524

The temperature and selected species profiles deduced from the D35 and R20 mechanisms are compared in the Fig. 7.2, showing very good agreement.
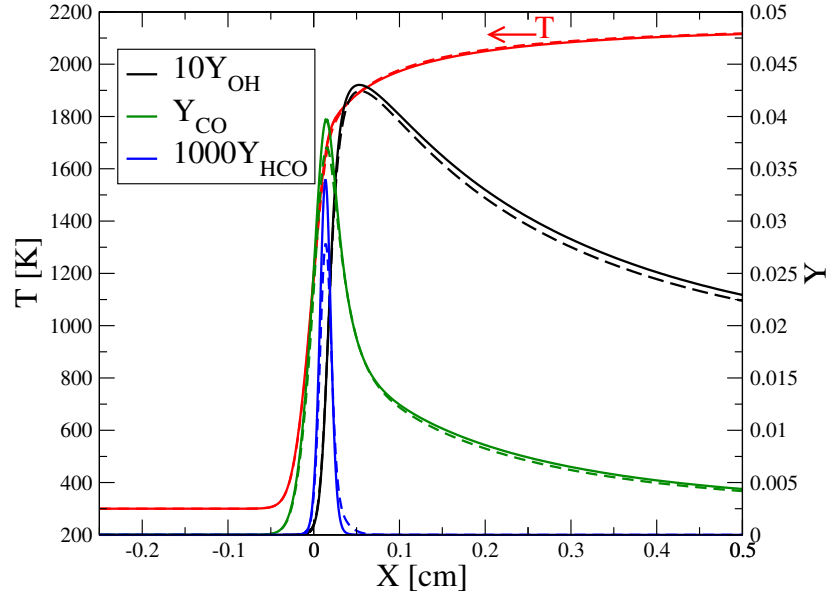
Figure 7.2: Comparison between the flame structure deduced from the comprehensive mechanism (solid lines) and the skeletal mechanism (dashed lines) for methane one-dimensional planar premixed flame ($p = 1$ atm, $T_0 = 300$ K and $\varphi = 0.9$).

Some direct numerical simulations of two-dimensional channel-like domain (see Fig. 7.3) have been performed aiming at comparing the results of the detailed and the skeletal mechanisms in a multi-dimensional setup. The variables are nondimensionalized using $T_{ref} = 300$ K, $x_{ref} = \delta_f$ and $t_{ref} = \delta_f/S_L$ for the reference temperature, length scale and time. The planar front was perturbed into a sinusoidal shape $\Delta = 0.1 sin(\pi y/h)$. Around the flame, uniform quadrilateral elements with $\delta_x = \delta_y = 0.5\delta_f$ and 8th-order polynomial in each direction were used so that the flame thickness is resolved with 17 grid points.

A single-cusp flame structure forms which propagates towards the inflow. The time history of the non-dimensional heat release rate
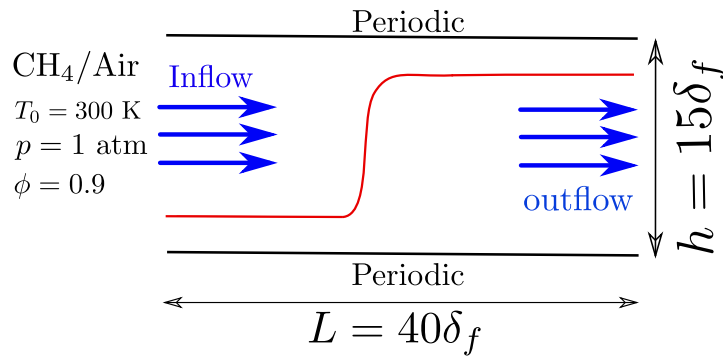
Figure 7.3: Schematic of two-dimensional planar premixed flame setup and boundary conditions
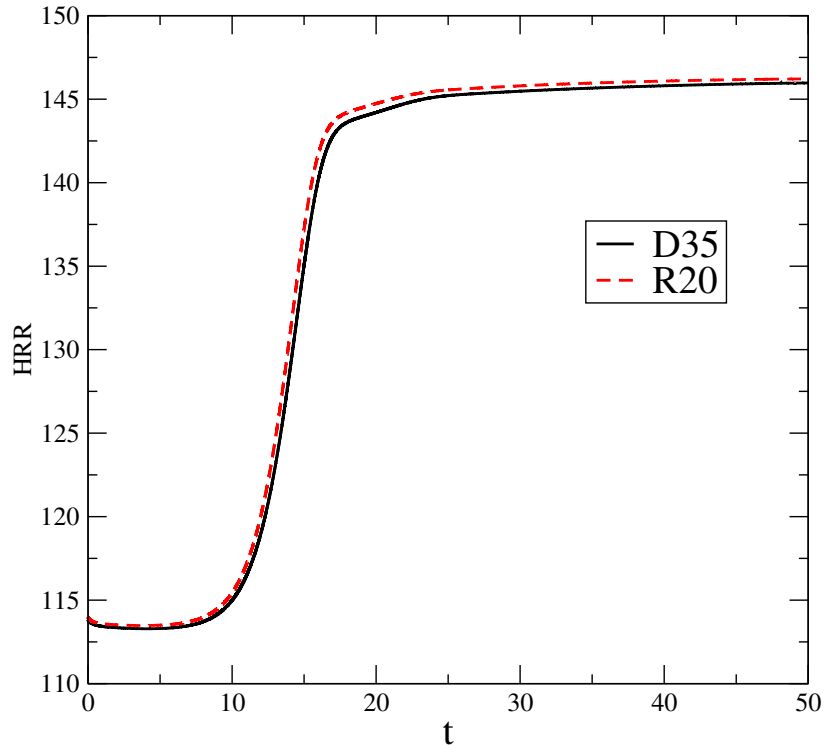
Figure 7.4: Temporal evolution of the heat release rate (HRR) for detailed (D35) and the skeletal mechanism (R20)

(HRR) (Fig. 7.4) and isocontours of the temperature for different times (Fig. 7.5), computed using the detailed and skeletal mechanisms are compared, showing very good agreement. The computational time

using the skeletal mechanism is three times lower, enabling parametric
studies and extension to three-dimensional turbulent conditions.
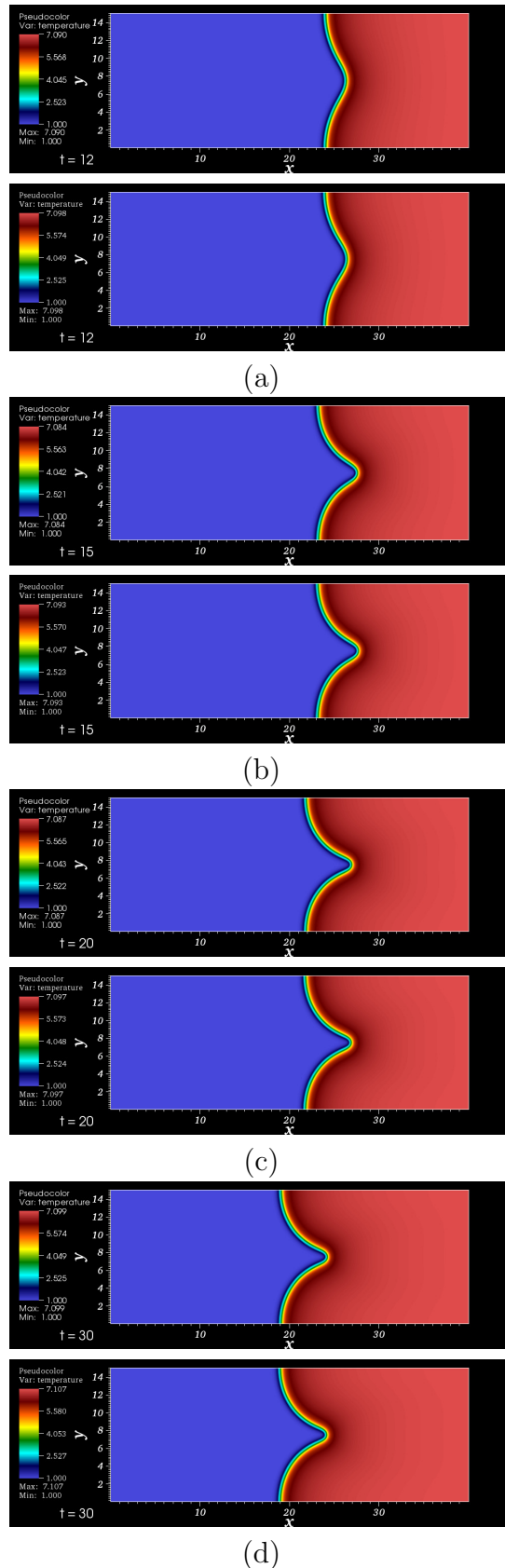
Figure 7.5: Temperature isocontours of the methane-air flame propagating in the 2D domain at (a) $t = 12$, (b) $t = 15$, (c) $t = 20$, and (d) $t = 30$. Upper and lower rows are deduced from the detailed and the skeletal mechanism respectively.

Appendix A

Code segment for the entropy production analysis

A database 'samples.dat' is generated by the constant enthalpy and pressure batch reactor solution, using the detailed mechanism initial conditions covering the range of interest. Pressure, p, temperature, T and mass fraction of all species Y, are stored row-wise in the file 'sample.dat'. KK and II are the number of species and reactions, respectively, and ICWRK and RCWRK the integer and real CHEMKIN work arrays. The stoichiometric matrix is stored in NUKI, forward and reverse reaction rates in the FWDK and REVK arrays, while the relative contribution of reactions to the total entropy production DSDT is stored in DSDTK. If its contribution is larger than the threshold, CUTOFF, the reaction is flagged in the array REINDX. Species participating in important reactions are flagged in array SPINDX. A slightly modified version of MECHMOD 3.42 [133] was used to generate the skeletal mechanisms by eliminating unimportant species from the detailed scheme.

```
1 OPEN(unit=10,file='samples.dat',form='formatted')

2 100 CONTINUE

3     READ (UNIT=10, FMT=* ,END=200)P,T,(Y(K),K=1,KK)

4     CALL CKYTX(Y,ICKWRK,RCKWRK,X)

5     CALL CKKFKR (P,T,X,ICKWRK,RCKWRK,FWDK,REVK)

6     DO K = 1,II

7        DSDTK(K) = 0.0d0

8     ENDDO

9     DSDT = 0.d0

10    DO K = 1,II

11       IF (FWDK(K).LE.0.0d0) FWDK(K) = 1.0D-50

12       IF (REVK(K).LE.0.0d0) REVK(K) = 1.0D-50

13       DSDTK(K) = RU*(FWDK(K)-REVK(K))*(log((FWDK(K)/REVK(K))))

14       DSDT     = DSDT + DSDTK(K)

15    ENDDO

16    DO K=1,II

17       IF ((DSDTK(K)/DSDT).gt.CUTOFF) ENT_IDX(K)=1

18    ENDDO

19        GO TO 100

20 200 CONTINUE

21    J = 0

22    DO K = 1, II

23       IF (ENT_IDX(K).eq.1) THEN

24          J = J + 1

25          REINDX(J)=K
```

```
26      ENDIF

27   ENDDO

28   CALL CKNU(KK, ICKWRK, RCKWRK, NUKI)

29   DO I = 1,KK

30      SPINDX(I)=0

31   ENDDO

32

33   DO K = 1, SIZEINDX

34      J = REINDX(K)

35      DO I =1, KK

36         IF (NUKI(I,J).ne.0) THEN

37            SPINDX(I)=1

38         ENDIF

39      ENDDO

40   ENDDO
```

Bibliography

[1] U. E. I. Administration, "Annual Energy Outlook 2014," *DOE/EIA*, vol. 0383, pp. 1–269, 2014.

[2] F. Williams, *Combustion theory: the fundamental theory of chemically reacting flow systems*, vol. 54. Perseus Books, 1985.

[3] Z. Qin, V. V. Lissianski, H. Yang, W. C. Gardiner, S. G. Davis, and H. Wang, "Combustion chemistry of propane: A case study of detailed reaction mechanism optimization," *Proc. Combust. Inst.*, vol. 28, no. 2, pp. 1663–1669, 2000.

[4] H. J. Curran, P. Gaffuri, W. J. Pitz, and C. K. Westbrook, "A comprehensive modeling study of n-heptane oxidation," *Combust. Flame*, vol. 114, no. 1-2, pp. 149–177, 1998.

[5] G. P. Smith, D. M. Golden, M. Frenklach, N. W. Moriarty, B. Eiteneer, D. M. Golden, C. T. Bowman, R. K. Hanson, S. Song, W. C. Gardiner, V. V. Lissianski, and Z. Qin, "GRI-Mech 3.0."

[6] P. Gokulakrishnan, C. C. Fuller, M. S. Klassen, R. G. Joklik, Y. N. Kochar, S. N. Vaden, T. C. Lieuwen, and J. M. Seitzman, "Experiments and modeling of propane combustion with vitiation," *Combust. Flame*, vol. 161, no. 8, pp. 2038–2053, 2014.

[7] C. K. Westbrook, W. J. Pitz, O. Herbinet, H. J. Curran, and E. J. Silke, "A comprehensive detailed chemical kinetic reaction mechanism for combustion of n-alkane hydrocarbons from n-octane to n-hexadecane," *Combust. Flame*, vol. 156, no. 1, pp. 181–199, 2009.

[8]   S. M. Sarathy, C. K. Westbrook, M. Mehl, W. J. Pitz, C. Togbe, P. Dagaut, H. Wang, M. a. Oehlschlaeger, U. Niemann, K. Seshadri, P. S. Veloo, C. Ji, F. N. Egolfopoulos, and T. Lu, "Comprehensive chemical kinetic modeling of the oxidation of 2-methylalkanes from C7 to C20," *Combust. Flame*, vol. 158, no. 12, pp. 2338–2357, 2011.

[9]   D. A. Goussis and U. Maas, "Model reduction for combustion chemistry," in *Fluid Mech. its Appl.*, vol. 95, pp. 193–220, Springer, 2011.

[10]   C. W. Gear, "Simultaneous Numerical Solution of Differential-Algebraic Equations," *IEEE Trans. Circuit Theory*, vol. 18, no. 1, 1971.

[11]   L. Brugnano, F. Mazzia, and D. Trigiante, "Fifty years of stiffness," *Recent Adv. Comput. Appl. Math.*, pp. 1–21, 2011.

[12]   B. Bhattacharjee, D. A. Schwer, P. I. Barton, and W. H. Green, "Optimally-reduced kinetic models: Reaction elimination in large-scale kinetic mechanisms," *Combust. Flame*, vol. 135, no. 3, pp. 191–208, 2003.

[13]   A. N. Gorban and I. V. Karlin, "Method of invariant manifold for chemical kinetics," *Chem. Eng. Sci.*, vol. 58, no. 21, pp. 4751–4768, 2003.

[14]   N. Peters, "Reducing mechanisms," in *Reduc. Kinet. Mech. Asymptot. Approx. Methane-Air Flames*, pp. 48–67, Springer, 1991.

[15]   T. Turányi and A. S. Tomlin, *Analysis of Kinetic Reaction Mechanisms.* Berlin, Heidelberg: Springer Berlin Heidelberg, 2014.

[16]   M. R. Roussel and S. J. Fraser, "On the geometry of transient relaxation," *J. Chem. Phys.*, vol. 94, no. 11, pp. 7106–7113, 1991.

[17]   J. Li, Z. Zhao, A. Kazakov, and F. L. Dryer, "An updated comprehensive kinetic model of hydrogen combustion," *Int. J. Chem. Kinet.*, vol. 36, no. 10, pp. 566–575, 2004.

[18]   S. B. Pope, "Small scales, many species and the manifold challenges of turbulent combustion," *Proc. Combust. Inst.*, vol. 34, no. 1, pp. 1–31, 2013.

[19]   M. Frenklach, K. Kailasanath, and E. S. Oran, "Systematic development of reduced reaction mechanisms for dynamic modeling," *Prog. Astronaut. Aeronaut.*, vol. 105, no. 2, pp. 365–376, 1986.

[20]   T. Turányi, "Sensitivity analysis of complex kinetic systems. Tools and applications," *J. Math. Chem.*, vol. 5, no. 3, pp. 203–248, 1990.

[21]   A. S. Tomlin, M. J. Pilling, T. Turanyi, J. H. Merkin, and J. Brindley, "Mechanism reduction for the oscillatory oxidation of hydrogen: Sensitivity and quasi-steady-state analyses," *Combust. Flame*, vol. 91, no. 2, pp. 107–130, 1992.

[22]   S. Vajda, P. Valko, and T. Turanyi, "Principal component analysis of kinetic models," *Int. J. Chem. Kinet.*, vol. 17, no. 1, pp. 55–81, 1985.

[23]   N. J. Brown, G. Li, and M. L. Koszykowski, "Mechanism reduction via principal component analysis," *Int. J. Chem. Kinet.*, vol. 29, no. 6, pp. 393–414, 1997.

[24]   C. E. Frouzakis and K. Boulouchos, "Analysis and Reduction of the CH4-Air Mechanism at Lean Conditions," *Combust. Sci. Technol.*, vol. 159, no. 1, pp. 281–303, 2000.

[25]   J. Warnatz, "The structure of laminar alkane-, alkene-, and acetylene flames," *Symp. Combust.*, vol. 18, no. 1, pp. 369–384, 1981.

[26]   J. Revel, J. C. Boettner, M. Cathonnet, and J. S. Bachman, "Derivation of a global chemical kinetic mechanism for methane ignition and combustion," *J. Chim. Phys.*, vol. 91, no. 4, pp. 365–382, 1994.

[27]   T. Lu and C. K. Law, "A directed relation graph method for mechanism reduction," *Proc. Combust. Inst.*, vol. 30 I, no. 1, pp. 1333–1341, 2005.

[28]   W. Sun, Z. Chen, X. Gou, and Y. Ju, "A path flux analysis method for the reduction of detailed chemical kinetic mechanisms," *Combust. Flame*, vol. 157, no. 7, pp. 1298–1307, 2010.

[29]   T. Turanyi, "Reduction of large reaction mechanisms," *New J. Chem.*, vol. 14, no. 11, pp. 795–803, 1990.

[30]   H. Karadeniz, H. S. Soyhan, and C. Sorusbay, "Reduction of large kinetic mechanisms with a new approach to the necessity analysis method," *Combust. Flame*, vol. 159, no. 4, pp. 1467–1480, 2012.

[31] L. Petzold and W. Zhu, "Model reduction for chemical kinetics: An optimization approach," *AIChE J.*, vol. 45, no. 4, pp. 869–886, 1999.

[32] I. P. Androulakis, "Kinetic mechanism reduction based on an integer programming approach," *AIChE J.*, vol. 46, no. 2, pp. 361–371, 2000.

[33] M. Valorani, F. Creta, D. A. Goussis, J. C. Lee, and H. N. Najm, "An automatic procedure for the simplification of chemical kinetic mechanisms based on CSP," *Combust. Flame*, vol. 146, no. 1-2, pp. 29–51, 2006.

[34] D. A. Goussis and G. Skevis, "Nitrogen chemistry controlling steps in methane-air premixed flames," *Comput. Fluid Solid Mech.*, vol. 1, pp. 650–653, 2005.

[35] N. Berglund and B. Gentz, "Noise-Induced Phenomena in Slow-Fast Dynamical Systems," in *Noise-Induced Phenom. Slow-Fast Dyn. Syst.*, Probability and Its Applications, pp. 17–49, London: Springer-Verlag, 2006.

[36] C. Kuehn, "A mathematical framework for critical transitions: Bifurcations, fastslow systems and stochastic dynamics," *Phys. D Nonlinear Phenom.*, vol. 240, no. 12, pp. 1020–1035, 2011.

[37] M. Bodenstein and S. C. Lind, "Geschwindigkeit der Bildung des Bromwasserstoffs aus seinen Elementen," *Zeitschrift für Phys. Chemie*, vol. 57, pp. 168–192, 1906.

[38] A. N. Al-Khateeb, J. M. Powers, S. Paolucci, A. J. Sommese, J. A. Diller, J. D. Hauenstein, and J. D. Mengers, "One-dimensional slow invariant manifolds for spatially homogenous reactive systems," *J. Chem. Phys.*, vol. 131, no. 2, p. 024118, 2009.

[39] S. H. Lam and D. A. Goussis, "The CSP method for simplifying kinetics," *Int. J. Chem. Kinet.*, vol. 26, no. 4, pp. 461–486, 1994.

[40] A. Zagaris, H. G. Kaper, and T. J. Kaper, "Fast and Slow Dynamics for the Computational Singular Perturbation Method," *Multiscale Model. Simul.*, vol. 2, no. 4, pp. 613–638, 2004.

[41] E. Chiavazzo, A. N. Gorban, and I. V. Karlin, "Comparison of Invariant Manifolds for Model Reduction in Chemical Kinetics 1 Introduction 2 Theoretical background," *Commun. Comput. Phys.*, vol. 2, no. 5, pp. 964–992, 2007.

[42] U. Maas and S. Pope, "Simplifying chemical kinetics: Intrinsic low-dimensional manifolds in composition space," *Combust. Flame*, vol. 88, no. 3-4, pp. 239–264, 1992.

[43] H. G. Kaper and T. J. Kaper, "Asymptotic analysis of two reduction methods for systems of chemical reactions," *Phys. D Nonlinear Phenom.*, vol. 165, no. 1-2, pp. 66–93, 2002.

[44] J. C. Keck and D. Gillespie, "Rate-controlled partial-equilibrium method for treating reacting gas mixtures," *Combust. Flame*, vol. 17, no. 2, pp. 237–241, 1971.

[45] J. C. Keck, "Rate-controlled constrained-equilibrium theory of chemical reactions in complex systems," *Prog. Energy Combust. Sci.*, vol. 16, no. 2, pp. 125–154, 1990.

[46] Z. Ren, S. B. Pope, A. Vladimirsky, and J. M. Guckenheimer, "The invariant constrained equilibrium edge preimage curve method for the dimension reduction of chemical kinetics," *J. Chem. Phys.*, vol. 124, no. 11, p. 114111, 2006.

[47] D. Lebiedz, "Computing minimal entropy production trajectories: An approach to model reduction in chemical kinetics," *J. Chem. Phys.*, vol. 120, no. 15, pp. 6890–6897, 2004.

[48] C. W. Gear, T. J. Kaper, I. G. Kevrekidis, and A. Zagaris, "Projecting to a Slow Manifold: Singularly Perturbed Systems and Legacy Codes," *SIAM J. Appl. Dyn. Syst.*, vol. 4, no. 3, p. 21, 2004.

[49] I. G. Kevrekidis and G. Samaey, "Equation-free multiscale computation: algorithms and applications.," *Annu. Rev. Phys. Chem.*, vol. 60, pp. 321–344, 2009.

[50] D. Hilbert, "Mathematical problems," *Bull. Am. Math. Soc.*, vol. 8, no. 10, pp. 437–480, 1902.

[51] L. Saint-Raymond, *Hydrodynamic Limits of the Boltzmann Equation*, vol. 1971 of *Lecture Notes in Mathematics*. Berlin, Heidelberg: Springer Berlin Heidelberg, 2009.

[52] M. Slemrod, "From Boltzmann to Euler: Hilbert's 6th problem revisited," *Comput. Math. with Appl.*, vol. 65, no. 10, pp. 1497–1501, 2013.

[53] A. N. Gorban and I. V. Karlin, "Hilbert's 6th problem: Exact and approximate hydrodynamic manifolds for kinetic equations," *Bull. Am. Math. Soc.*, vol. 51, no. 2, pp. 187–246, 2014.

[54] S. Chapman and T. G. Cowling, *The mathematical theory of non-uniform gases: an account of the kinetic theory of viscosity, thermal conduction and diffusion in gases.* 1970.

[55] H. Grad, "On the kinetic theory of rarefied gases," *Commun. Pure Appl. Math.*, vol. 2, no. 4, pp. 331–407, 1949.

[56] I. V. Karlin and A. N. Gorban, "Hydrodynamics from Grad's equations: What can we learn from exact solutions?," *Ann. Phys.*, vol. 11, no. 10-11, pp. 783–833, 2002.

[57] A. N. Gorban, I. V. Karlin, and A. Y. Zinovyev, "Invariant grids for reaction kinetics," *Phys. A Stat. Mech. its Appl.*, vol. 333, no. 1-4, pp. 106–154, 2004.

[58] E. Chiavazzo and I. V. Karlin, "Adaptive simplification of complex multiscale systems," *Phys. Rev. E - Stat. Nonlinear, Soft Matter Phys.*, vol. 83, no. 3, p. 036706, 2011.

[59] A. N. Gorban and I. V. Karlin, *Invariant manifolds for physical and chemical kinetics.* Springer, 2009.

[60] A. Debussche and R. Temam, "Inertial Manifolds and Slow Manifolds," *Appl. Math. Lett.*, vol. 4, no. 4, pp. 73–76, 1991.

[61] J. C. Robinson, "A concise proof of the "geometric" construction of inertial manifolds," *Phys. Lett. A*, vol. 200, no. 6, pp. 415–417, 1995.

[62] A. N. Gorban and I. V. Karlin, "Thermodynamic parameterization," *Phys. A Stat. Mech. its Appl.*, vol. 190, no. 3-4, pp. 393–404, 1992.

[63] A. C. Tsoumanis, K. Rajendran, C. I. Siettos, and I. G. Kevrekidis, "Coarse-graining the dynamics of network evolution: The rise and fall of a networked society," *AIP Conf. Proc.*, vol. 1389, no. 8, pp. 42–45, 2011.

[64] V. Bykov, I. Goldfarb, V. Gol'dshtein, and U. Maas, "On a modified version of ILDM approach: Asymptotic analysis based on integral manifolds," *IMA J. Appl. Math.*, vol. 71, no. 3, pp. 359–382, 2006.

[65] S. B. Pope, "Gibbs function continuation for the stable computation of chemical equilibrium," *Combust. Flame*, vol. 139, no. 3, pp. 222–226, 2004.

[66] V. Bykov and U. Maas, "Extension of the ILDM method to the domain of slow chemistry," *Proc. Combust. Inst.*, vol. 31 I, no. 1, pp. 465–472, 2007.

[67] Q. Tang and S. B. Pope, "A more accurate projection in the rate-controlled constrained-equilibrium method for dimension reduction of combustion chemistry," *Combust. Theory Model.*, vol. 8, no. 2, pp. 255–279, 2004.

[68] W. P. Jones and S. Rigopoulos, "Rate-controlled constrained equilibrium: Formulation and application to nonpremixed laminar flames," *Combust. Flame*, vol. 142, no. 3, pp. 223–234, 2005.

[69] S. Rigopoulos and T. Lø vås, "A LOI-RCCE methodology for reducing chemical kinetics, with application to laminar premixed flames," *Proc. Combust. Inst.*, vol. 32 I, no. 1, pp. 569–576, 2009.

[70] R. Law, M. Metghalchi, and J. C. Keck, "Rate-controlled constrained equilibrium calculation of ignition delay times in hydrogen-oxygen mixtures," *Symp. Combust.*, vol. 22, no. 1, pp. 1705–1713, 1989.

[71] G. Beretta, J. C. Keck, M. Janbozorgi, and H. Metghalchi, "The rate-controlled constrained-equilibrium approach to far from local equilibrium thermodynamics," *Entropy*, vol. 14, no. 2, pp. 92–130, 2012.

[72] P. S. Bishnu, D. Hamiroune, M. Metghalchi, and J. C. Keck, "Constrained-equilibrium calculations for chemical systems subject to generalized linear constraints using the NASA and STANJAN equilibrium programs," *Combust. Theory Model.*, vol. 1, no. 3, pp. 295–312, 1997.

[73] D. Hamiroune, P. Bishnu, M. Metghalchi, and J. C. Keck, "Rate-controlled constrained-equilibrium method using constraint potentials," *Combust. Theory Model.*, vol. 2, no. 1, pp. 81–94, 1998.

[74] M. Janbozorgi, S. Ugarte, H. Metghalchi, and J. C. Keck, "Combustion modeling of mono-carbon fuels using the rate-controlled constrained-equilibrium method," *Combust. Flame*, vol. 156, no. 10, pp. 1871–1885, 2009.

[75] V. Hiremath, S. R. Lantz, H. Wang, and S. B. Pope, "Large-scale parallel simulations of turbulent combustion using combined dimension reduction and tabulation of chemistry," *Proc. Combust. Inst.*, vol. 34, no. 1, pp. 205–215, 2013.

[76] O. Gicquel, D. Thévenin, M. Hilka, and N. Darabiha, "Direct numerical simulation of turbulent premixed flames using intrinsic low-dimensional manifolds," *Combust. Theory Model.*, vol. 3, no. 3, pp. 479–502, 1999.

[77] S. H. Lam and D. A. Coussis, "Understanding complex chemical kinetics with computational singular perturbation," *Symp. Combust.*, vol. 22, no. 1, pp. 931–941, 1989.

[78] A. N. Gorban and I. V. Karlin, "Uniqueness of thermodynamic projector and kinetic basis of molecular individualism," *Phys. A Stat. Mech. its Appl.*, vol. 336, no. 3-4, pp. 391–432, 2004.

[79] E. Chiavazzo, I. V. Karlin, and A. N. Gorban, "The role of thermodynamics in model reduction when using invariant grids," *Commun. Comput. Phys.*, vol. 8, no. 4, pp. 701–734, 2010.

[80] D. Schmidt, J. Segatz, U. Riedel, J. Warnatz, and U. Maas, "Simulation of Laminar Methane-Air Flames using Automatically Simplified Chemical Kinetics," *Combust. Sci. Technol.*, vol. 113, no. 1, pp. 3–16, 1996.

[81] S. B. Pope, "The computation of constrained and unconstrained equilibrium compositions of ideal gas mixtures using Gibbs function continuation," tech. rep., Cornell University, 2003.

[82] S. B. Pope, "CEQ: A FORTRAN library to compute equilibrium compositions using Gibbs function continuation," 2003.

[83] W. I. Thacker, J. Zhang, L. Watson, J. B. Birch, M. A. Iyer, and M. W. Berry, "Algorithm 905," *ACM Trans. Math. Softw.*, vol. 37, no. 3, pp. 1–20, 2010.

[84] P. N. Brown, G. D. Byrne, and A. C. Hindmarsh, "VODE: A Variable-Coefficient ODE Solver," *SIAM J. Sci. Stat. Comput.*, vol. 10, no. 5, pp. 1038–1051, 1989.

[85] M. R. Roussel and S. J. Fraser, "Global analysis of enzyme inhibition kinetics," *J. Phys. Chem.*, vol. 97, no. 31, pp. 8316–8327, 1993.

[86] W. P. Jones and S. Rigopoulos, "Reduced chemistry for hydrogen and methanol premixed flames via RCCE," *Combust. Theory Model.*, vol. 11, no. 5, pp. 755–780, 2007.

[87] R. J. Kee, J. F. Grcar, M. D. Smooke, and J. A. Miller, "PREMIX: a Fortran program for modeling steady laminar one-dimensional premixed flames," tech. rep., 1985.

[88] R. L. G. M. Eggels and L. P. H. de Goey, "Mathematically reduced reaction mechanisms applied to adiabatic flat hydrogen/air flames," *Combust. Flame*, vol. 100, no. 4, pp. 559–570, 1995.

[89] C. D. Levermore, "Moment closure hierarchies for kinetic theories," *J. Stat. Phys.*, vol. 83, pp. 1021–1065, June 1996.

[90] A. N. Gorban and I. V. Karlin, "Quasi-equilibrium closure hierarchies for the Boltzmann equation," *Phys. A Stat. Mech. its Appl.*, vol. 360, no. 2, pp. 325–364, 2006.

[91] I. V. Karlin, S. S. Chikatamarla, and M. Kooshkbaghi, "Non-perturbative hydrodynamic limits: A case study," *Phys. A Stat. Mech. its Appl.*, vol. 403, pp. 189–194, 2014.

[92] M. Kooshkbaghi, C. E. Frouzakis, E. Chiavazzo, K. Boulouchos, and I. V. Karlin, "The global relaxation redistribution method for reduction of combustion kinetics," *J. Chem. Phys.*, vol. 141, no. 4, p. 044102, 2014.

[93] E. Chiavazzo, I. V. Karlin, C. E. Frouzakis, and K. Boulouchos, "Method of invariant grid for model reduction of hydrogen combustion," *Proc. Combust. Inst.*, vol. 32, no. 1, pp. 519–526, 2009.

[94] A. N. Kolmogorov, "New Metric Invariant of Transitive Dynamical Systems and Endomorphisms of Lebesgue Spaces," *Dokl. Russ. Acad. Sci.*, vol. 119, no. N5, pp. 861–864, 1958.

[95] Y. G. Sinai, "On the Notion of Entropy of a Dynamical System," *Dokl. Russ. Acad. Sci.*, vol. 124, pp. 768–771, 1959.

[96] P. Ball, "Chaos-theory pioneer nabs Abel Prize," *Nature*, 2014.

[97] J. Keener and S. James, *Mathematical Physiology*, vol. 8 of *Interdisciplinary Applied Mathematics*. New York: Springer-Verlag, 1998.

[98] A. H. Nguyen and S. J. Fraser, "Geometrical picture of reaction in enzyme kinetics," *J. Chem. Phys.*, vol. 91, no. 1, p. 186, 1989.

[99] M. R. Roussel and T. Tang, "The functional equation truncation method for approximating slow invariant manifolds: a rapid method for computing intrinsic low-dimensional manifolds.," *J. Chem. Phys.*, vol. 125, no. 21, p. 214103, 2006.

[100] A. N. Gorban and M. Shahzad, "The Michaelis-Menten-Stueckelberg Theorem," *Entropy*, vol. 13, no. 12, pp. 966–1019, 2011.

[101] J. Eckmann and D. Ruelle, "Ergodic theory of chaos and strange attractors," *Rev. Mod. Phys.*, vol. 57, no. 3, pp. 617–656, 1985.

[102] A. Wolf, J. Swift, H. Swinney, and J. Vastano, "Determining Lyapunov exponents from a time series," *Phys. D Nonlinear Phenom.*, vol. 16, no. 3, pp. 285–317, 1985.

[103] K. D. Mease, S. Bharadwaj, and S. Iravanchy, "Timescale analysis for nonlinear dynamical systems," *J. Guid. Control. Dyn.*, vol. 26, no. 2, pp. 318–330, 2003.

[104] R. J. Kee, G. Dixon-Lewis, J. Warnatz, M. E. Coltrin, and J. A. Miller, "Chemkin-III: a Fortran chemical kinetics package for the analysis of gas-phase chemical and plasma kinetics," tech. rep., Sandia National Laboratories, 1996.

[105] P. S. Gregory, D. M. Golden, M. Frenklach, N. W. Moriarty, B. Eiteneer, M. Goldenberg, C. T. Bowman, R. K. Hanson, S. Song, W. C. Gardiner, V. V. Lissianski, and Z. Qin, "GRI-Mech 1.2," 1994.

[106] L. Tosatto, B. A. V. Bennett, and M. D. Smooke, "Comparison of different DRG-based methods for the skeletal reduction of JP-8 surrogate mechanisms," *Combust. Flame*, vol. 160, no. 9, pp. 1572–1582, 2013.

[107] M. Kooshkbaghi, C. E. Frouzakis, K. Boulouchos, and I. V. Karlin, "Entropy production analysis for mechanism reduction," *Combust. Flame*, vol. 161, no. 6, pp. 1507–1515, 2014.

[108] D. A. Schwer, P. Lu, and W. H. Green, "An adaptive chemistry approach to modeling complex kinetics in reacting flows," *Combust. Flame*, vol. 133, no. 4, pp. 451–465, 2003.

[109] K. He, M. G. Ierapetritou, and I. P. Androulakis, "A graph-based approach to developing adaptive representations of complex reaction mechanisms," *Combust. Flame*, vol. 155, no. 4, pp. 585–604, 2008.

[110] A. Massias, D. Diamantis, E. Mastorakos, and D. A. Goussis, "An algorithm for the construction of global reduced mechanisms with CSP data," *Combust. Flame*, vol. 117, no. 4, pp. 685–708, 1999.

[111] I. Banerjee and M. Ieapetritou, "An adaptive reduction scheme to model reactive flow," *Combust. Flame*, vol. 144, no. 3, pp. 619–633, 2006.

[112] T. Lu, Y. Ju, and C. K. Law, "Complex CSP for chemistry reduction and analysis," *Combust. Flame*, vol. 126, no. 1-2, pp. 1445–1455, 2001.

[113] T. Lu and C. K. Law, "A criterion based on computational singular perturbation for the identification of quasi steady state species: A reduced mechanism for methane oxidation with NO chemistry," *Combust. Flame*, vol. 154, no. 4, pp. 761–774, 2008.

[114] M. Valorani, F. Creta, F. Donato, H. N. Najm, and D. A. Goussis, "Skeletal mechanism generation and analysis for n-heptane with CSP," *Proc. Combust. Inst.*, vol. 31, no. 1, pp. 483–490, 2007.

[115] T. Lu and C. K. Law, "On the applicability of directed relation graphs to the reduction of reaction mechanisms," *Combust. Flame*, vol. 146, no. 3, pp. 472–483, 2006.

[116] T. Lu and C. K. Law, "Linear time reduction of large kinetic mechanisms with directed relation graph: n-heptane and iso-octane," *Combust. Flame*, vol. 144, no. 1-2, pp. 24–36, 2006.

[117] T. Lu and C. Law, "Strategies for mechanism reduction for large hydrocarbons: n-heptane," *Combust. Flame*, vol. 154, no. 1-2, pp. 153–163, 2008.

[118] Z. Luo, T. Lu, and J. Liu, "A reduced mechanism for ethylene/methane mixtures with excessive NO enrichment," *Combust. Flame*, vol. 158, no. 7, pp. 1245–1254, 2011.

[119] P. Pepiotdesjardins and H. Pitsch, "An efficient error-propagation-based reduction method for large chemical kinetic mechanisms," *Combust. Flame*, vol. 154, no. 1-2, pp. 67–81, 2008.

[120] K. E. Niemeyer and C.-J. Sung, "On the importance of graph search algorithms for DRGEP-based mechanism reduction methods," *Combust. Flame*, vol. 158, no. 8, pp. 1439–1443, 2011.

[121] X. Zheng, T. Lu, and C. Law, "Experimental counterflow ignition temperatures and reaction mechanisms of 1,3-butadiene," *Proc. Combust. Inst.*, vol. 31, no. 1, pp. 367–375, 2007.

[122] K. E. Niemeyer, C.-J. Sung, and M. P. Raju, "Skeletal mechanism generation for surrogate fuels using directed relation graph with error propagation and sensitivity analysis," *Combust. Flame*, vol. 157, no. 9, pp. 1760–1770, 2010.

[123] L. Tosatto, B. Bennett, and M. Smooke, "A transport-flux-based directed relation graph method for the spatially inhomogeneous instantaneous reduction of chemical kinetic mechanisms," *Combust. Flame*, vol. 158, pp. 820–835, May 2011.

[124] G. Li and H. Rabitz, "A general analysis of approximate lumping in chemical kinetics," *Chem. Eng. Sci.*, vol. 45, no. 4, pp. 977–1002, 1990.

[125] H. Huang, M. Fairweather, J. F. Griffiths, A. S. Tomlin, and R. B. Brad, "A systematic lumping approach for the reduction of comprehensive kinetic models," *Proc. Combust. Inst.*, vol. 30, no. 1, pp. 1309–1316, 2005.

[126] T. Lu and C. K. Law, "Diffusion coefficient reduction through species bundling," *Combust. Flame*, vol. 148, no. 3, pp. 117–126, 2007.

[127] L. Liang, J. G. Stevens, and J. T. Farrell, "A dynamic adaptive chemistry scheme for reactive flow computations," *Proc. Combust. Inst.*, vol. 32, no. 1, pp. 527–534, 2009.

[128] L. Liang, J. G. Stevens, S. Raman, and J. T. Farrell, "The use of dynamic adaptive chemistry in combustion simulation of gasoline surrogate fuels," *Combust. Flame*, vol. 156, no. 7, pp. 1493–1502, 2009.

[129] F. Contino, H. Jeanmart, T. Lucchini, and G. D'Errico, "Coupling of in situ adaptive tabulation and dynamic adaptive chemistry: An

effective method for solving combustion in engine simulations," *Proc. Combust. Inst.*, vol. 33, no. 2, pp. 3057–3064, 2011.

[130] I. Prigogine and P. V. Rysselberghe, *Introduction to Thermodynamics of Irreversible Processes*, vol. 110. 1963.

[131] T. Donder and P. V. Rysselberghe, *Thermodynamic theory of affinity, Band 1*. 1936.

[132] D. Kondepudi and I. Prigogine, *Modern Thermodynamics: From Heat Engines to Dissipative Structures*. Wiley, 1 ed., 1998.

[133] "MECHMOD: Manipulation of CHEMKIN format mechanisms." http://garfield.chem.elte.hu/Combustion/mechmod.htm/, 2003.

[134] A. N. Gorban, E. M. Mirkes, and G. S. Yablonsky, "Thermodynamics in the limit of irreversible reactions," *Phys. A Stat. Mech. its Appl.*, vol. 392, no. 6, pp. 1318–1335, 2013.

[135] N. Peters, G. Paczko, R. Seiser, and K. Seshadri, "Temperature crossover and non-thermal runaway at two-stage ignition of n-heptane," *Combust. Flame*, vol. 128, no. 1-2, pp. 38–59, 2002.

[136] "n-heptane, Detailed Mechanism, Version 2." https://www-pls.llnl.gov/?url=science_and_technology-chemistry-combustion-nc7h16, 1998.

[137] J. Prager, H. N. Najm, M. Valorani, and D. A. Goussis, "Skeletal mechanism generation with CSP and validation for premixed n-heptane flames," *Proc. Combust. Inst.*, vol. 32, no. 1, pp. 509–517, 2009.

[138] J. B. Heywood, *Internal Combustion Engine Fundamentals*, vol. 21. 1988.

[139] K. Nishida, T. Takagi, and S. Kinoshita, "Analysis of entropy generation and exergy loss during combustion," *Proc. Combust. Inst.*, vol. 29, no. 1, pp. 869–874, 2002.

[140] O. Herbinet and G. Dayma, "Jet-Stirred Reactors," *Clean. Combust.*, 2013.

[141] O. Bilous and N. R. Amundson, "Chemical reactor stability and sensitivity," *AIChE J.*, vol. 1, no. 4, pp. 513–521, 1955.

[142] R. Aris and N. R. Amundson, "An analysis of chemical reactor stability and control-I," *Chem. Eng. Sci.*, vol. 7, no. 3, pp. 121–131, 1958.

[143] A. Uppal, W. Ray, and A. Poore, "On the dynamic behavior of continuous stirred tank reactors," *Chem. Eng. Sci.*, vol. 29, no. 4, pp. 967–985, 1974.

[144] W. W. Farr and R. Aris, ""Yet who would have thought the old man to have had so much blood in him?"—Reflections on the multiplicity of steady states of the stirred tank reactor," *Chem. Eng. Sci.*, vol. 41, no. 6, pp. 1385–1402, 1986.

[145] P. Gray and S. K. Scott, *Chemical Oscillations and Instabilities.* Springer, 1996.

[146] C. K. Law, *Combustion Physics.* Cambridge University Press, 2006.

[147] A. B. Poore, "A model equation arising from chemical reactor theory," *Arch. Ration. Mech. Anal.*, vol. 52, no. 4, pp. 358–388, 1973.

[148] V. Balakotaiah and D. Luss, "Structure of the steady-state solutions of lumped-parameter chemically reacting systems," *Chem. Eng. Sci.*, vol. 37, no. 11, pp. 1611–1623, 1982.

[149] H. S. Sidhu, M. I. Nelson, G. N. Mercer, and R. O. Weber, "Dynamical analysis of an elementary X + Y = P reaction in a continuously stirred tank reactor," *J. Math. Chem.*, vol. 28, pp. 353–375, Dec. 2000.

[150] R. Warden, R. Aris, and N. Amundson, "An analysis of chemical reactor stability and control—VIII," *Chem. Eng. Sci.*, vol. 19, no. 3, pp. 149–172, 1964.

[151] F. Strozzi and J. Zaldívar, "A general method for assessing the thermal stability of batch chemical reactors by sensitivity calculation based on Lyapunov exponents," *Chem. Eng. Sci.*, vol. 49, no. 16, pp. 2681–2688, 1994.

[152] J. Alvarez, J. Alvarez, and E. González, "Global nonlinear control of a continuous stirred tank reactor," *Chem. Eng. Sci.*, vol. 44, no. 5, pp. 1147–1160, 1989.

[153] J. F. Griffiths and S. K. Scott, "Thermokinetic interactions: Fundamentals of spontaneous ignition and cool flames," *Prog. Energy Combust. Sci.*, vol. 13, no. 3, pp. 161–197, 1987.

[154] S. Kalamatianos and D. G. Vlachos, "Bifurcation Behavior of Premixed Hydrogen/Air Mixtures in a Continuous Stirred Tank Reactor," *Combust. Sci. Technol.*, vol. 109, no. 1-6, pp. 347–371, 1995.

[155] S. Kalamatianos, Y. K. Park, and D. G. Vlachos, "Two-parameter continuation algorithms for sensitivity analysis, parametric dependence, reduced mechanisms, and stability criteria of ignition and extinction," *Combust. Flame*, vol. 112, no. 1-2, pp. 45–61, 1998.

[156] R. J. Olsen and D. G. Vlachos, "A Complete Pressure Temperature Diagram for Air Oxidation of Hydrogen in a Continuous Flow Stirred Tank Reactor," *J. Phys. Chem. A*, vol. 103, no. 40, pp. 7990–7999, 1999.

[157] R. Shan and T. Lu, "Ignition and extinction in perfectly stirred reactors with detailed chemistry," *Combust. Flame*, vol. 159, no. 6, pp. 2069–2076, 2012.

[158] R. Shan and T. Lu, "A bifurcation analysis for limit flame phenomena of DME/air in perfectly stirred reactors," *Combust. Flame*, vol. 161, no. 7, pp. 1716–1723, 2014.

[159] R. Shan, C. S. Yoo, J. H. Chen, and T. Lu, "Computational diagnostics for n-heptane flames with chemical explosive mode analysis," *Combust. Flame*, vol. 159, no. 10, pp. 3119–3127, 2012.

[160] T. Lu and C. K. Law, "Toward accommodating realistic fuel chemistry in large-scale computations," *Prog. Energy Combust. Sci.*, vol. 35, no. 2, pp. 192–215, 2009.

[161] H. B. Keller, *Lectures on numerical methods in bifurcation problems.* Springer, 1987.

[162] E. J. Doedel, "AUTO: A program for the automatic bifurcation analysis of autonomous systems," *Congr. Numer*, 1981.

[163] E. J. Doedel and B. E. Oldeman, *AUTO-07P : Continuation and Bifurcation Software for Ordinary Differential Equations.* Concordia University, Montreal, Canada, 2009.

[164] A. Kazakov, M. Chaos, Z. Zhao, and F. L. Dryer, "Computational singular perturbation analysis of two-stage ignition of large hydrocarbons.," *J. Phys. Chem. A*, vol. 110, no. 21, pp. 7003–9, 2006.

[165] D. J. Diamantis, D. C. Kyritsis, and D. A. Goussis, "Two Stage Ignition of n-heptane: Identifying the Chemistry Setting the Explosive Time Scales," in *Second Int. Work. Model Reduct. React. Flows*, 2009.

[166] S. Gupta, H. G. Im, and M. Valorani, "Analysis of n-heptane auto-ignition characteristics using computational singular perturbation," *Proc. Combust. Inst.*, vol. 34, no. 1, pp. 1125–1133, 2013.

[167] W. Liu, C. K. Law, and T. Lu, "Multiple criticality and staged ignition of methane in the counterflow," *Int. J. Chem. Kinet.*, vol. 41, pp. 764–776, Dec. 2009.

[168] H. Meijer, F. Dercole, and B. Oldeman, "Numerical bifurcation analysis," *Encycl. Complex. Syst. Sci.*, pp. 6329–6352, 2009.

[169] I. Kuznetsov, *Elements of applied bifurcation theory*. Springer, 1998.

[170] R. J. Olsen and I. R. Epstein, "Bifurcation analysis of chemical reaction mechanisms. I. Steady state bifurcation structure," *J. Chem. Phys.*, vol. 94, no. 4, p. 3083, 1991.

[171] D. J. Diamantis, E. Mastorakos, and D. A. Goussis, "H2/air autoignition: The nature and interaction of the developing explosive modes," *Combust. Theory Model.*, pp. 1–52, 2015.

[172] M. Valorani, H. N. Najm, and D. A. Goussis, "CSP analysis of a transient flame-vortex interaction," *Combust. Flame*, vol. 134, no. 1-2, pp. 35–53, 2003.

[173] T. Lu, C. S. Yoo, J. H. Chen, and C. K. Law, "Three-dimensional direct numerical simulation of a turbulent lifted hydrogen jet flame in heated coflow: a chemical explosive mode analysis," *J. Fluid Mech.*, vol. 652, pp. 45–64, 2010.

[174] Z. Luo, C. S. Yoo, E. S. Richardson, J. H. Chen, C. K. Law, and T. Lu, "Chemical explosive mode analysis for a turbulent lifted ethylene jet flame in highly-heated coflow," *Combust. Flame*, vol. 159, no. 1, pp. 265–274, 2012.

[175] D. A. Goussis and H. N. Najm, "Model Reduction and Physical Understanding of Slowly Oscillating Processes: The Circadian Cycle," *Multiscale Model. Simul.*, vol. 5, no. 4, pp. 1297–1332, 2006.

[176] L. Hascoet and V. Pascual, "The Tapenade Automatic Differentiation tool: principles, model, and specification," *ACM Trans. Math. Softw.*, vol. 20, 2013.

[177] E. Anderson, Z. Bai, C. Bischof, S. Blackford, J. Demmel, J. Dongarra, J. Du Croz, A. Greenbaum, S. Hammarling, A. McKenney, and D. Sorensen, *LAPACK Users' Guide*. Philadelphia, PA: Society for Industrial and Applied Mathematics, third ed., 1999.

[178] R. Tolman and P. Fine, "On the Irreversible Production of Entropy," *Rev. Mod. Phys.*, vol. 20, no. 1, pp. 51–77, 1948.

[179] W. R. Dunbar and N. Lior, "Sources of combustion irreversibility," *Combust. Sci. Technol.*, 1994.

[180] I. Glassman and R. A. Yetter, *Combustion*. 2008.

[181] C. K. Westbrook, "Chemical kinetics of hydrocarbon ignition in practical combustion systems," *Proc. Combust. Inst.*, vol. 28, no. 2, pp. 1563–1577, 2000.

[182] P. D. Kourdis and D. A. Goussis, "Glycolysis in Saccharomyces cerevisiae: algorithmic exploration of robustness and origin of oscillations.," *Math. Biosci.*, vol. 243, no. 2, pp. 190–214, 2013.

[183] A. V. Bobylev, "The Chapman-Enskog and Grad methods for solving the Boltzmann equation," *Akad. Nauk SSSR Dokl.*, 1982.

[184] M. Slemrod, "Chapman-Enskog– viscosity-capillarity," *Q. Appl. Math.*, vol. 70, no. 3, pp. 613–624, 2012.

[185] F. J. Dyson, "The S Matrix in Quantum Electrodynamics," *Phys. Rev.*, vol. 75, no. 11, pp. 1736–1755, 1949.

[186] J. Schwinger, "On the Green's functions of quantized fields. I," *Proc. Natl. Acad. Sci.*, vol. 37, no. 7, pp. 452–455, 1951.

[187] S. Succi, H. Chen, and S. Orszag, "Relaxation approximations and kinetic models of fluid turbulence," *Phys. A Stat. Mech. its Appl.*, vol. 362, no. 1, pp. 1–5, 2006.

[188] J. Lätt, B. Chopard, S. Succi, and F. Toschi, "Numerical analysis of the averaged flow field in a turbulent lattice Boltzmann simulation," *Phys. A Stat. Mech. its Appl.*, vol. 362, no. 1, pp. 6–10, 2006.

[189] A. Singer, R. Erban, I. G. Kevrekidis, and R. R. Coifman, "Detecting intrinsic slow variables in stochastic dynamical systems by anisotropic diffusion maps.," *Proc. Natl. Acad. Sci. U. S. A.*, vol. 106, pp. 16090–5, Sept. 2009.

[190] C. J. Dsilva, R. Talmon, N. Rabin, R. R. Coifman, and I. G. Kevrekidis, "Nonlinear intrinsic variables and state reconstruction in multiscale simulations.," *J. Chem. Phys.*, vol. 139, p. 184109, Nov. 2013.

[191] Fischer, P. F. and Lottes, J. W. and Kerkemier, S. G., "NEK5000." http://nek5000.mcs.anl.gov., 2008.

[192] C. Altantzis, C. E. Frouzakis, A. G. Tomboulides, M. Matalon, and K. Boulouchos, "Hydrodynamic and thermodiffusive instability effects on the evolution of laminar planar lean premixed hydrogen flames," *J. Fluid Mech.*, vol. 700, pp. 329–361, May 2012.

[193] C. Altantzis, C. E. Frouzakis, A. G. Tomboulides, and K. Boulouchos, "Numerical simulation of propagating circular and cylindrical lean premixed hydrogen/air flames," *Proc. Combust. Inst.*, vol. 34, pp. 1109–1115, Jan. 2013.

LAV

Laboratorium für Aerothermochemie und Verbrennungssysteme
Aerothermochemistry and Combustion Systems Laboratory

Address: ETH Zürich,
Institut f. Energietechnik
ML L 18, Sonneggstrasse 3
8092 Zürich
Phone: +41 (44) 632 26 50
Website: www.lav.ethz.ch/people/mahdik
E-mail: kooshkbaghi@lav.mavt.ethz.ch
E-mail: mahdi.kooshkbaghi@gmail.com

Gender: Male
Nationality: Iranian
Marital status: Single
Birth-date: 25-01-1986
Place of Birth: Tehran

Curriculum Vitæ
Mahdi Kooshkbaghi

Education

2012 – 2015	• Ph.D in Mechanical Engineering at LAV, ETH Zürich
2008 – 2011	• M.Sc. in Mechanical Engineering at Tehran Polytechnic
2008 – 2010	• B.Sc. in Aerospace Engineering at Tehran Polytechnic
2004 – 2008	• B.Sc. in Mechanical Engineering at Tehran Polytechnic

Journal Publications

2015
• Kooshkbaghi, Mahdi, Christos E. Frouzakis, Konstantinos Boulouchos, and Iliya V. Karlin. "n-Heptane/air combustion in perfectly stirred reactors: Dynamics, bifurcations and dominant reactions at critical conditions." Combustion and Flame (2015), 162, no. 9 (2015): 3166-3179.

2014
• Kooshkbaghi, Mahdi, Christos E. Frouzakis, Konstantinos Boulouchos, and Iliya V. Karlin. "The global relaxation redistribution method for reduction of combustion kinetics." Journal of Chemical Physics, 141, 044102.

• Kooshkbaghi, Mahdi, Christos E. Frouzakis, Konstantinos Boulouchos, and Ilya V. Karlin. "Entropy production analysis for mechanism reduction." Combustion and Flame, 161, no. 6: 1507-1515.

• Karlin, I. V., S. S. Chikatamarla, and M. Kooshkbaghi. "Non-perturbative hydrodynamic limits: A case study." Physica A: Statistical Mechanics and its Applications 403: 189-194.

2013
• Kooshkbaghi, Mahdi, and Bamdad Lessani. "A collocated grid, projection method for timeaccurate calculation of lowMach number variable density flows in general curvilinear coordinates." International Journal for Numerical Methods in Fluids 72, no. 3: 301-319.

2010
• Shokouhmand, H., M. Fakoor Pakdaman, and M. Kooshkbaghi. "A similarity solution in order to solve the governing equations of laminar separated fluids with a flat plate." Communications in Nonlinear Science and Numerical Simulation 15, no. 12: 3965-3973.

Conference Proceedings

2014
- Kooshkbaghi, Mahdi, Christos E. Frouzakis, Eliodoro Chiavazzo, Ilya V. Karlin, and Konstantinos Boulouchos. "New Approaches For The Construction Of Reduced And Skeletal Mechanisms". IEA's 36th Task Leaders Meeting, Stavanger, Norway.

2013
- Kooshkbaghi, Mahdi, Christos E. Frouzakis, Eliodoro Chiavazzo, Ilya V. Karlin, and Konstantinos Boulouchos. "Relaxation Redistribution Method for model reduction". 4th IWMRRF, San Francisco, California, USA.

2009
- Rahimian, M.H, Fakoor Pakdaman, M. and Kooshkbaghi, M., "An Analytical and Numerical Similarity Solution for Laminar Flow and Heat Transfer Between Two Separated Fluids"., ISPT20, Vancouver, Canada.